February 2002 • NREL/SR-520-31528

Subcontractor Report

Impurity Precipitation, Dissolution, Gettering, and Passivation in PV Silicon

Final Technical Report
30 January 1998—29 August 2001

E.R. Weber
University of California at Berkeley
Berkeley, California

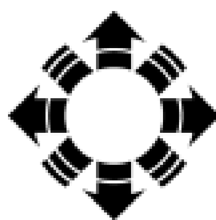

NREL

National Renewable Energy Laboratory

1617 Cole Boulevard
Golden, Colorado 80401-3393

NREL is a U.S. Department of Energy Laboratory
Operated by Midwest Research Institute • Battelle • Bechtel

Contract No. DE-AC36-99-GO10337

February 2002 • NREL/SR-520-31528

Impurity Precipitation, Dissolution, Gettering, and Passivation in PV Silicon

Final Technical Report
30 January 1998—29 August 2001

E.R. Weber
University of California at Berkeley
Berkeley, California

NREL Technical Monitor: B. McConnell

Prepared under Subcontract No. XAF-8-17607-04

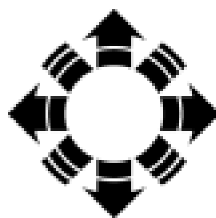

National Renewable Energy Laboratory

1617 Cole Boulevard
Golden, Colorado 80401-3393

NREL is a U.S. Department of Energy Laboratory
Operated by Midwest Research Institute • Battelle • Bechtel

Contract No. DE-AC36-99-GO10337

This publication was reproduced from the best available copy
Submitted by the subcontractor and received no editorial review at NREL

NOTICE

This report was prepared as an account of work sponsored by an agency of the United States government. Neither the United States government nor any agency thereof, nor any of their employees, makes any warranty, express or implied, or assumes any legal liability or responsibility for the accuracy, completeness, or usefulness of any information, apparatus, product, or process disclosed, or represents that its use would not infringe privately owned rights. Reference herein to any specific commercial product, process, or service by trade name, trademark, manufacturer, or otherwise does not necessarily constitute or imply its endorsement, recommendation, or favoring by the United States government or any agency thereof. The views and opinions of authors expressed herein do not necessarily state or reflect those of the United States government or any agency thereof.

Available electronically at http://www.osti.gov/bridge

Available for a processing fee to U.S. Department of Energy and its contractors, in paper, from:

U.S. Department of Energy
Office of Scientific and Technical Information
P.O. Box 62
Oak Ridge, TN 37831-0062
phone: 865.576.8401
fax: 865.576.5728
email: reports@adonis.osti.gov

Available for sale to the public, in paper, from:
U.S. Department of Commerce
National Technical Information Service
5285 Port Royal Road
Springfield, VA 22161
phone: 800.553.6847
fax: 703.605.6900
email: orders@ntis.fedworld.gov
online ordering: http://www.ntis.gov/ordering.htm

Printed on paper containing at least 50% wastepaper, including 20% postconsumer waste

Table of contents

1 Executive summary 2
2 Introduction 7
PART 1. Fundamentals of copper and iron in silicon....10
3 Diffusion, defect reactions, and recombination properties of copper in silicon 9
3.1 Determination of intrinsic and effective diffusion coefficients of copper in silicon 9
3.2 Point defect reactions of copper in silicon 16
3.3 Precipitation behavior of copper in silicon 17
3.4 Electrostatic model of precipitation behavior of copper in silicon 21
3.5 Study of the recombination activity of copper in n-type and p-type silicon: copper as a lifetime killing impurity at high copper concentrations. 25
3.6 Impact of copper on minority carrier diffusion length in n-Si at low copper concentrations. 29
3.7 Studies of kinetics of precipitation of interstitial copper at oxygen precipitates 33
3.8 Study of the thermal stability of copper precipitates in silicon 37
4 Iron in silicon 40
4.1 Analysis of the current understanding of iron in silicon 40
4.2 Method of evaluation of precipitation sites density from the analysis of iron precipitation kinetics 45
4.3 Studies of the processes of precipitation of iron, dissolution of iron precipitates, and effect of iron precipitation on minority carrier diffusion length 50
PART 2. Transition metals in PV-silicon 53
5 Application of synchrotron radiation-based X-ray fluorescence microprobe to detect impurities at the location of a shunt. 52
6 Study of chemical state and stability of iron precipitates in silicon 54
7 Application of X-ray fluorescence microprobe technique to the analysis of fully processed solar cells 57
8 Development of an experimental procedure to locate defects in-situ in a beam line 62
9 An attempt to apply the experimental techniques developed for interstitial copper to nickel in silicon. 66
10 Summary and outlook 68
11 Publications supported by the subcontract XAF-8-17607-04 70
12 Acknowledgements 73
13 References 74

1 Executive summary

The subcontract XAF-8-17607-04 was focused on the understanding of precipitation of metal impurities in silicon, dissolution of the precipitates, their recombination properties, and passivation in order to gain a fundamental physical understanding of the impact of transition metals on solar cell efficiency. In particular, we wanted to get insight in the nature of gettering-resistant sites. These sites are often found in defect clusters in mc-Si, detrimental to mc-Si solar cell efficiency. It is known that these sites contain transition metals, which cannot be easily removed by gettering. This understanding is a key to developing efficient gettering and passivation techniques necessary to improve multicrystalline solar cell performance. Two metals, copper and iron, were studied in detail. These two metals were chosen because they are often mentioned as major metal impurities in photovoltaics. Additionally, they are good representatives for the whole group of 3d transition metals, which consist of the fast diffusing metals (which include Cu, Co and Ni) and the slower diffusers, such as Ti, V, Cr, Mn, and Fe.

The results of our work were presented at the 1999-2001 NREL workshops, NCPV program review meeting, and 2001 E-MRS meeting. They were published in over 30 articles in scientific journals and conference proceedings.

The major results and deliverables of the subcontract can be summarized as follows:

1. The **theoretical basis of Transient Ion Drift**, a novel technique for detecting interstitial copper in silicon, was developed by solving a system of coupled differential equations which describe diffusion and drift of copper in depletion regions of inverse-biased Schottky diodes. The results of these theoretical studies enabled us to quantitatively interpret the capacitance transients, observed in Transient Ion Drift Measurements [1]. TID was one of the major experimental techniques which were used for studies of Cu in silicon on the following stages of the subcontract.
2. The **intrinsic and effective diffusion coefficient of copper in silicon** were determined using the temperature-dependent Transient Ion Drift technique [2]. It is shown that the data of Hall and Racette [3], which were used for modeling copper diffusion in silicon for almost 25 years, underestimate the intrinsic copper diffusivity at room temperature by 3 orders of magnitude. Our data indicated that the intrinsic and effective diffusion coefficients of copper are given by the following equations:

$$D_{\text{int}} = (3.0 \pm 0.3)\times 10^{-4} \times \exp\left(-\frac{0.18 \mp 0.01\ \text{eV}}{\text{k}_\text{B} T}\right) \quad (\text{cm}^2/s)$$

$$D_{eff} = \frac{3\times 10^{-4} \times \exp(-2090/T)}{1 + 2.584\times 10^{-20} \times \exp(4990/T)\times(N_a/T)} \quad (\text{cm}^2/s)$$

where temperature T is measured in Kelvin and the boron doping level, N_a, in cm^{-3}.

This result shows that copper can easily diffuse through the thickness of a solar cell within a few hours at room temperature.

3. The unexpectedly high diffusivity of copper at room temperature enabled us to explain the **poor stability of point defects of copper** [4, 5]. The kinetic barrier for dissociation of complexes of copper with other defects and impurities in silicon consists of two components, equilibrium binding energy of the complex, and the diffusion barrier which interstitial copper has to overcome to dissociate the complex. Since the diffusion barrier of interstitial copper (0.18 eV, [2]) is much lower than the diffusion barrier of the other transition metals (e.g., 0.67 eV for iron, [6]), the total kinetic barrier for dissociation of Cu complexes is also much lower than that of the other metals. Therefore, most copper complexes easily dissociate at room temperature, thus allowing copper to diffuse towards more stable sinks, such as copper precipitates or the wafer surface.
4. In collaboration with the group of Prof. W.Schröter from the University of Göttingen (Germany), **the microscopic structure of copper-precipitates in silicon** was investigated by Transmission Electron Microscopy and was correlated with the electrical properties of the precipitates [7]. It was found that copper precipitates form defect-like states in the upper half of the silicon band gap, between approximately E_C-0.15 eV and E_C-0.35 eV. The charge state of the precipitates depends on the Fermi level position in the sample. In p-type silicon, where the Fermi level position lies below the electroneutrality level of the precipitates at approximately E_C-0.2 eV, the precipitates are positively charged [7, 8]. In n-type silicon, where the Fermi level lies at or above the electroneutrality level, the precipitates are either neutral or negatively charged. This finding was instrumental in understanding the kinetics of copper precipitation and recombination properties of copper precipitates (see below).
5. EBIC and SPV measurements of the samples with high density of copper-silicide precipitates revealed their extremely strong **recombination activity** [9]. We suggested that the defect band, which is located close to the midgap position, provides an efficient recombination channel for minority carriers. Additionally, the positive charge state of copper-silicide precipitates in p-type silicon attracts the minority charge carriers by creating a depletion region around the precipitate and increasing the minority carrier capture cross-section for electrons (minority charge carriers in p-Si) to a value greater than the actual size of the precipitate. Since the DLTS spectra of copper-precipitates are extremely wide, their amplitude does not give a straightforward estimate of the actual concentration of copper precipitates. Our estimates showed that the DLTS signal of Cu precipitates may drop below the detection limit at a concentration of copper precipitates which is still sufficient to limit the diffusion length to 30-50 μm [7, 10]. Of course, this applies to any type of precipitate, and may explain why DLTS and MCTS measurements performed on mc-Si by a large number of workers

never revealed deep traps in concentrations adequate to account for the low values of the minority carrier diffusion length.

6. The **electrostatic model of copper precipitation** in silicon was suggested and confirmed experimentally [11, 12]. It was shown that precipitation of copper in the bulk of the wafer is unlikely at low copper concentrations because of the large nucleation barrier for the formation of Cu precipitates, which is due to (i) strong compressive strain, caused by large volume expansion [13] during the formation of copper silicide, and (ii) electrostatic repulsion between the positively charged Cu-precipitates and the ionized interstitial Cu_i^+ [11, 12]. The charge state of copper precipitates is determined by the Fermi level position, which depends on the concentration of shallow acceptors (boron) compensated by shallow donors (mainly interstitial copper). If the interstitial copper concentration exceeds the boron concentration, conductivity type inversion occurs. As soon as the Cu_i^+ concentration becomes sufficient for the Fermi level to exceed the electro-neutrality level of the precipitates at approximately E_C-0.2 eV [7, 12], the charge state of copper precipitates changes from positive to neutral or negative, and the electrostatic precipitation barrier disappears or even changes sign to attraction. This facilitates nucleation and growth of multiple Cu precipitates in the bulk of a sample. In n-type silicon, a much lower Cu concentration is required to initiate nucleation of the precipitates since the Fermi level is close to the electro-neutrality level even for very low copper concentrations.

   This result implies that copper precipitates are more likely to be observed in the n-type areas of solar cells than in p-type areas. Formation of Cu precipitates in the area of the p-n junction may shorten it and decrease the overall efficiency of the cell [14].

7. The electrostatic barrier for copper precipitation was also observed in the studies of **the impact of copper contamination on minority carrier diffusion length,** where an increase in the effective density of recombination sites by several orders of magnitude was found at copper concentrations which, according to the electrostatic precipitation model, are required to initiate its efficient precipitation in the wafer bulk. In n-type silicon, the dependence of the effective density of precipitation sites on Cu concentration was nearly linear; however, the slope of this dependence was less than unity, indicating that the recombination activity of copper in n-Si is due to complexes consisting of at least several copper atoms. We concluded that low levels of copper contamination will not have a pronounced effect on minority carrier diffusion length in p-type silicon and hence will not significantly limit the cell efficiency (aside from the formation of Cu precipitates in th n-type areas of the cells, mentioned above). The availability of heterogeneous precipitation sites for copper (oxide precipitates) had a mild effect on the effective density of copper-related traps.

8. A weak **passivating effect of copper** was observed in p-type silicon at low copper concentrations. This effect was explained by a defect reaction similar to the reaction involved in hydrogen passivation, i.e., by the formation of complexes of Cu_i with recombination active defects with a

lower recombination activity than that of the defects before passivation. Although it is very unlikely that Cu passivation can replace hydrogen passivation, experiments with copper can be used to better understand the mechanisms of hydrogen passivation in solar cells, and vice versa.

9. X-ray **microprobe absorption spectroscopy studies of copper precipitates** in multicrystalline silicon did not reveal any phase other than copper silicide [15, 16]. The studies of the thermal stability of copper-silicide precipitates by the same technique showed that these precipitates can be fairly easily dissolved, although their dissolution kinetics was found to be somewhat slower that expected.
10. Study of the **thermal stability of iron-silicide precipitates** showed that these precipitates cannot be gettering resistant defects since they can be easily dissolved within less than a minute at temperatures above 800^0C. Therefore, metal-silicide precipitates, which can be extremely recombination active, are unlikely to form gettering-resistant sites in solar cells.
11. An extensive study of the literature data on iron in silicon [6, 17] showed that there are indications that iron may react with the dissolved oxygen by forming iron oxides and iron silicates. Studies of the **chemical nature of metal precipitates** in multicrystalline silicon, performed in collaboration with S.A.McHugo at the Advanced Light Source [15] confirmed that multicrystalline silicon indeed contains clusters of gettering-resistant iron oxides and silicates. These clusters may be responsible for dissolution-resistant metals-related intragranular defects, found in bad grains of mc-Si in the earlier studies of our group.
12. The feasibility of application of the **μ-XRF technique for characterization of fully processed solar cells** without any chemical cleaning or surface preparation was demonstrated. It was shown that the topography of the contact grid, visible in an optical microscope, secondary electron image, and XRF scans, can be used to find the areas of interest in XRF and EBIC tools, as well as in optical techniques and thermography.
13. The X-ray fluorescence technique was applied towards characterization of **metal impurities at the location of a shunt** in a solar cell [18]. A contamination by titanium, a slowly diffusing heavy metal, was detected at the location of the shunt. This metal can be introduced by the metal belt used on a production line. Since Ti has very low diffusivity in silicon, it is unlikely that it can be easily removed from the location of the shunt by gettering, particularly if this metal contamination was introduced on one of the last steps of solar cell fabrication.
14. A proof of principle for the possibility of in-situ identification of the chemical nature of recombination-active defects by a new technique, **X-ray Beam Induced Current (XBIC)**, was demonstrated [19]. In this technique, an X-ray beam focused to the size on the order of a square micron hits the surface of the solar cell and generates electron-hole pairs, which can be collected by the p-n junction to obtain an EBIC-like map of the recombination activity of defects present in the wafer. On the other hand, any other X-ray microprobe technique, such as X-ray fluorescence, can be

used to identify the chemical content of recombination sites observed in the XBIC scans. XBIC was successfully demonstrated in combination with XPS, and implementation of XBIC at the XRF beamline is planned in the near future.

15. An attempt to apply the TID technique for studies **of nickel in silicon** was made; however, no ion drift transients were observed, which indicates that nickel may be neutral at room temperature, and precipitates immediately after the quench.

The structure of the report is as follows. A brief introduction, which describes the state of knowledge before the beginning of the three-year subcontract and formulates the problems addressed in our research, is followed by two experimental parts. In the first part, the progress achieved in the understanding of copper and iron in silicon is presented. The second half of the report concentrates on the analysis of multicrystalline silicon, including the development of novel characterization methods for the study of transition metals in PV-grade silicon. After the experimental parts, we outline the research directions which our group would like to pursue in the future. The report concludes with a list of publications supported by this subcontract, and the list of references.

2 Introduction

The easy availability of electrical energy has always been the essential, if not principal prerequisite for the progress of technology and manufacturing. For many years, electrical energy was generated primarily from oil (39.8% of the 1998 world energy consumption), natural gas (22.5%), and coal (23.3%). However, since the world supplies of these resources are limited, sooner or later the power producers will have to find alternative means to generate electricity. Hydroelectric (7.1%) and nuclear (6.5%) power plants do not depend on natural resources to the same extent as oil, gas, and coal plants, but their impact on the nature (dams required to build a power plant), potential hazards in the case of accidents (release of radioactive materials) and problems with the storage of nuclear waste make it questionable whether hydro or nuclear power can replace the conventional sources of electricity. Renewable energy, primarily solar, geothermal, and wind energy, which at the present time account for only 0.7% of the world production of electricity, are considered by many true alternatives to the conventional energy sources. The production of solar panels showed impressive growth at a steady 25% per year since the late 1980s. The advantages of photovoltaics (PV) are many: solar generators are environmentally friendly, do not consume natural resources, and can be installed either at centralized power plants or on the roofs of individual houses. However, the use of photovoltaics has been limited by high cost of the systems and consequently high cost of generated electricity. The most expensive component of a PV system are solar panels, which are usually made of single crystalline or polycrystalline silicon. For the same lighting conditions, the generated power is proportional to the product of the area of a solar panel and its efficiency. Although high crystalline quality Czochralski (CZ) and float zone (FZ) wafers enable one to achieve very high cell efficiency, the cost of the integrated circuit (IC)-grade substrates is prohibitively expensive. Much effort has been invested in the development of cost-efficient technologies for growth of either lower quality CZ substrates, or multicrystalline silicon substrates suitable for photovoltaics. These technologies are primarily based on rapid solidification, whereby silicon is pulled or casted in the shape of thin substrates (to avoid the costly and material-consuming step of sawing the crystal) at much higher pulling rates than utilized for CZ or FZ growth, used in the production of silicon for integrated circuit applications. Unfortunately, the efficiency of solar cells fabricated on mc-Si wafers grown by these technologies (typically 10-13%) proved to be significantly lower than that of the cells made of single crystalline silicon (up to 21-23%).

There are two major classes of defects which are present in multicrystalline substrates in much greater concentration that in crystalline silicon (such as CZ or FZ grown): impurities and lattice defects. Mc-Si contains a significantly higher concentration of metals and a much higher density of grain boundaries, dislocations, and microscopic structural defects, than monocrystalline silicon. The concentration of metals is higher in PV mc-Si primarily because the PV technology uses fast pulling/solidification rates and cannot benefit from the effect of segregation of impurities in the silicon melt during growth to the same extent as CZ of FZ technology. Two recent neutron activation analysis (NAA) studies of mc-Si used for fabrication of solar cells revealed that it contained 10^{12} cm^{-3} to 10^{15} cm^{-3} of metals, including Al, Ca, Fe, Mn, Ti [20, 21]. For comparison, high quality CZ silicon typically contains less that 10^{10} cm^{-3} of metal impurities. This difference in metal content is in a good agreement with the typical segregation coefficient of transition metals between crystalline phase and the melt. Lattice defects such as grain boundaries or dislocations are thought to be weak recombination centers when they are clean [22, 23]. However, it is very unlikely to find a clean dislocation in mc-Si since dislocations are efficient gettering sites which collect metal impurities thus becoming efficient recombination centers.

Other types of defects which are present in much higher concentrations in mc-Si than in crystalline silicon are grain boundaries, dislocations, and intragranular microdefects. The latter type of defect was detected in mc-Si in iron precipitation [24-26] and x-ray fluorescence mapping [27] experiments, reported by our group in 1994-1996, and in TEM studies reported by Werner et al. [28] in 1997. The microdefects appear to be effective precipitation sites for transition metals [24-26]. It was shown [24-26] that the precipitation rate of iron was slow in "good grains", while in "bad grains" iron precipitated at a much faster rate. Furthermore, degradation of the minority carrier diffusion length in "bad grains" was much stronger than in "good grains" [22-24]. It was suggested that the major difference between the "bad grains" and the "good grains" was that the "bad grains" contained a higher concentration of intragranular defects, which serve as efficient precipitation sites for iron [29]. Very little was known about the nature of these microdefects, the binding energy of metals to these defects, or the types of trapped metals. The strong binding energy of metals to these defects was suggested to explain poor improvement of lifetime in "bad grains" after gettering. The high density of these precipitation sites, particularly in grains with low minority carrier diffusion length, and the strong binding of metals to the precipitates are thought to be the reason for the low effectiveness of standard gettering techniques.

The studies done by the UC Berkeley group in the framework of this subcontract is a part of the NREL research program in fundamental materials science, focused on understanding the phenomena which limit the efficiency of multicrystalline solar cells. The goal of the program as a whole is to develop improved materials and processes in order to narrow the efficiency gap between multicrystalline and single crystalline solar cells. The objective of our subcontract was to understand the role of metal impurities in the formation of defect clusters in solar cells and to study the process of their precipitation, dissolution, gettering and passivation. The experiments were performed using iron and copper as model impurities in silicon. Both crystalline and multicrystalline silicon were used.

PART 1. Fundamentals of copper and iron in silicon

3 Diffusion, defect reactions, and recombination properties of copper in silicon

3.1 Determination of intrinsic and effective diffusion coefficients of copper in silicon

Copper is one of the most ubiquitous impurities in silicon device production [30]. The electrical and structural properties of copper in silicon are still poorly understood despite intensive research during the last 30 years (see, e.g., Istratov and Weber [10] for a review). Even such a fundamental property of *Cu* in *Si* as its diffusion coefficient remains uncertain. Unlike most other 3d transition metals, copper diffuses in silicon in the positively charged state [31]. The theory of diffusion of positively charged ions in the presence of immobile acceptors was developed by Reiss *et al.* [32]. They showed that, due to the processes of trapping and releasing of mobile donors by immobile acceptors, the effective (apparent) diffusivity D_{eff} of donors in *p*-type material is lower than their diffusivity D_{int} in the intrinsic material. In the case of $N_D<<N_a$ it is given by $D_{eff} = D_{\text{int}}/[1+\Omega N_a]$, where N_a is the acceptor concentration, N_D is the concentration of mobile donors and Ω is the pairing constant. The pairing constant can easily be calculated theoretically if the interaction potential between copper and shallow acceptors is known. The simplest (and incorrect, as it is shown below) approximation for the attraction potential, used in the previous studies, was electrostatic (Coulomb) attraction.

The first data point on copper diffusivity was obtained on intrinsic silicon by Struthers [33]. Later, temperature-dependent measurements were made by Hall and Racette [3] on heavily boron doped *p*-type *Si* (N_a=5×10^{20} cm^{-3}). Assuming negligible copper-acceptor pairing, Hall and Racette [3] suggested the expression $D=4.7\times10^{-3}\times exp(-0.43\ \text{eV}/k_BT)\ cm^2s^{-1}$, which was later widely used as the intrinsic copper diffusion coefficient in silicon (see, e.g., [30]). Keller *et al.* [34] were the first to suggest a correction to the Hall and Racette's data to take into account pairing of *Cu* with acceptors and to extract the intrinsic diffusion coefficient. They used a simple Coulomb attractive potential for *V(r)* and obtained a copper diffusivity of $D=3\times10^{-3}\times exp(-0.15\ \text{eV}/k_BT)\ cm^2s^{-1}$. Mesli et al. [35] argued that the treatment of Keller et al. [34] is incorrect since a high doping level requires use of a screened Coulomb potential, and suggested a corrected diffusion coefficient of $D = 5\times10^{-3}\times exp(-0.40\ \text{eV}/k_BT)\ cm^2s^{-1}$. Later, Heiser *et al*. [36] measured the effective copper diffusivity in *In* and *Ga*-doped *p-Si* around room temperature by Transient Ion Drift (TID) technique. Plotting the corrected data from [3] and their own estimates of copper diffusivity at low temperature [36] on the same plot, Mesli *et al*. [37] suggested the expression $D=4.5\times10^{-3}\times exp(-0.39\ \text{eV}/k_BT)\ cm^2s^{-1}$.

The studies discussed above were made on *p*-doped silicon and consequently only an effective diffusion coefficient of copper was measured. The intrinsic diffusion coefficient was estimated by assuming a Coulomb interaction between *C*u ions and acceptors [34-37]. This model implies that the potential energy of donor-acceptor interaction *V(r)* should depend only on the acceptor charge state and not on its chemical nature. Yet, recent experimental studies of the copper-acceptor dissociation energy reported by Wagner *et al.* [38] revealed that the dissociation energy is different for different types of acceptors (0.61 eV for *CuB*, about 0.70 eV for *CuAl*, *CuGa* and *CuIn* and 0.85 eV for *CuPt*), thus indicating that the binding in these pairs has a covalent (or strain) component. This conclusion is

in agreement with the theoretical calculations reported by Estreicher [39]. As follows from the results presented below, the assumption of a purely Coulomb interaction [35-37] resulted in an underestimation of the pairing constant Ω by more than an order of magnitude and the previously published 'intrinsic' diffusion data need to be reconsidered.

One of the accomplishments of the first year of the subcontract was the development of a new experimental procedure to accurately determine the intrinsic diffusivity of copper in silicon in the temperature range between 240 and 380 K. Measurements were done by Transient Ion Drift (TID) [36] technique, which is essentially similar to Deep Level Transient Spectroscopy (DLTS, [40]). However, the capacitance transients are due to drift of charged ions rather than emission of charge carriers. The time constants of the capacitance transients bear information on diffusivity of the drifting ions. To be able to accurately extract the diffusion coefficient of copper from our transient ion drift experiments, we developed an exact model of transient ion drift obtained by solving a system of coupled differential equations. This model describes the ion drift across a reverse biased Schottky diode, assuming a constant diffusion coefficient, *D*, a diffusion-limited trapping of the mobile ions (or solute) at the doping impurities, and a thermal dissociation of neutral solute-dopant pairs. We also assumed that the majority carriers (holes) and solute ions (Cu_i^+) carry the same electrical charge, that the background doping is uniform, and that Einstein's relation between the ion mobility, μ, and its diffusion coefficient, *D*, holds.

The solute density, $N_{sol}(x,t)$, obeys the following equations:

$$N_{sol}(x,t) = N(x,t) + P(x,t) \tag{1}$$

$$\frac{\partial N(x,t)}{\partial t} = \frac{\partial}{\partial x}\left[D\frac{\partial N(x,t)}{\partial x} + s\mu N(x,t)\frac{\partial V(x,t)}{\partial x}\right] - \frac{\partial P(x,t)}{\partial t} \tag{2}$$

$$\frac{\partial P(x,t)}{\partial t} = 4\pi R_c D N(x,t)[A_{tot} - P(x,t)] - \nu P(x,t) \tag{3}$$

$$\frac{\partial^2 V(x,t)}{\partial x^2} = -\frac{q}{\varepsilon_s}\left\{ N_{sol}(x,t) - A_{tot} + [A_{tot} - N_{sol}(L)] \times e^{-\frac{q[V(x,t)-V(L)]}{kT}} \right\} \tag{4}$$

where $N(x,t)$ and $P(x,t)$ are the concentrations of unpaired and paired solute atoms, respectively, A_{tot} is the total doping density, $V(x,t)$ is the distribution of electrical potential, R_c is the capture radius, ν is the dissociation rate of the pairs, *q* is the ion charge, ε_s is the semiconductor dielectric constant, *L* is the sample thickness, *k* is the Boltzmann constant, *s* is the sign of the ion charge state and *T* is the temperature. The backside solute density, $N_{sol}(L)$, is supposed to be time independent. The meaning of Eq. 1 is that the total copper concentration is given by the sum of its paired and unpaired fractions. Eq.(2) describes thermally activated diffusion and drift in the electric field and includes a recombination term to take pairing into account. Eq.(3) represents the solute-dopant interaction and takes into account the diffusion-limited capture rate, and Eq.(4) is the Poisson equation. For boundary conditions, we assume no solute flux on both sample surfaces and equilibrium of the pairing reaction on the backside surface. The latter assumption is accurate as long as the sample thickness, *L*, is considerably larger than the space-charge region (SCR) width. The total constant voltage drop is given by $\Delta V = V(0) - V(L) = V_{bi} + V_{ext}$, where V_{bi} is the Schottky diode built-in voltage and V_{ext} is the externally applied bias. The potential origin is chosen at the sample backside surface (i.e., $V(L)=0$).

In TID measurements, the signal acquisition starts when the applied voltage is changed from V_{pulse} to V_{rev}, increasing the depletion region width. Typically, V_{pulse}=0 V and V_{rev}=5 V. We consider that instant as the origin of the time scale. If the pulse voltage was applied long enough, the system has reached a stationary state by t=0. Concentration of the solute atoms in the depletion region is then negligibly low, while in the neutral region, a uniform solute density in equilibrium with the pairing reaction has been established. We may thus approximate the initial solute distribution, $N_{sol}(x,0)$, by:

$$N_{sol}\left(x \le W_{pulse}, 0\right) = 0 \; and \; N_{sol}\left(x > W_{pulse}, 0\right) = \overline{N}_{sol} \tag{5}$$

where W_{pulse} is the width of the SCR under V_{pulse}, with the pairing reaction at thermal equilibrium. $\overline{N}_{sol}$ is the average solute density in the bulk, which is equal to $N_{sol}(L)$ and taken to be lower than the doping level. The ion distribution will affect the SCR width and hence the depletion capacitance $C(t)$. Baccarani *et al*. [41] have proposed an analytical model to derive the Schottky diode capacitance for arbitrary doping profiles. According to this model, the depletion capacitance per unit area, $C(t)$, can be related to the solute density by:

$$\Delta V = -\frac{1}{\varepsilon_s}\int_0^{W(t)} x \cdot \rho(x,t)dx + \frac{kT}{q}\left\{\ln\left[\frac{\rho(W,t)}{\rho(L,t)}\right] - \frac{W(t)}{\rho(W,t)}\left.\frac{d\rho}{dx}\right|_{W(t)} - 1\right\} \tag{6}$$

$$\rho(x,t) = q \cdot \left[N_{sol}(x,t) - A_{tot}\right] \tag{7}$$

and

$$C(t) = \frac{\varepsilon_s}{W(t)} \tag{8}$$

where $\rho(x,t)$ represents the space charge density, and $W(t)$ the depletion width. The term in curly brackets in Eq.(6) takes into account the difference between free carrier and space charge distributions. Eqs. (1)-(4) were solved with the finite difference method implemented by the software package 'ZOMBIE' [42]. A detailed discussion of the solution found in this study and its implications for the analysis of Transient Ion Drift data can be found in our publication, Ref. [1]. Briefly, a very good agreement between the experimentally observed and theoretically predicted capacitance decays was found. In particular, we found that the characteristic time constant of TID capacitance transient, τ_{TID}, can be well described by analytical expression derived from a simplified model of transient ion drift [2], if two correction coefficients, α=2.85 and β=1.95, are introduced as follows:

$$\tau_{TID} = \alpha \times \frac{\varepsilon\varepsilon_0 k_B T}{q^2 N_a D_{\text{int}}} + \alpha \times \beta \times \tau_{diss} \tag{9}$$

The first term on the right-hand side of Eq.(9) describes the average drift time of unpaired copper ions through the depletion region. The second term describes the dissociation of copper-acceptor pairs. These equations were obtained for $N_D \ll N_a$. In the framework of the semi-empirical model of TID [36], the coefficient α assigns to τ_{TID} the time needed by a diffusing ion to cover about

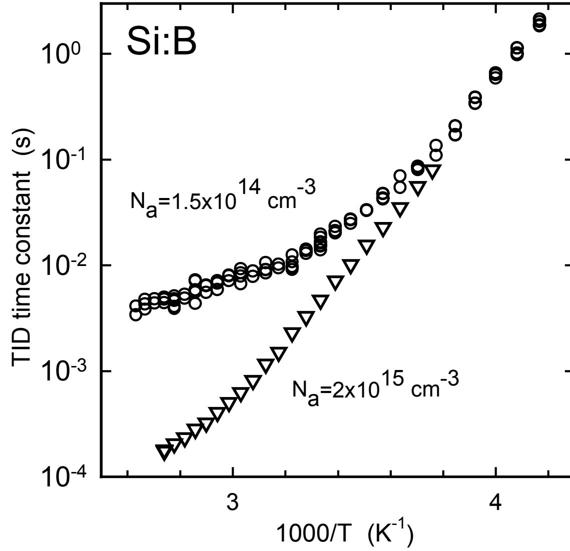

Fig.1. Experimentally measured dependence of the TID time constant on temperature for boron-doped silicon with the doping levels of 1.5×10^{14} cm^{-3} (circles) and 2×10^{15} cm^{-3} (triangles).

95% of its distance to the edge of the space charge region. Coefficient β takes into account non-equilibrium of the pairing process in the depletion region of a Schottky-diode.

Although Eq. (9) requires the knowledge of D_{int} and of the dissociation rate of the copper-acceptor pairs τ_{diss}^{-1}, it does not require the explicit knowledge of the attractive potential $V(r)$ between Cu_i^+ and B^-. The process of trapping is characterized by a capture radius R_C, which is calculated from the condition that the average thermal energy k_BT equals the attractive potential energy $V(r)$, i.e., $k_BT=V(R_C)$. Since in most cases R_C is as large as several *nm*, the covalent component of the ion interaction can be neglected and $V(R_C)$ can be approximated by a screened Coulomb potential. If $\tau_{TID}>>\alpha\times\beta\times\tau_{diss}$, the pairing is weak and the TID time constant is determined primarily by the intrinsic drift of copper ions through the depletion region. The intrinsic diffusivity D_{int} can in this case be determined directly from the experimental data as follows:

$$D_{\text{int}} = \frac{\alpha\varepsilon\varepsilon_0 k_B T/(q^2 N_a)}{\tau_{TID} - \alpha\times\beta\times\tau_{diss}} \tag{10}$$

An important conclusion that follows from Eq.(10) is that if the first term on the right-hand side of Eq.(9) is small compared to the second one, i.e., $\tau_{TID}\approx\alpha\times\beta\times\tau_{diss}$, then the pairing is strong and the denominator in Eq.10 becomes arbitrary close to zero. In this case, the information on the intrinsic diffusion coefficient contained in the dependence $\tau_{TID}(T)$ drops below the measurement errors and D_{int} cannot be extracted unambiguously from the experimental data. The conditions of strong pairing, $\tau_{TID}\approx\alpha\times\beta\times\tau_{diss}$, and weak pairing, $\tau_{TID}>>\alpha\times\beta\times\tau_{diss}$, can be distinguished by the slope of the temperature dependence of τ_{TID}. This is illustrated in Fig. 1, which presents the temperature-dependent TID measurements done on boron-doped silicon with acceptor densities of 1.5×10^{14} cm^{-3} and 2×10^{15} cm^{-3}. In the low-doped samples (Fig.1, circles) a change of the slope in the temperature dependence of τ_{TID} is observed between T=255 K and T=310 K. The pairing of copper with boron is dominant at T<255 K (1000/T>3.92), while above T=310 K (1000/T<3.22) the slope is limited by the intrinsic diffusion process. For the boron doping level of $N_a=2\times10^{15}$ cm^{-3} the dependence $\tau_{TID}(T)$ is

determined by pairing with boron up to the temperature of about 320 K (1000/T=3.125) (Fig.1, triangles). Eq.9 can be used to determine the time constant of *CuB* dissociation at temperatures where the pairing is strong, and Eq. 10 to determine the intrinsic copper diffusion coefficient at the higher temperatures. Using these two data sets between 240 K and 320 K, the following expression for the *CuB* dissociation rate was obtained:

$$\tau_{diss}^{-1}(T) = (2.05 \pm 0.80) \times 10^{13} \times \exp(-\frac{0.61 \pm 0.01\, eV}{k_B T}) \tag{11}$$

This expression is very close to the one reported by Wagner *et al.* [38]. The intrinsic diffusivity of copper calculated using Eqs.10 and 11 for the samples with N_a=1.5×10^{14} cm^{-3} in the temperature range between 265 K and 380 K is presented in Fig.2 as an Arrhenius plot. A linear regression to our data alone gives $D_{int}=(1.7\pm0.4)\times10^{-4}\times exp(-0.165\pm0.015\ \mathrm{eV}/k_BT)\ cm^2s^{-1}$. To expand the temperature range in which the diffusion coefficient is valid, we made a least square fit to our data together with the data obtained on intrinsic silicon at 1173 K by Struthers [33]. This yields the following expression for the interstitial copper intrinsic diffusion coefficient:

$$D_{\mathrm{int}} = (3.0 \pm 0.3) \times 10^{-4} \times \exp(-\frac{0.18 \mp 0.01\, \mathrm{eV}}{\mathrm{k_B} T}) \quad (\mathrm{cm}^2 / s) \tag{12}$$

which is valid in the temperature range between 265 K to 1173 K and can be considered as the most accurate expression for the intrinsic copper diffusivity in silicon reported up to now. The intrinsic diffusion barrier of 0.18 eV in Eq.(12) is close to the value of 0.24 eV, recently predicted by Woon *et al.* [43] from the molecular dynamics simulations.

Fig.2. Intrinsic diffusion coefficient of copper determined from our experimental data (N_a=1.5×10^{14} cm^{-3}) in the temperature range 265 to 380 K (circles) and experimental data point reported by Struthers (open triangle).

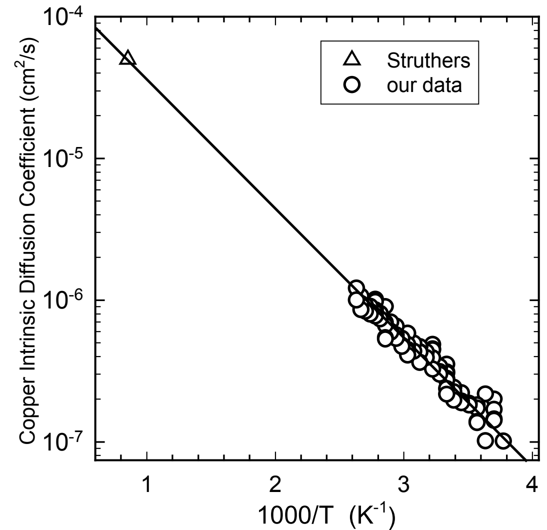

We would like to emphasize that Eq.(12) describes the copper diffusivity in the absence of copper-acceptor pairing and is valid only in intrinsic or *n*-type silicon, provided that no other trapping processes exist. In *p*-type material, however, it is the effective diffusivity D_{eff} which describes copper diffusion and which is relevant for all practical applications. D_{eff} can be either determined

experimentally, e.g., from TID measurements (see Ref. [2] for more details), or calculated theoretically as follows:

$$D_{eff}(N_A,T) = D_{\text{int}} / \left[1 + 4\pi \times \beta \times D_{\text{int}} R_C N_a \tau_{diss}\right] \qquad (13)$$

where τ_{diss} and D_{int} are given by Eqs.(11) and (12), respectively. The capture radius R_C is determined by either simple or screened Coulomb radius, depending on the doping level and the temperature. As discussed above, the coefficient β reflects non-equilibrium capture conditions in the depletion region during TID measurements and should be set to unity for bulk measurements. Inserting the constants, Eqs.(11) and (12), and an expression for R_C into Eq.13, we obtain a convenient numerical equation for effective diffusion coefficient in moderately boron-doped ($N_a \le 10^{17}$ cm^{-3}) silicon:

$$D_{eff} = \frac{3\times 10^{-4} \times \exp(-2090/T)}{1 + 2.584\times 10^{-20} \times \exp(4990/T) \times (N_a/T)} \qquad (14)$$

In Fig.3 we present the effective copper diffusivity for different doping levels calculated using Eqs. 12, 13, and 14 with β=1 (bulk diffusion). Also presented are the effective copper diffusivities experimentally determined from TID measurements using samples with two different doping levels, and the data of Hall and Racette. The different values used for β (unity for the bulk, and 1.95 for TID junction measurements) lead to a slight deviation between curves 2,3 in Fig. 3 and the experimental points at temperatures where pairing is dominant. The calculations agree over the whole temperature range not only with the data used for the determination of D_{int}, but also with the data measured in the medium doped material ($N_a = 2\times 10^{15}$ cm^{-3}). Since Hall and Racette's data points are close to the calculated dependence (curve 5), the agreement between our model and experimental data extends over the doping level range from 1.5×10^{14} to 5×10^{20} cm^{-3}. This agreement also confirms that the Hall and Racette data represent the effective diffusion coefficient for $N_a = 5\times 10^{20}$ cm^{-3}, and explains their significant deviation from the intrinsic diffusivity curve. Furthermore, since the effective diffusion coefficient depends nonexponentially on temperature (see Eqs. 13,14), the exponential expression suggested by Hall and Racette can be used only as an approximation in the temperature range where the data points were taken and may result in significant errors if extrapolated outside of this range.

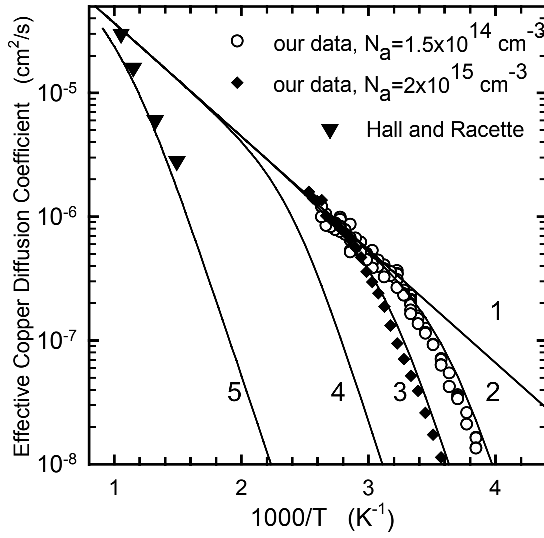

Fig.3. Effective diffusion coefficient of copper in silicon calculated for different boron doping levels (lines) and experimental data obtained in this study (circles, N_a=1.5×10^{14} cm^{-3} and diamonds, N_a=2×10^{15} cm^{-3}) and by Hall and Racette (triangles, N_a=5×10^{20} cm^{-3}). Curve 1 - intrinsic silicon, curve 2 - N_a=1.5×10^{14} cm^{-3}, curve 3 - N_a=2×10^{15} cm^{-3}, curve 4 - N_a=1×10^{17} cm^{-3}, curve 5 - N_a=5×10^{20} cm^{-3}.

3.2 Point defect reactions of copper in silicon

It is well known from literature that copper does not form electrically active point defects in appreciable concentrations. It has been reported (see Ref. [10] for a review) that the total density of electrically active copper-related defects usually does not exceed 10^{-3} of the total copper concentration dissolved in the sample. Since this fraction is not constant and may vary depending on the type of the wafer and its thermal history, it is impossible to determine the total copper concentration from DLTS or EPR measurements. The reason of low probability of formation of point defects was difficult to understand until the correct diffusion barrier for copper in silicon was determined.

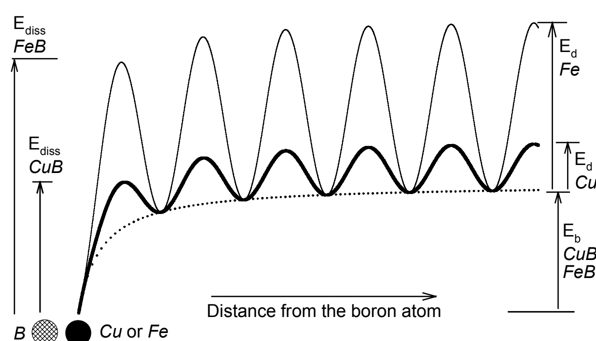

Fig. 4. A schematical potential diagram which represents the energy for dissociation of *CuB* and *FeB* pairs. Even if the interaction potentials between *Cu-B* and *Fe-B* are identical, higher diffusion barrier of interstitial iron makes *FeB* pairs much more stable than *CuB* pairs.

It is well known that the barrier which an impurity atom (e.g., copper) has to overcome to dissociate from a defect (which can be another impurity atom, a dislocation, or a precipitate) is determined by two components: (i) the depth, E_b, and the shape of the attractive potential between the impurity and the defect, and (ii) the height of the diffusion barrier, E_d, for the impurity (Fig. 4). To obtain a rough estimate of the dissociation energy of a pair, E_{diss}, some researchers add the diffusion barrier height, E_d, to the binding energy, E_b: $E_{diss} \approx E_b + E_d$. Since accurate data on the binding energy of defects in silicon are rarely available, the binding energy of a donor-acceptor pair in silicon (i.e., a pair which consists of a negatively charged and a positively charged ion, located at a substitutional and the nearest interstitial lattice sites, respectively, with purely electrostatic interaction between them) is frequently used as an approximation for E_b, E_b=0.52 eV. The diffusion barrier for Cu_i is 0.18 eV, whereas for most other *3d* transition metals it is greater than 0.6 eV (e.g., 0.67 eV for Fe_i). Therefore, an estimate for the dissociation energy would be 0.7 eV for *CuB* pairs and 1.2 eV for *FeB* pairs. The experimental data are fairly close to these estimates: the dissociation energy of *FeB* pairs was reported to lie between 1.14 and 1.40 eV [44, 45], whereas for *CuB* pairs it is as low as 0.61 eV [2, 38, 46]. Consequently, *CuB* pairs are unstable even at room temperature and dissociate within milliseconds, whereas *FeB* pairs can be dissociated only by heating the sample up to 200^0C [47]. Since the diffusion barrier height, E_d, affects the dissociation energy of not only *CuB* pairs, but of all other *Cu* complexes and agglomerates, it explains the poor stability of *Cu* complexes in silicon. As complexes of *Cu* with other impurities and defects dissociate very easily, they cannot permanently trap copper, but rather only slow down its diffusion until copper finds more stable sinks. These sinks can either be extended defects in the bulk of the wafer (copper-silicide precipitates, dislocations, grain boundaries), or wafer surface.

3.3 Precipitation behavior of copper in silicon

Since copper has a very high diffusion coefficient even at room temperature, while its equilibrium solubility, extrapolated to room temperature is negligibly small [30, 31], it can not be "frozen in" in the interstitial position by a rapid cooling to room temperature, and diffuses to stable sinks during or quickly after the quench. Thus, the resulting recombination activity of copper is determined by the properties (and location in the crystal) of its complexes and precipitates, rather than by the properties of the interstitial copper itself. As discussed in the previous section, copper is unlikely to form stable point defect complexes. Therefore, Cu precipitates and agglomerates should determine the electrical properties of Cu in silicon.

Precipitation of copper in the bulk and in the near-surface region of the silicon wafers was extensively studied starting from the 1980s (see, for example, Schröter *et al*. [48] and references therein, or the recent review by Seibt *et al*. [49]). At slow cooling rate (air cooling, 1 to 25 K/s), copper forms colonies of precipitates in the near-surface regions [50-52]. At fast cooling rate (quench, >100 K/s), when copper does not have time to diffuse to the surface, and when huge supersaturation caused by rapidly decreasing temperature forces it to precipitate, it precipitates in the bulk [53].

Copper precipitate colonies can be detected by preferential etching of Cu-diffused wafers [52]. TEM investigations [52, 54-56] revealed that the size of precipitate colonies can range from 0.5 to 80 μm, and they protrude up to 40 μm into the bulk of a Si wafer. The colonies consist of small particles forming planar arrangements parallel to Si {110} and sometimes {001} planes. The colonies are usually bounded by edge-type dislocation loops. The diameter of the particles varies between about 7 nm (even values as low as 1 nm have been reported [57]) in the vicinity of the dislocation loops and 20 nm for precipitates at least 50 nm away from the bounding dislocation. Copper-based colonies show high recombination activity - Correia et al. [57] recorded EBIC contrast as high as 93% on a colony. The model of growth of planar precipitate colonies by a repeated nucleation process on climbing edge dislocations has been proposed by Nes et al. [51, 55, 56, 58] based on a mechanism described by Silcock et al. [59].

After a fast quench, copper forms precipitates in the bulk of silicon in the form of thin platelets, lying mainly in the {111} planes. The size of the platelets depends on the cooling rate [53] and usually varies between 20 and 600 nm. Independent of the cooling rate, the platelets are surrounded by strong deformation fields. The atomic structure of the precipitates is not certain. Seibt reported [53] that after a fast quench copper formed copper-silicide islands, surrounded by thin extended defects, similar to stacking faults. The earliest stages of copper precipitation investigated so far are characterized by platelets with a thickness of only two or three lattice planes [7, 60]. Larger and thicker precipitates, which were not surrounded by stacking faults, were reported by Kajbaji [61].

A typical TEM micrograph obtained using the equipment available at National Center for Electron Microscopy on a Cu-precipitate in p-type silicon, obtained after copper diffusion at 850^0C terminated by quench, is presented in Fig. 5. Contrasts surrounding the precipitate are indicative of strong strain fields. These strain fields are associated with much larger molecular volume (volume of a cell with one silicon atom) of copper silicide, Cu_3Si, than that of silicon: 46 $Å^3$, as compared to the molecular volume of silicon of 20 $Å^3$ [13, 48]. This means that approximately 1.3 silicon interstitials should be emitted for each silicon atom forming copper-silicide (the other way to say it is that precipitation of 2.3 copper atoms emits 1 silicon interstitial). High-resolution TEM image presented in Fig. 6 enabled us, using advanced TEM image processing techniques, to determine that precipitates are surrounded by misfit dislocations. The precipitates observed in n-type samples had very similar

morphology to those observed in p-type silicon.

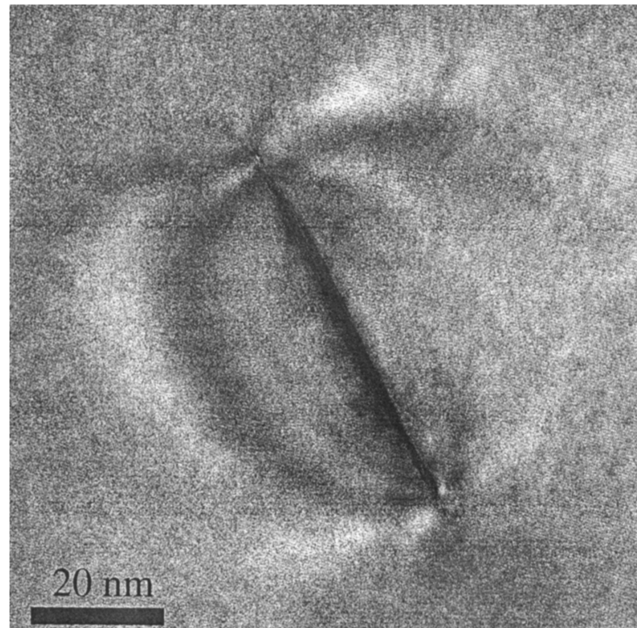

Fig. 5. (111) platelet of copper silicide in p-type silicon after in-diffusion at 850^{0}C as observed with TEM.

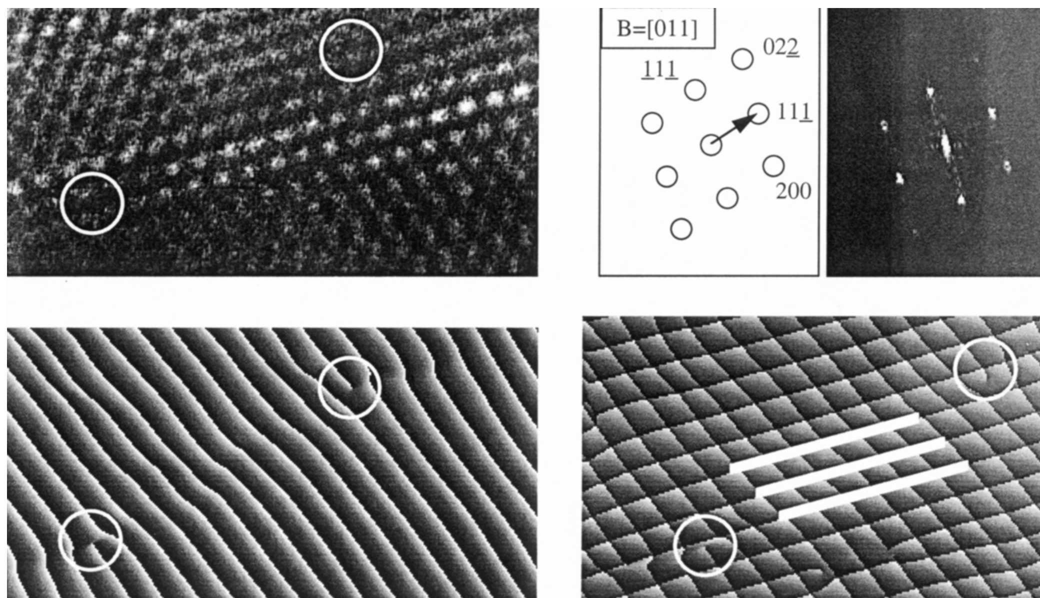

Fig. 6. High resolution TEM image of a copper silicide platelet in p-type silicon. The Fourier transform of the image in the top left corner of the figure was used to calculate the atomic distance of the 111 lines crossing the platelet and to exactly determine the location of the lattice planes. The method clearly highlights the misfit dislocations surrounding the precipitate.

Interestingly, the size, orientation, and morphology of Cu-silicide precipitates were found to be very similar to one of the types of intragranular defects, reported by Werner et al. [28] (see Fig. 7).

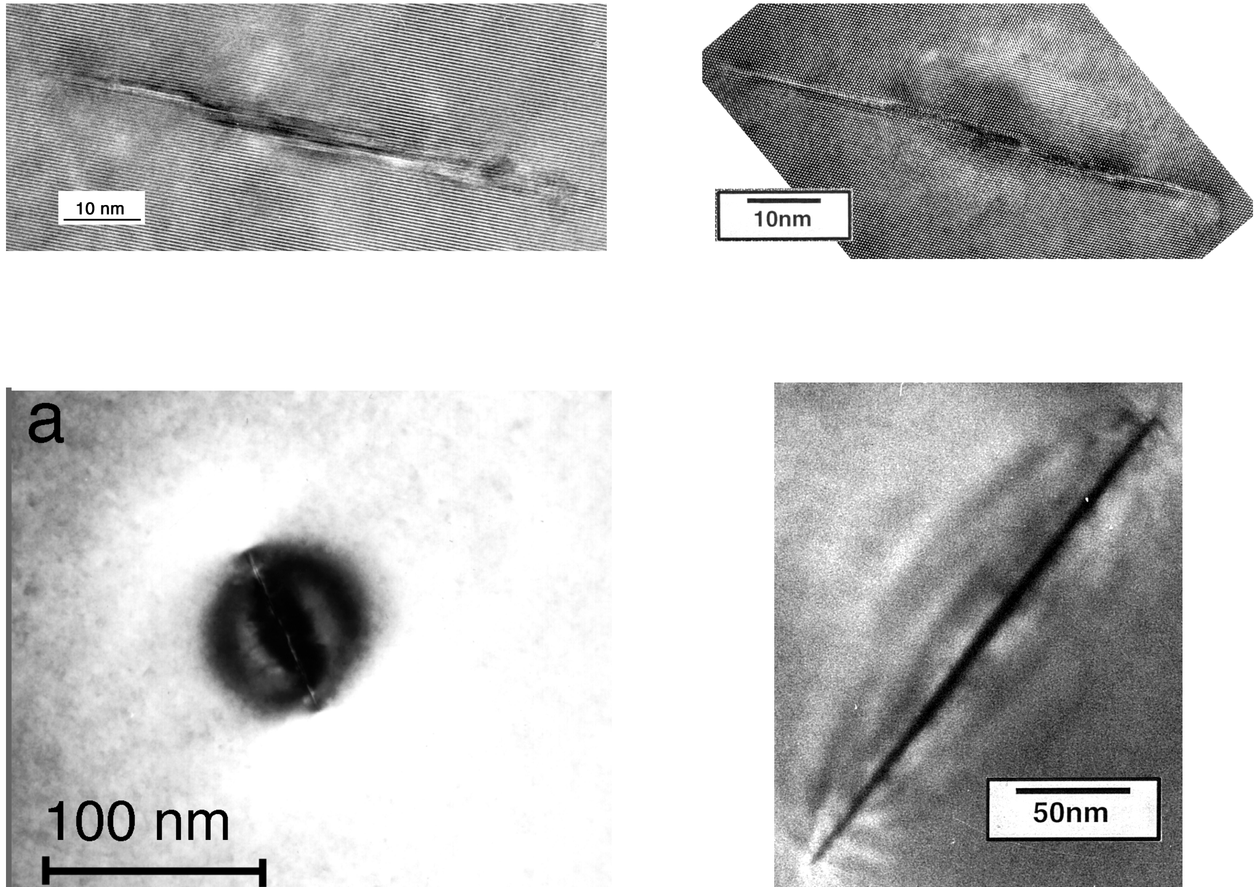

Fig. 7. A comparison of a TEM image of an intragranular microdefect, observed by Werner et al. [28] (left-hand side of the figure) in a sample of mc-Si which was not intentionally contaminated, with a copper-silicide precipitate (right-hand side of the figure). Close similarity of TEM images of both defects suggests that Cu precipitates may be one of the types of intragranular defects.

DLTS measurements of Cu-contaminated samples, performed in collaboration with the group of Prof. Schröter from the university of Göttingen (Germany), allowed us to gain insight in the electrical properties of the precipitates. A typical DLTS spectrum of *Cu*-silicide precipitates in *n-Si* after copper diffusion at 850^0C and rapid quench in 10% NaOH solution is shown in Fig.8. Note the extremely unusual, almost rectangular shape of the peak, and its extremely large width. The amplitude and the shape of the peak correlated with the initial Cu concentration and the cooling regime. The observation that the peak shifted along the temperature axis as a whole when the DLTS rate-window was varied (see Fig. 8) was interpreted as an indication that this peak was associated with a defect band in the silicon band gap rather than with overlapping levels of point defects. Numerical modeling of DLTS spectra of bandlike states (see Refs. [7, 62, 63]) revealed that both the

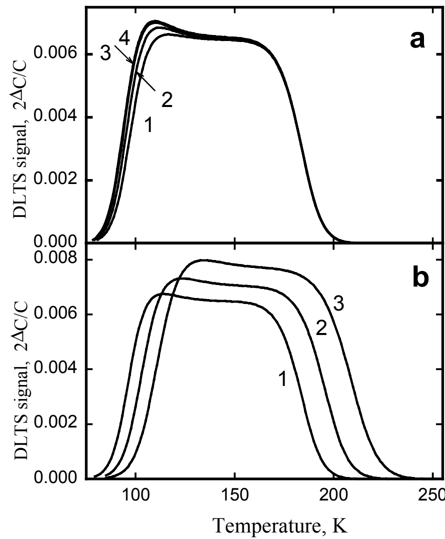

Fig.9. Simulated pulse width and correlation frequency variations for a band-like defect with a box-like distribution of levels between E_C-0.15 eV and E_C-0.35 eV.

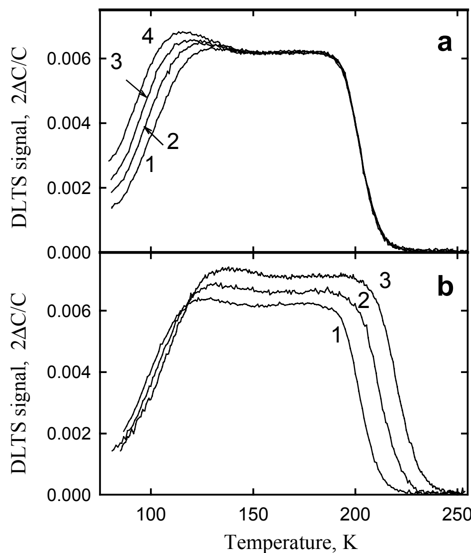

Fig. 8. DLTS spectra of Cu-precipitates in n-Si. The diffusion of copper was performed at 850^0C and then terminated by quench in 10% NAOH solution. a) filling pulse width variation, t_p = 30 µs (curve 1), 300 µs (curve 2), 3 ms (curve 3) and 30 ms (curve 4); the spectra were taken with the sinusoidal lock-in correlation frequency f=1.907 Hz. b) sinusoidal lock-in correlation frequency variation: curve 1 - 1.907 Hz, curve 2 - 7.63 Hz, curve 3 - 30.52 Hz; filling pulse width t_p=100 µs.

shape of DLTS spectra presented in Fig.8 and their dependence of DLTS filling pulse duration and rate-window can be explained assuming that (a) copper-silicide precipitates form a defect band between approximately E_C-0.15 eV and E_C-0.35 eV, and (b) the copper-silicide precipitates are electrically amphoteric, i.e., they are positively charged when empty and negatively charged when filled up to about 80-100%. Fig. 9 represents the results of computer simulation of DLTS spectra of bandlike states, which are in a good agreement with the experimental spectra of copper-silicide precipitates.

Minority carrier diffusion length analyses of samples with copper precipitates indicated that copper-silicide precipitates are extremely active recombination centers. The diffusion length in both *n-Si* and *p-Si* samples quenched from 850^0C was less than 2.5 µm for NaOH quenched samples and on the order of 13-15 µm after silicone oil quench, which results in the formation of a lower density of larger precipitates. Comparison with the diffusion length studies on samples where copper has not yet precipitated [64] indicated that the same concentration of copper is by far more recombination active when it is precipitated than when it is in the interstitial state. Extrapolation of the experimental data from [7] to lower concentrations of copper suggests that copper precipitates will control the diffusion length in PV silicon at the level of several tens of microns even if the concentration of precipitated copper is about 10^{12} to 10^{13} cm^{-3}. Thus, copper precipitates form strong recombination centers which may control the lifetime in PV silicon (see Sec. 3.5 below for further analysis of the recombination properties of copper). The next question that was addressed in our research was to understand where the recombination-active copper-silicide precipitates are likely to form in the wafer, and what conditions are most favorable for their formation.

3.4 Electrostatic model of precipitation behavior of copper in silicon

This section will present the results which enabled us to conclude that the charge state of copper affects not only its diffusion, but also its precipitation in the bulk of silicon.

It has been assumed for a long time that the supersaturated copper precipitates completely after cooling down the sample. However, recent experimental data suggested that this is not the case. There were indications in the literature that precipitation of interstitial copper is retarded in *p-Si*. Heiser *et al.* [36, 65] were the first to report that contrary to the common belief, copper does not precipitate immediately during or after a rapid quench, but remains interstitial for at least several hours. One can easily calculate using Eqs.(12,14) that during this time copper ions can typically diffuse through half of the wafer thickness. The work of Shabani *et al*. [66] provided additional evidence that in some cases copper may not completely precipitate in the wafer. They showed that after a week almost all copper diffuses out from *p-Si* wafers contaminated with copper to the level of $10^{13} - 10^{15}$ cm^{-3} to the wafer surface, provided the surface oxide was removed. This observation was confirmed by the similar studies of McCarthy et al. [67]. No out-diffusion was detected in *n-Si* [66] unless the wafer was heated to 400^0C.

At first glance, the finding that Cu does not immediately precipitate in p-Si may appear quite surprising since the chemical driving force for precipitation of supersaturated copper, $\Delta f = k_B T \ln(C / C_0)$, where C is the concentration of supersaturated copper, and C_0 is its equilibrium solubility, can be as high as 0.7 to 0.9 eV at room temperature. Unlike iron, which gets trapped by shallow acceptors and forms *FeB* pairs, thus reducing the concentration of supersaturated Fe_i to its equilibrium level, *CuB* pairs are unstable at room temperature and cannot serve as efficient sinks for supersaturated copper. For instance, it is easy to calculate that about 20% of the total Cu_i concentration remains in the free interstitial state in 10 Ωcm silicon at room temperature.

Lattice strain is clearly one of the factors that determine the precipitation behavior of copper in silicon. Indeed, the large (150%, see [13, 48]) lattice expansion during formation of copper-silicide can be responsible for this potential barrier: adding each next copper atom to the existing precipitate increases the strain, which is relieved by emission of a silicon self-interstitial for each two precipitated copper atoms. A very rough estimate shows that the energy gain due to precipitation of two copper atoms, which is on the order of 2 eV, depending on the copper supersaturation level, is compensated by about 4 eV which it takes to generate a silicon self-interstitial [68]. The remaining precipitation barrier, which can be as high as 1 eV per copper ion, is sufficient to decrease the precipitation rate of copper to very low levels. Since the surface usually represents a good sink for self-interstitials, the strain-related barrier for copper precipitation can be expected to be lower in the near-surface regions or be completely absent if copper diffuses out of the wafer bulk and ends up at the surface. Likewise, local tensile strain, or the presence of efficient sinks for generated silicon-self-interstitials (such as dislocations, possibly even punched out by copper silicide precipitates themselves) may decrease the stress-related precipitation barrier. An interesting example of this effect was presented by Kissinger *et al.* [69], who showed that the morphology and location of copper precipitates colonies not only depended on the local stress at $Si/Si_{0.98}Ge_{0.02}$ interface, but also reflected the density and location of misfit dislocations. Although the existence of a stress-related barrier explains the slow bulk precipitation of the interstitial copper, the difference in outdiffusion and recombination properties of copper in *n-Si* and *p-Si* discussed above indicated that electrical effects (such as effects determined by the Fermi level position in *n-Si* and *p-Si*) may also be involved.

Below, we present experimental evidence that such effects indeed play a role in the precipitation and recombination behavior of copper.

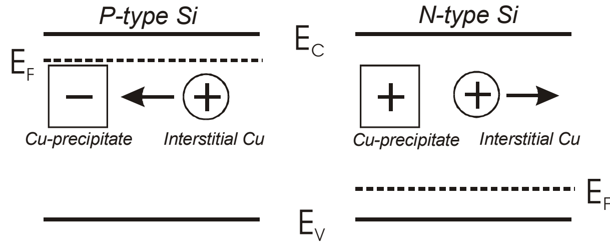

Fig. 10. An illustration of the effect of the electrostatic interaction between positively charged copper ions and growing copper precipitates on copper precipitation kinetics in *p-Si* and in *n-Si*.

The understanding that not only interstitial copper ions, but also copper-precipitates are positively charged in *p*-type silicon (see the discussion in Sec. 3.3 above), enabled us to hypothesize that it is the electrostatic repulsion between the positively charged nuclei of copper precipitates and positively charged copper ions that increases the stress-related barrier for copper precipitation to the level sufficient to completely suppress the precipitation of copper in *p*-type silicon. On the contrary, in *n*-type silicon the copper precipitates are neutral or negatively charged, and there is either no significant electrostatic repulsion between Cu_i^+ and *Cu* precipitates, or even electrostatic attraction that enhances precipitation. This electrostatic model is sketched in Fig. 10. It is important to notice that the transition from repulsive to attractive electrostatic potential is determined by the Fermi level position, which is affected not only by the concentration of shallow dopants such as boron or phosphorus, but also by the concentration of Cu_i^+. If the concentration of copper is higher than that of shallow acceptors, then an inversion of the conductivity type of the sample from *p*- to *n*-type will occur. This raises the Fermi level to a position close to the bottom of the conduction band, thus changing the charge state of copper-silicide precipitates and enhancing the precipitation of copper. One can than expect that (a) there should be a threshold copper concentration in *p-Si*, which has to be reached to remove the electrostatic component of the precipitation barrier, and (b) that this threshold copper concentration should increase with the increasing boron doping level as the Fermi level position is determined by both Cu_i^+ and B_s^- concentration.

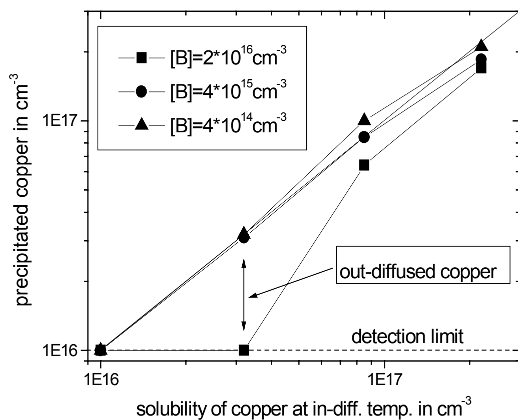

Fig. 11. Precipitated copper concentration measured with XRF plotted vs. the solubility of copper at in-diffusion temperature for the samples with three different doping levels.

To test our model of electrostatic effects on the kinetics of copper precipitation in *p-Si*, we investigated precipitation of copper in samples with different initial copper concentrations and different boron doping levels. Interstitial copper concentrations have been measured within 30 minutes after the quench with the Transient Ion Drift (TID) technique [1, 65]. The concentration of precipitated copper in the bulk was measured by synchrotron-based X-Ray Fluorescence (XRF) after removal of the near-surface layer of the sample. The XRF measurements were performed at beamline 10.3.1 at the Advanced Light Source of Lawrence Berkeley National Laboratory in collaboration with S.A.McHugo (see, e.g., [70] for the details of the technique). We used our standard procedure [2, 65] to diffuse copper, quench the sample, and prepare Schottky diodes for TID measurements. The initial copper

concentration was determined by the indiffusion temperature. The decay of the interstitial copper concentration during room temperature storage was monitored using the Transient Ion Drift technique. A complete disappearance of the TID signal observed after several days of room temperature storage indicated that all the copper has found stable sinks either in the bulk, or at the surface. The concentration of *Cu* that has precipitated in the bulk was measured by the XRF technique after removing the surface layer chemically. The concentration of the outdiffused copper could not be measured directly, and was calculated as the difference between the measured concentration of precipitated copper, and the equilibrium Cu solubility at the diffusion temperature. Since we could not distinguish Cu trapped in the native oxide from copper, precipitated in the near-surface area of the sample, the term "outdiffusion" is used in this section in a broader meaning than suggested by Shabani [66] and includes both of these two sinks for copper. Additionally, both values were compared with the interstitial copper concentration, determined by TID after the quench. An example of such comparative measurement by TID and XRF is presented in Fig. 11. The ratio of the outdiffused copper and the copper precipitated in the bulk depended on the initial copper concentration and the boron doping level. The fraction of the outdiffused copper varies from nearly zero to about 70% depending on the experimental conditions. In the case when outdiffusion to the surface (a relatively slow process limited by copper diffusivity) was dominant, TID measurement taken within 30 min of room temperature storage after the quench could detect nearly all indiffused copper in the interstitial state. On the contrary, in the case when bulk precipitation was dominant, a significant fraction of copper would precipitate during the time required to fabricate Schottky diodes, and the interstitial copper concentration detected by TID was much lower than expected. Detailed TID studies on three series of samples with different boron doping levels and with different initial *Cu* concentrations revealed that the onset of the bulk *Cu* precipitation is reached only at a *Cu* concentration which depends on the doping level of the samples. While these threshold *Cu* concentrations were found to vary with the boron doping level of the sample, the Fermi level position corresponding to the threshold copper concentrations was the same for all samples (Fig. 12). This indicated that the mechanism of this threshold effect was correlated with the Fermi level position in the sample. The critical Fermi level position was found to be at approximately E_C-0.2 eV, which matches the electroneutrality level of the copper precipitates (see [7]). This confirms the model that the growth of copper precipitates is determined by the electrostatic interaction between Cu_i^+ and *Cu* precipitates, as illustrated in Fig. 10.

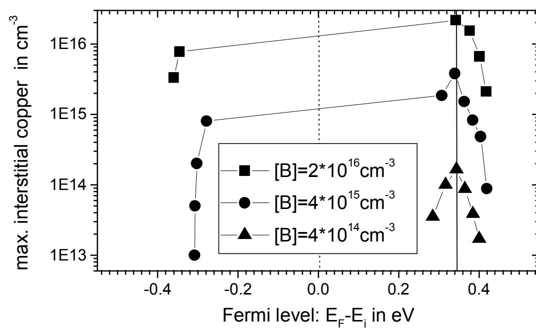

Fig. 12. Maximum interstitial copper concentration as measured with TID for samples with three different doping level plotted vs. Fermi level position immediately after quench to room temperature.

For an initial copper concentration lower than the acceptor concentration, the Fermi level is in the lower half of the band gap and rises slowly with increasing copper contamination. When the copper concentration exceeds the doping level, the conductivity type changes from p- to n-type. However, this is not yet sufficient to change the precipitation behavior of copper (see Fig. 12). Only when the Fermi level exceeds the critical value of about E_C-0.2 eV, does Cu precipitation take place. When the copper concentration is below the critical level, the precipitates (or their

nuclei) are positively charged, and Coulomb repulsion inhibits precipitation of the positively charged interstitial copper ions. If the copper concentration exceeds the critical concentration, the Fermi level rises above the neutrality level, the charge state of copper precipitates changes and precipitation can occur (see Fig. 10). However, during precipitation the Fermi level decreases as the concentration of interstitial copper ions decreases, and the precipitates turn positively charged again. This significantly slows down the precipitation and enables out-diffusion of the rest of the interstitial copper atoms. In *n*-type silicon with a sufficiently high doping level the Fermi level remains above the neutrality level of the precipitates for any copper concentration and precipitation is the dominant process to decrease the supersaturation of interstitial copper at room temperature.

The fast copper precipitation rate in *n-Si* explains why no one was able to actually detect the conductivity type inversion after copper diffusion – the excessive *Cu* concentration precipitates too fast to be detected. Furthermore, the suppression of the bulk copper precipitation in *p-Si* enabled us to understand the conditions of the complete outdiffusion of copper to the wafer surfaces, reported by Shabani *et al.* [66] and McCarthy *et al.* [67].

3.5 Study of the recombination activity of copper in n-type and p-type silicon: copper as a lifetime killing impurity at high copper concentrations.

Although the detrimental impact of copper on semiconductor device yield was recognized already in 1960 by Goetzberger and Shockley [71], literature data on the impact of copper on minority carrier diffusion length remained controversial until now. It was found [72-78] that intentional Cu contamination up to the level of 10^{11}-10^{13} cm^{-3} had very little or no effect on the minority carrier lifetime in p-type silicon, or even improved it, whereas high copper concentrations inevitably led to significant degradation of minority carrier diffusion length [7]. In contrast, a strong effect of Cu on lifetime in n-Si was observed even at low Cu contamination levels [74, 79, 80]. To the best of our knowledge, a consistent explanation was offered neither for this difference in recombination activity of copper in n-Si and p-Si, nor for its weak impact on lifetime in p-Si at low Cu concentrations.

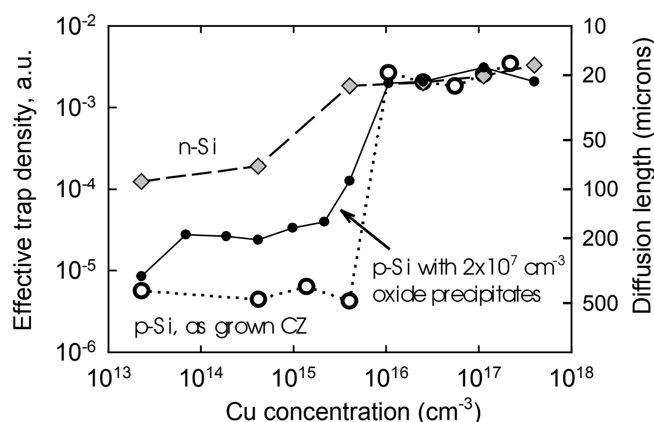

Fig. 13. Dependence of minority carrier diffusion length on Cu contamination level in 10 Ohm-cm FZ-grown n-Si samples (diamonds), in 10 Ohm-cm p-Si, as-grown CZ (open circles) and with 2×10^{7} cm^{-3} of internal gettering sites (black circles). The IG site density was determined from optical precipitates profiler measurements.

In this section, we present results of systematic experimental studies of the impact of copper contamination on minority carrier diffusion length in n-type and p-type as-grown Czochralski (CZ) silicon with different doping levels, and in p-type silicon with internal gettering sites, and suggest a model to explain the observed dependencies.

Copper diffusion in CZ-grown p-type silicon was performed in the temperature range between 450^{0}C and 950^{0}C for sufficiently long time to reach the equilibrium solubility of copper. For comparison, similar diffusions were performed using n-type silicon. Due to the lack of suitable CZ-grown n-type samples, float-zone grown n-type Si samples were used. Both n-type and p-type silicon samples had resistivities of 10 Ω-cm. Copper was chemically deposited on the sample surfaces by dipping them into dilute copper-fluoride solution. Diffusion anneals were performed in a vertical furnace in nitrogen ambient and were terminated by a quench in silicone oil. After the quench, samples were chemically cleaned, etched, and stored for several days at room temperature before measurements to allow all defect reactions of copper to go towards completion. The minority carrier diffusion length was determined by the surface photovoltage technique using the CMS-IIIA system by Semiconductor Diagnostics (SDI). The results of the SPV measurements are presented in Fig. 13. We found it instructive to plot the data in Figs. 13-15 against the effective density of recombination sites, which is proportional to $1/L^{2}$, where L is the minority carrier diffusion length. This proportionality holds because according to the Shockley-Read-Hall statistics, the density of recombination centers is proportional to $1/\tau$ (assuming that there is only one predominant type of lifetime limiting defects in the sample), whereas the minority carrier lifetime, τ, is proportional to L^{2}. The corresponding values of the minority carrier diffusion length, L, are given in Figs. 13-15 on the right vertical axis.

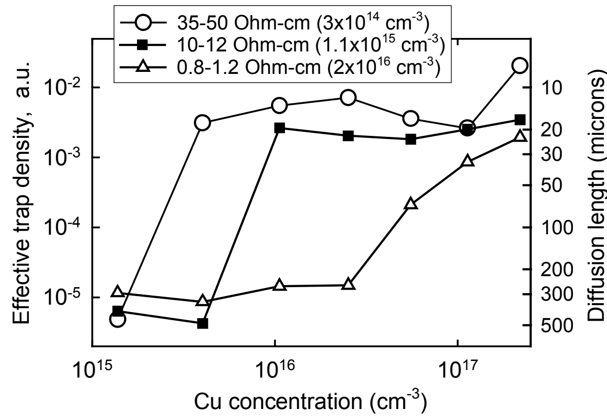

Fig. 14. Dependence of minority carrier diffusion length on Cu contamination level in p-type silicon samples with different boron doping level.

Fig. 13 presents three curves, one for n-type silicon, and two for p-type silicon, as grown CZ and with internal gettering (IG) sites. Initially, our discussion will be confined to the curves obtained on the n-Si (diamonds) and p-Si without intentionally formed IG sites (open circles). It is seen from Fig. 13 that in n-type silicon, the effective density of recombination centers increases almost linearly with the indiffused Cu concentration, whereas in p-type silicon, the effective density of recombination centers remains very low at low Cu concentrations and experiences a sharp increase at a Cu concentration of approximately 10^{16} cm^{-3}. This critical Cu concentration matches the threshold concentration of copper that has to be reached in 10 Ω×cm p-Si to start forming Cu-precipitates in the bulk (see Sec. 3.4 above). This suggests that a step in the effective trap density, observed in the curves plotted in Fig. 13, is associated with the onset of the formation of Cu precipitates in the bulk of the samples. These precipitates are efficient recombination centers for charge carriers. Indeed, EBIC measurements of our samples, mentioned in Sec. 3.4 above, indicated that Cu precipitates are very efficient recombination centers [9]. This can be explained by a combination of two factors, the positive charge of Cu precipitates in p-Si, which increases their capture cross-section for minority charge carriers, and the effective recombination of these charge carriers through the bandlike states associated with Cu precipitates [7, 11]. Therefore, it is reasonable to assume that the step in minority carrier lifetime (Fig. 1) is caused by recombination of the charge carriers at copper precipitates. These precipitates are formed at high density as soon as the Fermi level position in the sample reaches the electroneutrality level, thus reducing the total barrier for nucleation and growth of Cu precipitates.

To further test this model, we investigated the effect of Cu on minority carrier diffusion length for samples with three different resistivities (35-50 Ohm-cm ($\langle B\rangle=3\times10^{14}$ cm^{-3}), 10-12 Ohm-cm ($\langle B\rangle=1.1\times10^{15}$ cm^{-3}), and 0.8-1.2 Ohm-cm ($\langle B\rangle=2\times10^{16}$ cm^{-3})). This experiment enabled us to compare the minority carrier diffusion length in samples with the same starting copper concentration, but with different Fermi level position. Results are presented in Fig. 14, which shows that the position of the step in the effective density of recombination sites depends on the doping concentration. A higher concentration of Cu is required to cause the step-like transition in the effective density of recombination sites in the samples with a higher boron doping level. However, the position of the room-temperature Fermi level calculated for the moment immediately after the quench is the same for all three types of samples, see Fig. 15. This allows us to conclude that all three samples have experienced the same dominant defect reaction, which determines the observed step in the efficient density of copper-related recombination sites: the formation of copper precipitates which starts as soon as Fermi level reaches the electroneutrality level of copper precipitates.

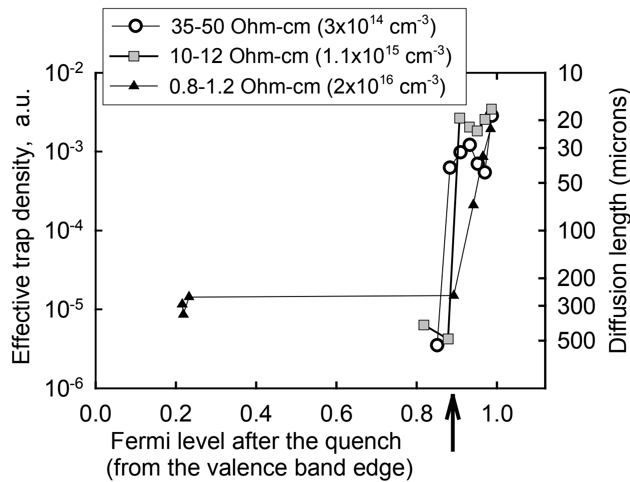

Fig. 15. The same data as in Fig.14, plotted against Fermi level position in the sample at room temperature immediately after the quench. The Fermi level position was calculated assuming that all copper is in the ionized interstitial state. The range of the horizontal axis corresponds to the bandgap with of silicon at room temperature. The arrow indicates the position of the electroneutrality level of copper precipitates.

This result provides a confirmation of the electrostatic model of Cu precipitation in silicon [11, 12] and explains the step-like dependence of minority carrier lifetime on Cu concentration in p-type Si. At low copper concentrations, very few precipitates are formed in high crystalline quality p-type silicon. As discussed in our recent publications [4, 5], complexes of interstitial copper are unstable, and outdiffusion of copper to the wafer surface is the predominant defect reaction of Cu in p-type silicon. Since only a small fraction of Cu is left in the bulk, its impact on minority carrier diffusion length is small, and may even result in passivation of electrically active defects, if complexes of Cu with these defects are less recombination active than the original defects. However, when the critical copper concentration is reached, copper starts forming recombination active precipitates everywhere in the bulk. As these precipitates are very efficient lifetime killers, the minority carrier diffusion length decreases drastically. In n-type silicon, the Fermi level is very close to the electroneutrality level of copper precipitates, and nucleation of copper precipitates occurs much easier. Therefore, the effect of copper on minority carrier lifetime at low copper concentrations is greater in n-Si than in p-Si.

Even with this qualitative understanding, the details of the behavior of copper and, consequently, its effect on the lifetime on the quantitative level may vary from wafer to wafer, depending on its thermal history, concentration of lattice defects and other impurities in the wafer, and its surface condition. It is instructive to compare two dependencies, taken on boron-doped CZ samples with the same resistivity with (filled circles, Fig. 13) and without (open circles, Fig. 13) IG sites. The curve obtained on the sample with IG sites shows the same step-like behavior as the curve obtained on as-grown CZ sample, but the step is much smoother and its height is lower. This can tentatively be explained by heterogeneous precipitation of copper at lattice defects (e.g., dislocations or stacking faults) associated with the oxide precipitates, which results in a small increase in the effective trap density at sub-critical Cu concentration range between 10^{13} and 10^{15} cm^{-3}. As the Cu concentration reaches $10^{16}cm^{-3}$, the effective trap density becomes approximately equal to that for as-grown CZ sample. This indicates that precipitation of Cu at oxide precipitates does not seem to be playing a significant role in determining the minority carrier diffusion length at copper concentrations above the critical copper concentration.

Finally, we would like to point out that the slope of the nearly linear dependence obtained for n-type silicon in Fig. 13 (diamonds) suggests that the copper-related recombination centers consist of more than one atom of copper. Recombination at centers which consist of a single impurity atom should follow a proportional dependence between the metal concentration and the effective density of

precipitation sites, whereby doubling of metal concentration doubles the concentration of recombination sites. In contrast, the increase in Cu concentration by over four orders of magnitude results only in an increase in efficient density of recombination sites in n-Si by about a factor of 20 (see Fig. 13). This confirms our hypothesis that the minority carrier diffusion length is limited in n-Si by agglomerates of copper. This is reasonable also because it is known that interstitial copper is a very shallow donor, which, according to Shockley-Read-Hall statistics, is expected to have very weak recombination properties, and cannot account for such a strong effect (similar to that of iron) of Cu on minority carrier diffusion length in silicon.

3.6 Impact of copper on minority carrier diffusion length in n-Si at low copper concentrations.

In this section, we report data observed on samples contaminated with low concentrations of copper (around 2.3×10^{13} cm^{-3}). We observed that, in contrast to high copper contamination levels, low copper concentrations can even improve the minority carrier diffusion length in the p-type samples.

In this study, we used a variety of samples, including as-grown float-zone (FZ) and Czochralski (Cz) grown silicon, Czochralski-grown samples with dissolved oxygen (CZdo), and Czochralski-grown samples with different densities of oxide precipitates (Si6, Si7). Our standard procedure was used for sample preparation, with the only difference that a slow ramping down was used to achieve the equilibrium copper concentration at the diffusion temperature below 550^0C. Namely, copper diffusion was initially performed at 650^0C for 30 min, and then the temperature was decreased step-wise, by 50^0C every 30 min, to the required indiffusion temperature. The 650^0C step was intended to assist with the formation of copper-silicide at the sample surface, which then served as the boundary phase necessary to reach the equilibrium copper solubility at lower temperatures.

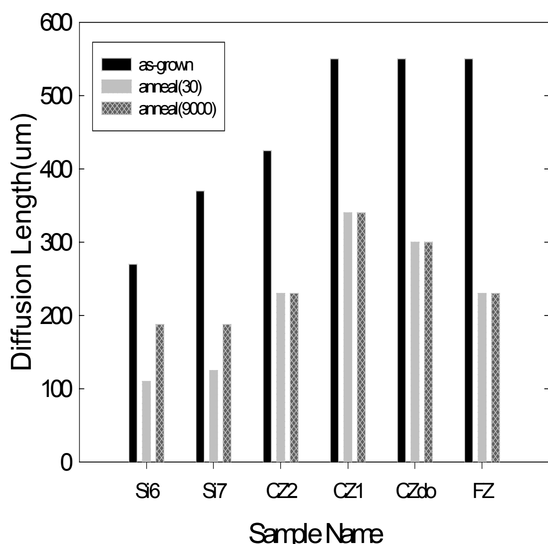

Fig. 16. Diffusion length for six different silicon samples before and after anneal without copper. The diffusion length for these samples was measured as grown (AG). Then samples were annealed at 450°C for 30min and then quenched at RT. Anneal(30) refers to anneal sample whose diffusion length was measured 30 min after quench. Anneal(9000) refers to same sample as Anneal(30) measured 9000 min after quench.

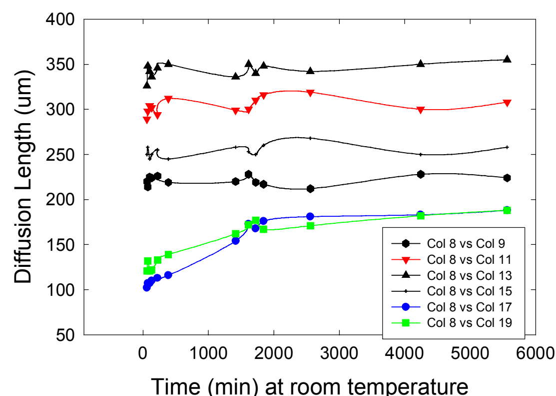

Fig. 17. Diffusion length vs. time after a 450°C treatment for 30 min and subsequent quench. FZ is float zone, CZdo is a CZ sample which was annealed at high temperature to dissolve oxygen precipitates, CZ1 and CZ2 are standard Czochralski wafers, Si6 and Si7 has $8.9\text{x}10^6$ cm^{-3} and $1.1\text{x}10^7 cm^{-3}$ oxide precipitates.

In the first step of this experiment, we studied how the minority carrier diffusion length changes after annealing the sample in a furnace without an intentional copper contamination. Fig. 16 shows a vertical bar chart for diffusion length of noncontamined silicon samples annealed at 450°C for 30 min

and subsequently quenched at RT. The diffusion length is then measured at two different time intervals after quench. There is a drop in diffusion length after anneal, as compared to the diffusion length before the anneal (see Fig. 16), which is most probably due to residual unintentional metal contamination. This metal contamination could be introduced either during cleaning, or during annealing in the furnace. Since our diffusion furnace is not located in a clean room, a certain background contamination level (at or below 10^{11} cm^{-3}) can be expected.

It is interesting to note that in two of the samples, namely Si6 and Si7 (silicon with a density of 8.9×10^{6}cm^{-3} and 1.7×10^{7}cm^{-3} oxide precipitates respectively), an increase in diffusion length is observed over time (Figs. 16, 17). This increase could be explained by a defect reaction caused by unintentional metal contamination, for instance by the association of FeB pairs. The change in the minority carrier diffusion length after annealing and quench is routinely used in SPV technique to determine the iron concentration in the wafers [47]. Application of the observed change in diffusion length corresponded to a Fe_i^+ concentration of about 10^{11} cm^{-3}.

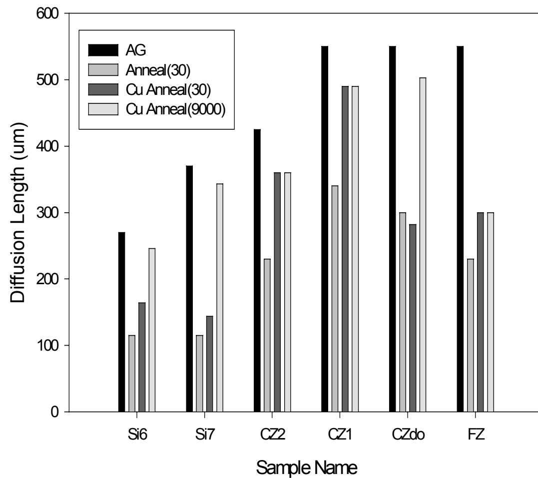

Fig. 18. Diffusion length observed on different types of samples for different anneal procedures. AG refers to as grown/received samples measured without any annealing procedure. Anneal(30) refers to non-contaminated samples annealed at 450°C for 30min. Cu Anneal(30) refers to anneal Cu contaminated samples whose diffusion length was measured 30 min after quench. Cu Anneal(9000) refers to same sample as Anneal(30) measured 9000 min after quench

DLTS experiments on sample Si7 confirmed the presence of [Fe_i^+]≈10^{11}cm^{-3}. Since the reaction of FeB formation with the inherent increase in the diffusion length was observed only on samples Si6 and Si7, but not on as-grown CZ samples or FZ samples, it is proposed that Si7 wafer samples have an unintentional iron contamination which occurred before we received them in our lab. This unintentional contamination was indeed a complication in our experiments. However, since Cu concentration in experiments with intentional Cu contamination was several orders of magnitude higher than the background Fe concentration, the impact on lifetime of silicon was expected to dominate due to Cu, not Fe_i^+. This assumption was confirmed experimentally, as shown in Figs. 18-20.

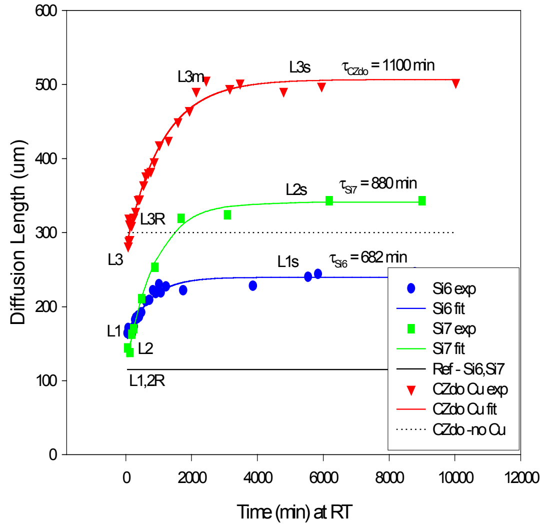

Fig. 19. Diffusion length vs. time after a 450°C treatment for 30 min and subsequent quench. L1, L2, L3 are the diffusion length values 30 min after quench. L1s, L2s, L3s are the steady state values of diffusion length. L1,2R and L3R are the reference values.

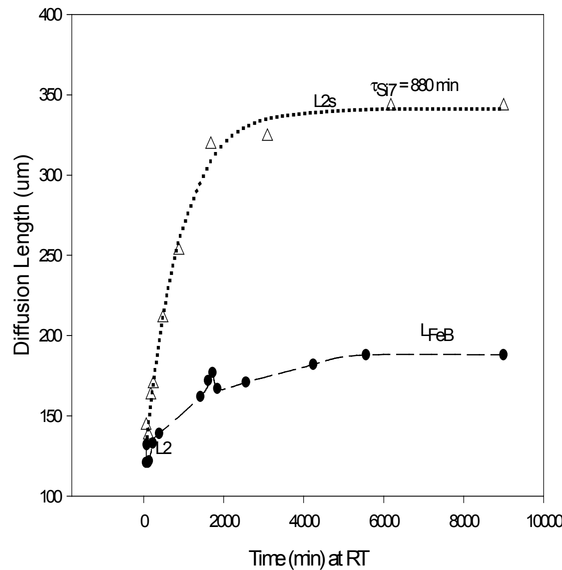

Fig. 20. Diffusion length vs. time after a 450°C treatment for 30 min and subsequent quench. This figure compares amplitude of the transients observed in samples with only unintentional iron contamination, and with Fe and Cu contamination combined.

As shown in a vertical bar graph in Fig. 18, low level of Cu contamination (diffusion at 450^0C, which corresponds to the equilibrium Cu solubility of 2.3×10^{13} cm^{-3}) generally increases the minority carrier diffusion length to a value, which is higher than the diffusion length observed in the samples which were subjected to the same heat treatment and quenching, but without any copper contamination. Measurement of time dependence of minority carrier diffusion length revealed transients shown in Fig. 19.

An increase in diffusion length as a function of time at RT is observed for the samples with oxide precipitates namely Si6, Si7 and the CZdo sample. The time constants calculated for each of the transients are shown on the graph.

Fig. 20 clearly shows that the amplitude of minority carrier diffusion length transients, observed in Cu-contaminated samples, is much greater than the iron-related transients observed in samples which were not intentionally contaminated with Cu. The two curves in Fig. 20 correspond to two of the Si7 silicon samples (containing $1.7\text{x}10^7$cm^{-3} oxide precipitates), one of which received a non Cu contaminated anneal treatment of 450°C for 30 min and the second one received a Cu contaminated for the same temperature and time. Both of the curves show a rise in diffusion length but the sample contaminated with copper shows a greater rise than the one not contaminated with copper.

Thus, it is clear that the presence of low concentrations of copper compensates the detrimental effect of other defects and impurities and increases the minority carrier diffusion length in the samples. This confirms observations previously reported in literature [74, 79, 81]. Since interstitial copper is somewhat similar to hydrogen (i.e., it is also a fast diffuser in silicon and is

positively charged), we think that its compensating effect is also similar to that of hydrogen, i.e., interaction of interstitial copper with recombination-active defects in silicon results in the formation of less recombination active complexes. This process is facilitated by the fact that interstitial copper is a very shallow donor, and it is much less recombination active that the rest of 3d transition metals [64]. As long as interstitial copper gets trapped by other impurities and the lattice defects, it has either little effect on minority carrier diffusion length, or even passivates the existing defects. As soon as it starts forming precipitates and agglomerates, which are extremely recombination active, the passivating effect of copper changes to a detrimental lifetime limiting effect. The time constant of the change in minority carrier diffusion length (see the curve in Fig. 20) is in a reasonable agreement with characteristic time constants of "disappearance" of interstitial copper from the sample in the reactions of its outdiffusion or gettering, as 880 min is the time which copper requires to diffuse a distance on the order of several hundred microns.

The exact nature of defect reactions observed in our experiments remains uncertain. It is possible that copper is trapped either by extended defects associated with oxide precipitates, such as punched-out dislocations, or by microscopic lattice defects, such as voids. Fig. 18 indicates that the passivating effect of copper may vary in a wide range, depending on the thermal history of a wafer, and, presumably, on the type of lattice defects in the wafer. Additional research is required to determine the exact nature of defect reactions involved in the passivation effect of copper. However, it is clear that the similarity between hydrogen and copper passivation can be beneficially used to gain a better understanding of the defect reactions of both hydrogen and copper in silicon.

3.7 Studies of kinetics of precipitation of interstitial copper at oxygen precipitates

Although it is well known that some types of extended defects such as stacking faults, Frank-type partial dislocations, and grain boundaries, serve as effective precipitation sites for copper (see, e.g., [54, 82-84]), a quantitative description of the efficiency of various precipitation sites, and oxygen precipitates in particular, was lacking. Since photovoltaic grade multicrystalline silicon contains high concentration of the dissolved oxygen and oxygen precipitates, it is quite likely that dissolved copper will precipitate at these oxygen clusters, thus creating recombination-active centers in the bulk of the wafer. This will decrease the solar cell efficiency.

In our experiments we used CZ silicon with the density of oxygen precipitates varying from 10^6 to 10^{11} cm^{-3}. The wafers were pre-characterized, i.e., the decrease of interstitial oxygen concentration after the precipitation anneal, ΔO_i, and the bulk microdefect density, N_{oxy}, were known. Additionally, the same experiment was performed using EFG multicrystalline material.

Using the new value for the diffusion coefficient of copper in silicon obtained in Sec. 3.1 above, one can apply Ham's law (see Refs. [85] for details) to predict the precipitation rate of copper:

$$\tau = \left(4\pi D_{eff} n r_0\right)^{-1} \qquad (15)$$

Assuming that the whole surface of oxygen precipitates serves as a precipitation site (this is the standard assumption in Ham's precipitation theory), the following precipitation time constants of copper were calculated:

Table 1.

Sample	ΔO_i ($\times 10^{17}$ cm^{-3})	N_{oxy} (precip/cm^3)	radius ($\times 10^{-6}$ cm)	Expected τ (s)
Si6	<0.1 (below detection limit)	1.8×10^6	unknown	>10,000
Si7	<0.1 (below detection limit)	2.0×10^7	unknown	>4000
Si8	0.28	2.3×10^8	8.38	930
Si9	0.54	1.6×10^9	5.46	205
Si10	2.25	1.5×10^{10}	4.15	28.8
Si11	6.00	2.5×10^{11}	2.25	3.2

Thus, one can expect that Cu would precipitate in the CZ samples with the density of oxygen precipitates from 10^8 to 10^{11} cm^{-3} with the time constants from 930 s to 3.2 s, respectively, and be very slow in the samples Si6 and Si7. In the latter two samples the expected time constants could not be calculated accurately since ΔO_i was below the sensitivity limit of FTIR system used to pre-characterize the wafers. By extrapolating the dependence of the expected precipitation time constants versus the density of oxygen precipitates to the density of oxide precipitates in the samples Si7 and Si8, the precipitation time constant τ were estimated as greater than 4000 s for the Si7 sample, and more than 10,000 s of the Si6 sample. Since it takes at least 30 min to chemically clean the samples after the quench and to evaporate Schottky diodes required for TID measurements, one can predict

that the initial Cu_i concentration, present in the sample at the moment of quench, will decrease by the beginning of measurement by the factor:

Table 2.

Sample	τ (s)	30 min / τ	Cu concentration decay factor after 30 min at room temperature
Si8	930	1.93	6.9
Si9	205	8.78	6.5×10^3
Si10	28.8	62.5	1.4×10^{27}
Si11	3.2	562.5	Complete Cu precipitation

Consequently, if oxygen precipitates are effective precipitation sites for Cu, then one may expect that Cu_i concentration in the Si8 sample will decrease as compared to the equilibrium *Cu* solubility at the diffusion temperature by a factor of 7, while in the Si9 sample it will decrease by more than three orders of magnitude and will be close to the detection limits of TID. Finally, Cu can be expected to precipitate completely in the samples Si10 and Si11. In the samples Si6 and Si7 with very slow precipitation rates the interstitial copper concentration should change by less than a factor of 2. This anticipated variation of the precipitation rate by several orders of magnitude as the density of oxygen precipitates changed from 10^8 to 10^{11} cm^{-3} was confirmed by our earlier study of precipitation of iron in silicon [86].

However, experimental measurements showed that precipitation of copper at oxygen precipitates is not described by Ham's law. Namely, the precipitation rate of copper, measured by TID was much slower than expected from Ham's law, thus indicating that oxygen precipitates are poor gettering sites. The decay of the interstitial Cu_i concentration (decay factor) during the 30 min required to manufacture Schottky-diodes, which was predicted from Ham's law to be 6.9 for the sample Si8, was as low as a factor of 2 (see Fig. 21). For the sample Si9, the decay of copper concentration was less than one order of magnitude, although the concentration decay expected from Ham's law was about a factor of 6×10^3 (see the table above). Furthermore, in the samples Si10 and Si11, in which we expected the indiffused copper to precipitate completely within the first 30 min, the decay of the Cu_i^+ concentration was only given by a factor of 20 to 40. Hence, there is no direct proportionality between the products of the density of oxygen precipitates and their radii, which is the product which determines the precipitation rate in

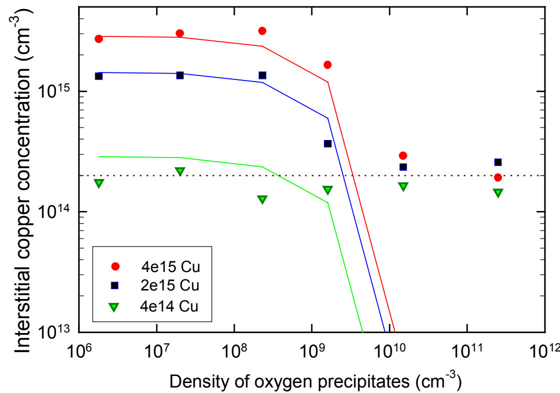

Fig. 21. Interstitial copper concentration detected by TID 30 min after the quench for different density of oxygen precipitates and different initial copper concentration. The initial copper concentration, determined by the annealing temperature, is indicated in the inset. Solid lines represent the best fit achieved using Ham's law obtained assuming that only 10% of the surface of oxygen precipitates getter copper.

Ham's law (Eq. (15)) and the experimentally observed copper precipitation rate. Additionally, the decay time of the remaining copper concentration was in agreement with the precipitation-free outdiffusion model, see Fig. 22. This implies that oxygen precipitates did not have any significant effect on the behavior of interstitial copper during measurements, although the decay of Cu_i concentration during the first 30 min after the quench, plotted in Fig. 21, indicates that some of the copper does precipitate at oxygen clusters immediately after the quench.

One could hypothesize that we observe the effect of saturation of oxygen precipitates with copper, whereby the oxygen precipitates become inefficient as soon as they getter a certain amount of copper. However, comparison of TID data obtained on samples with different initial copper concentration (Fig. 21) suggests that the effect is more complicated. Obviously, precipitation of copper at oxygen precipitates depends not only on the density of the precipitates, but also on the initial copper concentrations. For relatively high initial copper concentrations, 2×10^{15} cm^{-3} and 4×10^{15} cm^{-3}, the gettering effect becomes appreciable only in the samples with the density of oxygen precipitates exceeding 10^8 cm^{-3}. In contrast, if the initial copper concentration is lower, 4×10^{14} cm^{-3} (bottom curve in Fig. 21), then there is no dependence of the Cu_i concentration detected by TID on the density of oxygen precipitates whatsoever. An interesting feature of the Fig.21 is that the residual interstitial copper concentration, detected in the Si10 and Si11 samples at the beginning of the TID measurements, is almost independent of the starting copper concentration and is equal to about 2×10^{14} cm^{-3}. This suggests that similarly to bulk precipitation of copper in FZ silicon [12, 87, 88], there is a critical copper concentration which should be reached to trigger precipitation of copper at oxygen precipitates. As soon as interstitial copper concentration drops below this critical value, precipitation of copper at oxygen precipitates slows down or stops. Our data presented in Fig. 21 suggest that this critical concentration is about 2×10^{14} to 4×10^{14} cm^{-3} of copper in 10 Ω×cm silicon. Note that since interstitial copper is a shallow donor, an increase of the Cu_i^+ concentration in the sample results in electrical compensation of the sample and a gradual shift of the Fermi level upwards. The critical compensation level observed in this study corresponds to the Fermi level position between approximately E_V+0.3 eV and E_V+0.5 eV. This agrees with the theoretical predictions that the position of the energy levels of dislocations in silicon should be close to the mid-gap (see, e.g., Ref. [89]). Indeed, it is known that oxygen precipitates tend to punch out dislocations, and that dislocations are efficient precipitation sites for copper. Therefore, this result gives us reasons to believe that electrostatic effects are also involved in the precipitation of copper at extended defects associated with oxygen precipitates.

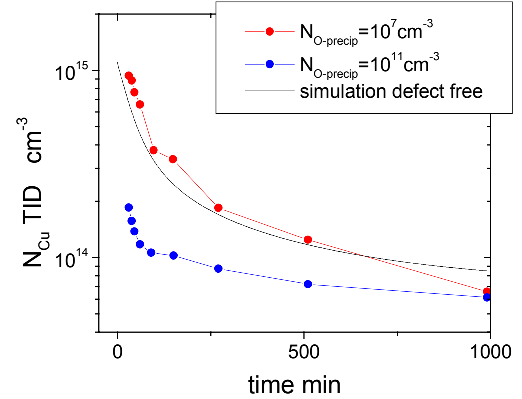

Fig. 22. Time dependence of the decay of interstitial copper concentration in CZ samples Si7 (density of oxygen precipitates 10^7 cm^{-3}, red (upper) curve) and Si11 (density of oxygen precipitates 10^{11} cm^{-3}, blue (bottom) curve), as measured by TID. Black line represents results of modeling of outdiffusion of copper to the wafer surface in the absence of bulk precipitation sites.

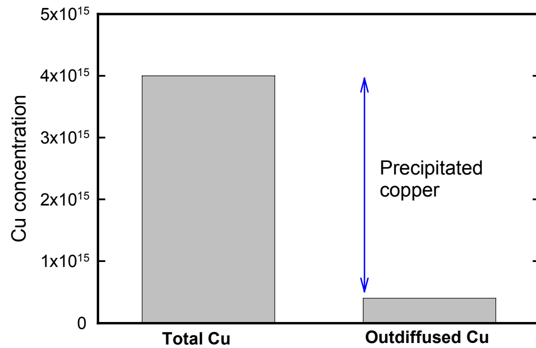

Fig. 23. Result of a TID measurement on EFG material. While most of copper has precipitated, non-negligible fraction of it remains in the bulk even 30 min after the quench. The residual copper concentration is similar to that observed in CZ samples.

Presently, we can suggest the following model: as long as the Fermi level in the sample lies above the energy level of dislocations punched out by the oxygen precipitates, these dislocations (which are thought to form acceptor levels in the band gap) are negatively charged and attract positively charged interstitial copper ions. As soon as the Fermi level drops below the energy level of these dislocations in the band gap, they change their sign from negative to neutral or positive, and copper precipitation slows down considerably. This hypothesis is similar to our model of Fermi-level dependent precipitation behavior of copper, discussed in Sec. 3.4.

An experiment similar to those described above and presented in Fig. 21 was performed using EFG multicrystalline material. As it follows from Fig. 23, 90% of the copper has precipitated in the bulk. However, the remaining 10 percent did not precipitate and could be detected as interstitial copper by TID 30 min after the quench. The kinetics of decay of the residual copper concentration, monitored by TID over the subsequent 24 hours, was in a good agreement with the model of outdiffusion of copper to the wafer surface without any precipitation in the bulk. This result is similar to that obtained on Si10 and Si11 CZ samples.

Thus, the following conclusions can be made. First, EFG silicon provides a very high density of precipitation sites for copper in the bulk of the wafer, comparable to the density of precipitation sites in CZ silicon with 10^{10} to 10^{11} cm^{-3} of oxygen precipitates in the bulk. However, these precipitation sites do not getter all the copper. In fact, almost 2×10^{14} cm^{-3} of copper remains ungettered 30 min after the quench, although the precipitation rate predicted by Ham's law for as high a density of defects as is available in the EFG material would be sufficient for all copper to precipitate within several minutes or less. This residual copper may diffuse to the p-n junction and form precipitates there, which may eventually decrease open-circuit voltage or even form shunts.

Our data, presented in this report, suggest that electrostatic effects, which we proposed to explain these observations, are as important in the EFG material as they are in CZ silicon with oxygen precipitates.

3.8 Study of the thermal stability of copper precipitates in silicon

In this study we used single crystal Czochralski-grown silicon, doped with 10^{15} boron atoms/cm^3, and containing 10^{18} oxygen atoms, as measured by FTIR. The wafers were subjected to a series of heat treatments to produce an oxygen precipitate density of 10^{11} cm^{-3}, and a stacking fault density of about 10^5 cm^{-3} (see [86] for details of the heat treatment; the pre-characterized CZ wafers were courtesy of R.Falster). Copper was intentionally introduced by dip coating the samples in a solution of copper fluoride trihydrate, HF, and H_2O followed by a 900^0C in-diffusion performed in a N_2 ambient. The annealing times used in these experiments were more than sufficient to establish the equilibrium concentration of 10^{18} Cu atoms/cm^3 throughout the thickness of the material. The samples were air-cooled with an average cooling rate of 25^0C/min. Excess copper was subsequently removed from the surface by mechanical polishing and chemical etching. The slow cool allowed for Cu precipitation at the internal defects and for outdiffusion of the rest of copper to the wafer surfaces. Anneals to dissolve the Cu precipitates were performed at 360 and 460^0C for 30 min and were also terminated by a rapid quench.

For copper detection, we utilized synchrotron-based XRF (Beamline 10.3.1 at the Advanced Light Source, Lawrence Berkeley National Laboratory) with which we ascertained the spatial distribution of copper in silicon. In this system, x-rays from a synchrotron source are focused to a spot size of 1-2 μm^2. The sensitivity of the μ-XRF system is such that one Cu precipitate with a 10 nm radius or greater can be detected within the sampling volume of 80 μm^3. The sample stage can be scanned, allowing mapping of large sampling areas.

Using the μ-XRF system, we have identified the positions of Cu precipitates with reference to an intentional scribe mark on two samples. The elemental map taken on the first sample after the Cu in-diffusion is shown in Fig. 24(a). The density of Cu clusters agrees well with the stacking fault density of 10^2/cm^3. Furthermore, the orientation of the Cu clusters is similar to the preferred orientation for stacking faults in silicon, where stacking faults prefer to lie on the (111) planes. Considering the total Cu concentration measured with XRF was 10^{16} per cm^2 of the scanned sample surface and the thickness of the silicon was 500 μm (giving a maximum concentration of 2×10^{17} cm^{-3}), we see a large fraction of the Cu has not precipitated at the internal defects but has likely returned to the surface during cooling.

We then annealed the sample at 360^0C for 30 min in an attempt to dissolve the Cu precipitates. After annealing, the sample was rescanned with the μ-XRF system in the same area using the scribe mark as a reference point. As shown in Fig. 24(b), we observe a decrease in the amount of Cu at the clusters. However, all precipitates remain, indicating that the 360^0C anneal was insufficient to fully dissolve the Cu precipitates.

For the second sample we attempted to dissolve the Cu precipitates using a higher temperature anneal at 460^0C. The μ-XRF maps of the sample in the initial state and after the 460^0C anneal are shown in Figs. 25(a) and 25(b), respectively. We observe more dissolution of the Cu precipitates with the 460^0C anneal as compared to the 360^0C anneal. Some clusters have dissolved to below the μ-XRF sensitivity limit while others have significantly decreased in size and intensity.

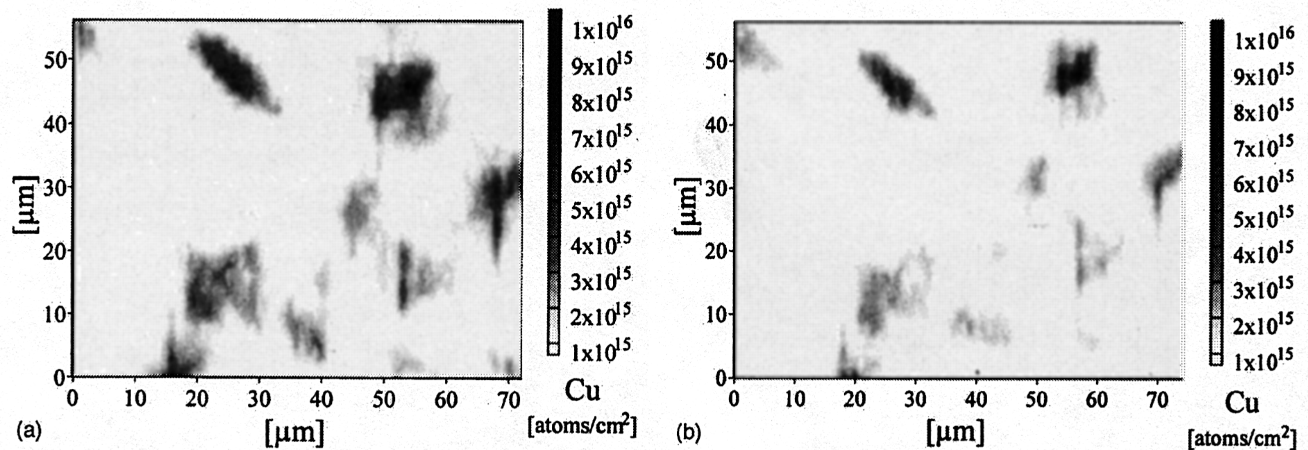

Fig. 24. (a) Precipitated Cu in CZ silicon with oxygen precipitates and stacking faults as measured with μ-XRF. Cu was intentionally introduced at 1180^0C and precipitated during a slow air cool. (b) Cu distribution in the sample from Fig. 1(a) after the sample has been annealed at 360^0C for 30 min. Note that some of the Cu clusters have decreased in size and intensity.

The rapid dissolution of Cu at low temperatures indicates that Cu precipitates formed at stacking faults are relatively unstable. However, the stability of the observed precipitates is higher than one could expect. Assuming Cu is in the form of Cu_3Si precipitates, theoretical calculations [90, 91] predict a Cu_3Si precipitate with radius smaller than 9 and 70 nm would fully dissolve during 30 min anneals at 360^0C and 460^0C, respectively. Considering that we do not observe full dissolution of all Cu clusters in this study, either some Cu precipitates may be larger than 70 nm, or some of the Cu precipitates are in a more stable form than Cu_3Si. Past TEM studies on precipitated Cu by Solberg et al. [92] and Seibt et al. [53] identified the formation of Cu_3Si when Cu was allowed to precipitate in silicon. However, these studies were performed on silicon material without previously formed oxygen precipitates. The presence of oxygen precipitates may allow for the formation of Cu oxides, which would dissolve slowly compared to metallic Cu and Cu silicides. From the point of view of equilibrium thermodynamics, Cu oxide formation seems unlikely since a comparison of heats of formation between SiO_2 and Cu oxides indicates SiO_2 is the thermodynamically favorable phase. However, thermodynamics does not preclude the formation of metal oxides and silicates, particularly in multicrystalline materials grown using rapid solidification techniques. For example, Fe oxides and silicate precipitates have been observed to form in the presence of SiO_2, even though SiO_2 is the thermodynamically favorable phase [15, 93]. This indicates Cu oxide or silicate formation can occur in the presence of SiO_2 via a preferred kinetic pathway.

Other TEM studies [94, 95] provide an alternative possibility to enhance Cu precipitate stability. These works identified the formation of CuSi rather than Cu_3Si for Cu precipitation in silicon and at the silicon surface. CuSi would be expected to have a slightly different dissolution rate than Cu_3Si, however, not as great of a difference as would be found for a Cu oxide compound. Hence, the conclusion of our study is that the moderate level of stability indicates that the Cu precipitates may be in a more stable form than Cu_3Si.

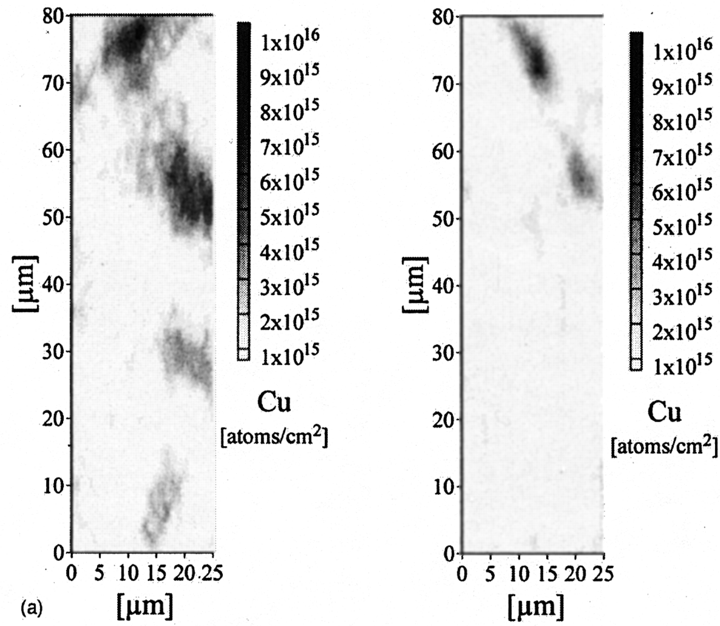

Fig. 25. (a) Precipitated Cu in CZ silicon with oxygen precipitates and stacking faults as measured with μ-XRF. Cu was intentionally introduced at 1180^{0}C and precipitated during a slow air cool. (b) Cu distribution in the sample from Fig. 2(a) after the sample has been annealed at 460^{0}C for 30 min. Note that some of the Cu clusters have been dissolved below the system sensitivity limit and others have decreased in size and intensity.

4 Iron in silicon

4.1 Analysis of the current understanding of iron in silicon

Iron is the best studied metal impurity in silicon, which was found in high concentrations at intragranular microdefects. Although the chemical state of iron at these defects was unclear, the attention of the photovoltaics community has been confined mostly to the interstitial iron, iron-boron pairs, and iron-silicide clusters. Since interstitial iron is a fast diffuser in silicon, and iron-boron pairs and iron-silicide easily dissociate, iron in the form of Fe_i, FeB, and $FeSi_2$ should be easy to remove from wafers by gettering. Therefore, it is unlikely that they form gettering-resistant clusters. To gain a better understanding of the other types of clusters/complexes formed by iron in silicon, and to identify iron compounds which can potentially be responsible for gettering-resistant clusters, we performed a detailed analysis of the literature on iron-related defects and their electrical properties. This study was published as two review articles, Refs. [6, 17], and was presented in our quarterly reports submitted to NREL in 1999-2000. Due to the large volume of the data presented in those reviews, in this section we will discuss the issues of hydrogen passivation of iron-related defects and interaction of iron with oxygen with the formation of iron oxides and silicates. We think that these issues can shed some light on the nature of gettering-resistant defects in silicon.

The first problem to be discussed in this section is the interaction of iron with hydrogen. The ability of hydrogen to passivate electrically active defects is well known (see, e.g., the review of Pearton *et al*. [96]) and is widely used in photovoltaics to increase the minority carrier diffusion length (see, e.g., Refs. [97, 98]). Passivation is usually implemented by a relatively low-temperature hydrogen plasma treatment. Substantial concentrations of hydrogen are also introduced into the near-surface region of silicon during routine chemical etching (see, e.g. [99-102]). Recent experimental data showed that the interaction of hydrogen with metal impurities is more complicated than just passivation. Complexes of transition metals with hydrogen often introduce new levels in the bandgap (see, e.g., recently published data on *Pt-H* complexes [101], *Ag-H* complexes [103], and *Co-H* complexes [104]).

Despite the importance of the problem of interaction of iron with hydrogen and passivation of iron-related defects, literature data are inconclusive. Tavendale and Pearton [105, 106] studied the influence of hydrogen plasma treatment on *Fe*-related deep levels and reported that the levels at $E_V+0.32\ eV$ and $E_V+0.39\ eV$ (note that the latter level is not the level of Fe_i), which appeared in DLTS spectra after iron diffusion, were neutralized by hydrogen to the depth of the hydrogen penetration. They also found that the level of interstitial iron was not affected by the plasma treatment. The latter result has recently been confirmed by Weber [107]. Data of Kouketsu *et al*. [108, 109] indicate that the *FeB* peak at E_V+0.1 eV is effectively neutralized by hydrogen. Yakimov *et al*. [110] suggested that the introduction of hydrogen during wet chemical etching stimulates the dissociation of *FeB* pairs in the near-surface layer and increases the local concentration of unpaired interstitial iron. However, the mechanism of such a dissociation process remains unclear. Kaniewska *et al*. [111] reported a change in the shape of the DLTS spectra taken on *n*-type *Fe*-contaminated silicon samples with dislocations and stacking faults after hydrogenation. However, the complex nature of the spectra made it impossible to identify the passivated centers.

Several authors suggested that the levels at E_V+0.23 eV, E_V+0.38 eV [108, 109], and E_V+0.31 eV [112] appear in the bandgap after hydrogenation of iron-contaminated samples and argued that they are levels of iron-hydrogen complexes. It was shown that these levels are unstable at elevated

temperatures and dissociate after anneals at 175^0C for 30 min [112]. Unfortunately, the experiments described in Refs. [108, 109, 112] lacked a systematic analysis of the interaction of hydrogen with the impurity levels, such as the one developed in Refs. [99, 103]. This approach includes the comparison of DLTS spectra of cleaved (no hydrogen) and etched (hydrogen in the near-surface region) samples and a comparison of the depth profiles of the traps with the predicted distribution of hydrogen. This correlation even enables one to determine the number of hydrogen atoms in a complex. To the best of our knowledge, this technique has not yet been applied to iron in silicon. It is clear, however, that hydrogen passivation can be inefficient for some complexes of iron.

The second aspect of properties of iron in silicon important for solar cell efficiency, which will be discussed in detail in this section, is precipitation of iron and formation of iron silicide and iron silicates in the bulk of the wafer. Similarly to other transition metals, iron forms a number of silicide phases, including cubic ε-FeSi, tetragonal α-$FeSi_2$, orthorhombic β-$FeSi_2$, hexagonal Fe_5Si_3, and cubic Fe_3Si [113, 114]. A phase diagram of iron-silicides can be found in [115]. Note that it is usually much more difficult to find iron-silicide precipitates in the bulk of a silicon wafer after thermal diffusion and cool down than to find precipitates of copper or nickel. This is because the solubility of iron is much lower than that of Cu or Ni. Low strain fields around the precipitates make their TEM observation difficult. Additionally, the pairing of iron with boron is an efficient trapping mechanism, which significantly reduces the driving force for the precipitation of iron in the bulk. Several groups [30, 116-118] succeeded in finding rod-like $FeSi_2$ precipitates, up to 0.5 μm long and a few tenths of a nanometer thick, in TEM samples prepared from devices or wafers after thermal indiffusion of iron. These iron-silicide precipitates were observed at Si/SiO_2 interfaces. However, most observations of iron-silicide precipitates were done after implantation of high doses of iron with subsequent annealing [119-129]. These studies were stimulated by the prospect of using iron-silicide or silicon-based optoelectronics (see, e.g., [130-132]) since its direct band gap of about 0.87 eV makes it suitable for the fabrication of infrared detectors or emitters integrated to silicon circuits.

In contrast to bulk precipitates of iron in high crystalline quality silicon, agglomeration of iron at extended defects, such as dislocations or low-angle boundaries, can easily be observed after thermal diffusion of iron. A significant increase in the recombination activity of iron-contaminated dislocations, silicon-oxide precipitates, and misfit dislocations in Si/SiGe epitaxial structures has been reported in Refs. [133-139]. However, the formation of distinctive large iron-silicide precipitates at extended defects is very uncommon. With a few exceptions (such as [140]), it was found that iron precipitates along dislocation lines very uniformly, and does not form any contrast spots in EBIC images, common for *Cu*-contaminated samples [84, 117].

Decoration of dislocations and oxidation-induced stacking faults (OSF) with iron is a well-known cause for *pn*-junction leakage, breakdown of oxides, and retention time (refresh) failures of DRAMs [141-144]. Interestingly, iron not only decorates the existing stacking faults, but also affects their growth. As discussed in the April 99 quarterly report and in our article, Ref. [6], the data on the effect of iron on nucleation of silicon-oxide precipitates are contradictory. However, everyone agrees that iron enhances the final stage of growth of silicon-oxide precipitates, i.e., the formation of OSFs [113, 141, 145-149]. Fujino et al. [147] showed that the density of OSFs increased by nearly 5 orders of magnitude as iron surface contamination level increased from 3×10^{11} cm^{-3} to 10^{13} cm^{-3}. Likewise, Miyazaki et al. [145] observed higher OSF densities for iron concentrations above $5x10^{12}$ Fe/cm^3.

The increase of the precipitation rate of iron in polycrystalline silicon, proportional to the density of dislocations, grain boundaries, and intragranular defects, was observed by Bailey et al. [22], and clearly indicated that iron precipitates at these defects. A similar correlation of precipitation rate of iron with the density of silicon-oxide precipitates has been done by Gilles et al. [150, 151].

Experimental studies of Aoki et al. [152-154] showed that the presence of silicon-oxide precipitates does not affect the solubility of iron in the bulk, but changes the kinetics of its precipitation [154]. Aoki et al. [154] performed TEM-EDX (transmission electron microscopy combined with energy-dispersive X-ray analysis) measurements and were able to directly detect iron at silicon-oxide precipitates. Our group [86, 155] (see Sect. 3.3 below) developed a quantitative technique for analysis of iron precipitation kinetics. Application of this technique to CZ silicon with different densities of silicon-oxide precipitates confirmed that the effective density of precipitation sites for iron correlates well with the density of silicon-oxide precipitates. We concluded from our studies that iron is gettered by the surface of silicon-oxide precipitates rather than by associated dislocations. In contrast, Sadamitsu et al. [156], and Ogushi et al. [157] argued that iron is most probably gettered by the bulk of the precipitates.

Besides precipitation of iron at extended defects in the bulk, accumulation of iron at the Si/SiO_2 interfaces or at the bare silicon surface has also been observed [113, 127, 158-164]. The precipitation of iron near the growing Si/SiO_2 interface may be stimulated by silicon self-interstitials, injected by the growing oxide and consumed by the iron-silicide precipitates, or by local compressive strain fields at the Si/SiO_2 interface [161, 162]. This is because the molecular volume of iron silicide is less than that of silicon, and the precipitates are surrounded by a tensile strain.

The thermal stability of precipitated iron was studied by Ramappa et al. [165], Colas et al. [166], and Aoki et al. [167] in FZ silicon, and by Aoki et al. [167, 168] in CZ wafers with silicon-oxide precipitates. All of these studies showed that iron is weakly bound at iron-silicide precipitates, and can be dissolved back into the silicon by annealing the samples. Detailed studies of McHugo et al. [169] indicated that the stability of iron at oxygen precipitates somewhat depends on the carbon content of the sample. It was found that iron is more stable at oxygen precipitates formed in silicon with low carbon content. It was suggested that carbon reduces the strain, which stabilizes the iron at oxygen precipitates [169].

It is important to note that the relatively low thermal stability mentioned above refers only to iron (or possibly iron silicide), precipitated at already existing extended defects. As we will show below, the presence of iron in the wafer surface *during* silicon dioxide growth may lead to the formation of strong chemical bonds between iron, oxygen, and silicon, with the formation of iron oxides or iron silicides. A similar effect may also take place during rapid solidification of silicon melt, used in PV technology. Since mc-Si for PV applications contains high concentration of oxygen, unintentional contamination of melt with transition metals may result in formation of iron-oxygen complexes. The starting concentration of iron in polysilicon feedstock steadily decreases with the development of silicon purification technology. Relatively recent studies of Huber et al. [21] revealed that the iron concentration in polysilicon is below 2.5×10^{11} cm^{-3}. In single crystal growth technologies (FZ and CZ), only a small fraction of this amount of iron is transferred to the growing crystal due to the effect of segregation of impurities in the melt. Literature data on segregation coefficient of iron between the silicon solid crystal and the melt are in reasonably good agreement: 10^{-4}, as reported by James et al. [170], 8×10^{-6} as reported by Trumbore [171], 3×10^{-5} as reported by Bugay *et al*. [172], 4.6×10^{-6} as reported by Mishra et al. [173], 5×10^{-6} to 1×10^{-5} as follows from the experiments of Collins [174], and 7×10^{-6} as derived by Weber [31, 175]. Thus, the average value of distribution coefficient is about 10^{-5}. Unfortunately, the photovoltaics manufacturing uses simplified low-cost technologies to grow multicrystalline silicon at high pulling rates. These technologies cannot benefit from the segregation effects of transition metals in the melt to the same extent as monocrystalline technology does. Hence, it is reasonable to expect that mc-Si can contain iron in concentrations from 10^{11} to 10^{13} cm^{-3}, as follows from the data from Refs. [20, 21].

A number of authors have discussed the possibility of forming other phases of iron which are thermodynamically more favorable than either α- or β-$FeSi_2$ [176-178]. Hackl et al. [178] presented a table of formation energies for possible iron-oxygen-silicon compounds to show that the highest formation energy is for a silicate of Fe_2SiO_4 followed by Fe_3O_4, while $FeSi_2$ has a lower energy of formation by a factor of 18.

Probably the first experimental observation of the effect of strong binding of iron in the surface silicon-dioxide was made in the studies of the solubility of iron in silicon [163, 179-181]. It was found that if there is no oxide on the surface, and the annealing ambient does not contain traces of oxygen to form such an oxide during the anneal, then all iron deposited on the surface easily diffuses into the bulk. If the wafer surface is covered by silicon dioxide, and particularly if trace concentrations of oxygen or residual water vapors [182] are present in the annealing ambient, iron becomes bound to oxygen contained in the surface oxide [147]. Rotondaro et al. [183] reported that in dry O_2, only about 50% of the surface Fe contamination was found in the bulk after diffusion, while the use of N_2 results in a diffusion of 70 to 100% of the contamination into the bulk. Recent Auger electron spectroscopy (AES) and X-ray photoelectron spectroscopy (XPS) studies by Swart et al. [184] confirmed that iron in the oxide indeed forms chemical bonds to silicon and oxygen.

Note that the equilibrium bulk iron concentration after diffusion in oxidizing ambient may be affected not only by the fraction of iron bound at the surface, but also by the fact that a new boundary phase different from iron silicide $FeSi_2$ is formed. A phase with a larger formation energy results in a lower equilibrium solubility of iron in silicon. Colas et al. [166] studied the solution of iron in the presence of oxygen clusters of different morphology and speculated that they might have observed the formation of an oxygen-iron compound which is more stable that the $FeSi_2$ silicide. However, the possibility of formation of iron oxides or silicates in the silicon lattice was not fully explored until highly-sensitive synchrotron-radiation-based X-ray techniques, which can unambiguously distinguish different types of bonding, became available. Kitano [93] diffused iron into boron-doped CZ silicon wafers through a 20 nm SiO_2 film at 750^0C and 900^0C, removed oxide by HF chemical etching, and studied the chemical state of iron at the silicon surface (former Si/SiO_2 interface) by using the angular-dependent total X-ray fluorescence and X-ray absorption fine structure techniques. It was found [93] that a significant amount of iron was concentrated at the SiO_2/Si interface and that chemical bonds of the type Fe-O, Fe-Si and Fe-Fe were formed. The valence of iron was a mixture of Fe^{3+} and Fe^{2+}, but mostly Fe^{3+}. From these observations, Kitano [93] inferred that the layer formed by iron at the SiO_2/Si interface is iron silicate, in which a portion of Fe^{3+} ions are reduced to Fe^{2+}, similarly to the natural iron silicate $Fe^{3+}Fe^{2+}_{0.5}[SiO_4]$, known as laihunite. Clearly, similar behavior of iron may also be expected if iron and oxygen co-precipitate in the bulk of the wafer. Sadamitsu et al. [113] reported that their TEM analyses revealed inclusions in silicon oxide when they intentionally contaminated silicon with iron and oxidized it. They suggested that the inclusions may be either Fe_3O_4 or Fe_2SiO_4 [113]. The formation of the iron oxide embedded into the chemical oxide on the wafer surface was suggested by Takizawa et al. [185]. Shimizu [186-189] argued that thermal oxidation of Fe- and Al-contaminated wafers leads to the incorporation of these metals into a growing oxide in the form of $(FeOSi)^-$ negative ions, which are oxidized, during the oxide growth, into neutral metal oxides. In agreement with the observations of Refs. [147, 190-192], they found that metals were located primarily at the oxide surface, furthest from the Si/SiO_2 interface. A similar observation was made by Tardif et al. [193, 194], Hocket et al. [195], and Zhong et al. [196]. Takiyama et al. [197] investigated a possibility of chemical reactions of iron with SiO_2 by mixing powders of iron-oxide with silicon-dioxide, sintering them in a nitrogen ambient, and analyzing them by X-ray

diffraction. They observed formation of iron-silicates, tentatively Fe_2SiO_4, after sintering at temperatures of 900^0C and above.

Since there are strong indications in the literature that dissolution-resistant iron-oxides and silicates can be formed in silicon, a series of analyses was performed with the purpose of assessing the feasibility of finding such complexes of iron in solar cells. These data are presented in Sec. 6.

4.2 Method of evaluation of precipitation sites density from the analysis of iron precipitation kinetics.

So far, there was no reliable experimental technique to determine the density of heterogeneous precipitation sites in the bulk of silicon wafers. Such techniques as chemical etching, laser scattering tomography (LST), Optical Precipitate Profiler (OPP), and Fourier transform infra-red spectroscopy (FTIR) can be used to detect only large precipitates, containing more than 10^6 impurity atoms, and are not sensitive to microdefects. We developed an experimental technique which enabled us to determine the precipitation site density from the analysis of precipitation kinetics. The technique is based on theoretical analysis of Ham [85]. Taking into account the growth of the precipitates and the increase of their radii during growth, Ham solved the three dimensional diffusion equation and obtained the following analytical equation to describe the kinetics of precipitation:

$$Dt\cdot\left(\frac{4\pi n}{3}\right)^{2/3}\cdot\left(\frac{(c_o-c_s)(1+Z)}{c_p-c_s}\right)^{1/3}=$$
$$\frac{1}{6}\ln\left(\frac{\left(u(t)^2+u(t)+1\right)\left(u(0)^2-2u(0)+1\right)}{\left(u(t)^2-2u(t)+1\right)\left(u(0)^2+u(0)+1\right)}\right)+$$
$$-\frac{1}{\sqrt{3}}\tan^{-1}\left(\frac{2u(t)+1}{\sqrt{3}}\right)+\frac{1}{\sqrt{3}}\tan^{-1}\left(\frac{2u(0)+1}{\sqrt{3}}\right) \tag{16}$$

where

$$u(t)^3=1-\frac{\bar{c}(t)-c_s}{(\bar{c}(0)-c_s)(1+Z)} \quad \text{and} \quad Z=\frac{4\pi n r_o^3}{3}\cdot\frac{c_p-c_s}{c_o-c_s} \tag{17}$$

and where $\bar{c}(t)$ is the time dependent solute (impurity) concentration, c_o is the initial impurity concentration, c_s is the impurity equilibrium solubility concentration, c_p is the density of the impurity in the precipitate, D is the diffusivity of precipitating impurity at the fixed precipitation temperature, n is the precipitate site density, and r_o is the *initial* precipitate radius. Eqs. 16 and 17 can be used to fit given experimental data by varying n as long as the precipitation took place at a constant temperature. However, because of the implicit nature of this formulation, Eqs. 16 and 17 would have to be solved using convergent techniques for each time increment. This would require long computer times to complete.

To simplify the problem, Ham assumed a fixed precipitate radius r_o. For a precipitate of fixed radius, Ham finds that the precipitation process is adequately described by,

$$\bar{c}(t)-c_s\cong(c_o-c_s)\cdot e^{-t/\tau_o} \tag{18}$$

with

$$\tau_o=1/4\pi n r_o D \tag{19}$$

Ham also showed that the growing radius solution approximates the fixed radius solution if the precipitate radius does not change significantly during growth, i.e. when more than 50% of the solute has precipitated:

$$\frac{\overline{c}(t)-c_s}{c_o-c_s} \cong k \cdot e^{-t/\tau_o} \qquad (20)$$

where k is a constant which is larger than 1 and depends on the ratio of n/c_o, and τ_o is given in Eq. 19. To the best of our knowledge, only few experimental studies, published to-date, analyzed the precipitation kinetics of impurities, and all of them used the exponential approximation. For example, Gilles *et al*. [151] and Livingston *et al*. [198] applied Ham's law to the gettering effect of oxygen precipitates. Bailey *et al*. [22] precipitated iron in different types of PV silicon and found a correlation between the initial diffusion length in as-grown samples and the precipitation rate of iron. However, since they used an exponential approximation, they could not give a quantitative estimate for the density of precipitation sites. The disadvantages of applying the exponential approximation method are as follows:

- Fitting this equation to experimental data points yields only the product nr_o, and does not allow one to determine n and r_0 separately.
- Early in the precipitation process the precipitate radius is growing, giving rise to a non-exponential curvature. Unfortunately, most experimental techniques are most accurate while the solute concentration is still large, i.e. early in the precipitation process.
- The product nr_o does not indicate whether the early precipitation was non-exponential (small r_o and large n) or exponential (large r_o and small n).

To address the first point, some studies [150, 199] have used the conservation of mass to obtain n as follows. The conservation of mass is simply expressed as,

$$\Delta c = \frac{4}{3}\pi r_o^3 n c_p \qquad (21)$$

Combining Eq. 19 and 21, one obtains an expression for n as,

$$n = \left(\frac{3}{4}\pi \cdot \frac{1}{(4\pi D \tau)^3} \cdot \frac{c_p}{\Delta c} \right)^{1/2} \qquad (22)$$

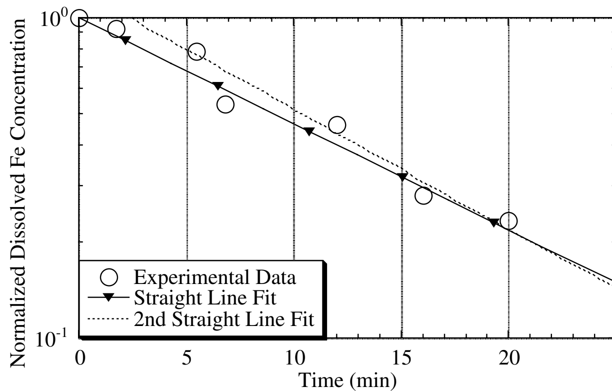

Fig. 26: Iron precipitation in Cz silicon at 650°C. The straight line fit is equivalent to the fixed radius approximation and yields a precipitate site density (with Eq. 7) of $3.9\text{x}10^8$ sites/cm^3. The second straight line fit through the last three data points yields a site density of $4.7\text{x}10^8$ sites/cm^3.

where Δc is the drop of solute concentration, and c_p is the density of the impurity in the precipitate. This already enables one to get an estimate of the precipitate density.

To demonstrate the application of Eqs.21,22, combined with the exponential approximation, experimental precipitation data of iron in silicon are plotted in Fig.26. The data were obtained from Czochralski silicon samples with no oxygen precipitates which were first contaminated to an interstitial iron concentration of approximately $4.75\text{x}10^{13}$ Fe/cm^3 as measured by deep level transient spectroscopy (DLTS). They were then annealed for various times at 650°C

followed by a quench. The remaining interstitial iron concentrations were then measured with DLTS. Assuming precipitation follows Ham's law (Eq. 18 and 19), the time constant τ can be obtained from the slope of a straight line fit through experimental data points as illustrated in Fig.26. The resulting nr_o product found from the slope in Fig.26 is 402 cm^{-2}. Using Eq. 22, one finds that n=3.9x10^8 sites/cm^3 using a c_p=25.6 Fe/nm^3. While this is close to the value obtained by more rigorous methods (see below), n=7.2x10^8 sites/cm^3, the error incurred is sensitive to where the data points are measured. Lines fitted to data taken early in the precipitation induce greater error than a linear fit through data taken later in the precipitation. For example, the last three data points were fitted with a second straight line and Eq. 22 was used to obtain n=4.7x10^8 sites/cm^3. Clearly, the site density estimate is improved as lines are fitted to data points later in the precipitation process. Here the 'fixed radius' r_o is approximately the radius of the final precipitate.

The accuracy of the evaluation of precipitate sites density can be further improved using an iterative technique based on the fixed radius solution, which provides a number of advantages. First, this method can simulate the growing radius solution by appropriately increasing the radius after each small time interval, Δt. Furthermore, this approach can be used in conjunction with other finite-difference simulations that require an explicit expression of the change in dissolved concentration as a function of time. Finally, the precipitation can still be modeled *when the temperature is not fixed*, as during a slow cool.

For the iterative solution of Ham's equation, we have slightly modified Eq. 18 to obtain:

$$\Delta\bar{c}(\Delta t) = \bar{c}_{t+\Delta t} - \bar{c}_t = [c_s - \bar{c}_t]\times\left(1 - e^{-\Delta t/\tau}\right) \quad \text{with} \quad \tau = 1/4\pi n\, rD \qquad (23)$$

In this equation Δc is the change of the solute concentration from the starting concentration of the time interval Δt. It is slightly different from Eq. 17 because that equation yields the absolute concentration with respect to the equilibrium solubility concentration.

To calculate changes in precipitate radius, we used the following equation,

$$\Delta c = \frac{4}{3}\pi\left(r_1^3 - r_0^3\right)\times nc_p \qquad (24)$$

where r_0 and r_1 are, respectively, the precipitate radii before and after the time interval Δt.

The results of the iterative calculations are shown in Fig.29 using the same experimental data as in Fig.28. Both the analytic growing radius solution, Eqs. 16 and 17, and the iterative solution fit each other and the data well for n=7.2x10^8 sites/cm^3. Solutions for n=5x10^8 and 9x10^8 sites/cm^3 are also shown to illustrate the sensitivity of the solution on n. The superiority of the fit in Fig.27 compared to that in Fig.28 is obvious. Thus, the developed iterative algorithm can be used to fit experimentally measured precipitation kinetics and enables us to determine not only the product nr_0, as it was the case in the previously reported studies, but the density of precipitation sites n and the average radius of precipitation sites r_0 separately. The developed algorithm is much faster than the direct solution of Eq.16, and the obtained density of precipitation sites is accurate since the data points in the beginning of the decay are used.

Experimental data presented in Fig.27 show the superiority of the iterative technique over the methods based on exponential approximation. To obtain an additional proof of accuracy of data obtained from the analysis of iron precipitation kinetics, we applied the technique to precipitation of iron at well characterized oxygen precipitates in CZ silicon. As a matter of fact, this work was the first consequent quantitative study of precipitation of iron at oxygen precipitates. Previous studies succeeded only in establishing an unambiguous correlation between the density and size of oxygen precipitates and the kinetics of internal gettering of iron. For example, Gilles *et al*. [150, 151]

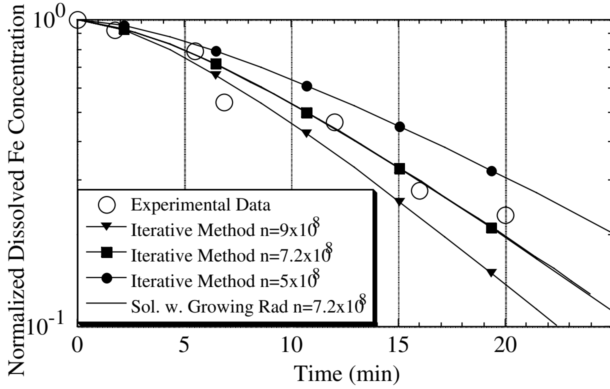

Fig. 27: More accurate methods used to evaluate experimental precipitation data. The thick line is the exact analytic solution with a growing radius given by Ham using an iron precipitate density of 7.2×10^8 sites/cm^3. The iterative technique with the same site density yields essentially the same curve. Variations in *n* are also plotted.

measured the low temperature precipitation rate of iron and derived nr_0 products, where n is the density of precipitation sites with a radius of r_0. They showed a direct correlation between the nr_0 product of oxygen precipitates during the oxygen precipitates growth step and the nr_0 product of iron in the same samples at low temperature.

Czochralski silicon samples used in our experiment were cleaved from the center regions of four different wafers, all with an initial oxygen level of approximately 7×10^{17} <O_i>/cm^3 and a boron doping of 1.5×10^{15} B/cm^3. These wafers were first heat treated to dissolve all oxygen nuclei, and then subjected to different oxygen nucleation treatments and finally a single 1000°C, 16 hour growth step. The resulting drop in oxygen concentration and the oxygen precipitate density are listed in the Table 4.

Oxygen precipitate concentrations were obtained near the center of the cleaved wafers by preferential etching and then counting the pits. Samples for this experiment were taken near the center of un-etched wafers. These samples were cleaned, scratched with 99.997% pure iron and annealed at ≈900°C, contaminating the samples to (2 to 4)x10^{13} Fe/cm^3. The samples were cleaned again and annealed (precipitation anneal) in a horizontal furnace or in a rapid thermal anneal system followed by a quench to room temperature. After the precipitation anneal, more than 60 μm were etched from the surfaces, and aluminum diodes were evaporated for deep level transient spectroscopy (DLTS) measurements, which were used to determine the concentration of interstitial iron remaining in the solute.

Table 4: Experimental data and calculated radius for various silicon samples used in this study.

Sample	ΔO_i ($\times 10^{17}$ O/cm^3)	n_{oxy} (precip/cm^3)	Radius ($\times 10^{-6}$ cm)
Si8	0.28	2.3×10^8	8.38
Si9	0.54	1.6×10^9	5.46
Si10	2.25	1.5×10^{10}	4.15
Si11	6.00	2.5×10^{11}	2.25

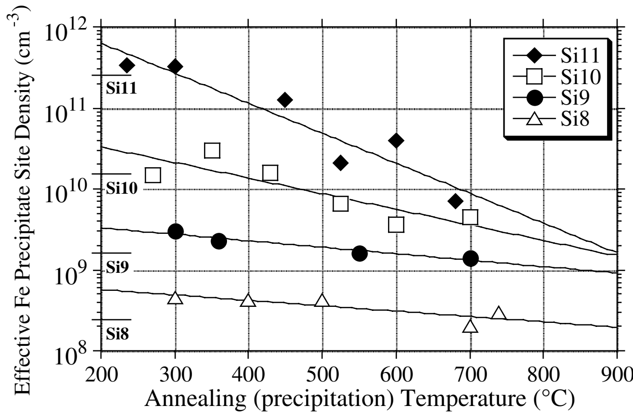

Fig. 28: Effective iron precipitate density plotted for various temperatures using the radius of the oxygen precipitates for r_o. The horizontal bars on the y-axis indicate the oxygen precipitate density for the materials specified.

Ham's equation was fitted to the experimental data points. The decay of interstitial iron in the experiment was exponential, indicating that the radius was large and not growing. Such an exponential decay could be explained if iron were precipitating on or decorating a larger defect such as the oxygen precipitate itself. In this case, if the radius of the oxygen precipitate were used for r_o, then the iron precipitate site (here and below, the term "nucleation site" will be used for all sites with an initial radius of the smallest nucleus, i.e. a pair of atoms, which results in a non-exponential decay. The term "precipitation site" will refer to sites with a larger initial radius resulting in an exponential decay) density, n_{Fe}, should match that of the oxygen precipitate density, n_{Oxy}. Assuming the oxygen precipitates are essentially spherical, the radius of the oxygen precipitates was estimated from the number of precipitates and the total oxygen concentration precipitated. Using this calculated radius of the oxygen precipitates for r_o, the resulting iron precipitate densities, n_{Fe}, for various annealing (precipitation) temperatures are shown in Fig.28. One can see that for low temperatures, $n_{Fe} \approx n_{Oxy}$, proving the model that iron precipitates on or decorates the surface of the oxygen precipitates.

Additionally, for the samples Si8 and Si9, the low temperature n_{Fe} is even slightly above the n_{Oxy} as might be expected for an oxygen precipitate with a shape that has a larger surface area than a simple sphere. From Fujimori's [200] study of oxygen precipitate morphology, we can expect that the oxygen precipitates in the Si11 sample have octahedral and truncated octahedral morphologies (essentially spherical), while the oxygen precipitates in the Si8 sample have truncated octahedral and platelet morphologies. The platelet morphology provides a larger surface area for the iron to precipitate on or decorate, resulting in a slightly larger n_{Fe} than n_{Oxy}.

In Fig.28, one can also see that the low temperature data can not be used at high temperatures, since there is dependence of the iron precipitation rate on annealing temperature. Therefore a better quantitative method for describing precipitation is to specify r_o, thus determining the form of the decay, and then to specify n for various temperatures. The simplest explanation for the temperature dependence of n_{Fe}, is that at lower supersaturation (high temperature), not all of the oxygen precipitates act as sinks for iron. This implies that some of the oxygen precipitates are more favorable sites for iron precipitation. That the temperature effect is strongest for the Si11 samples which contain the smallest oxygen precipitates may indicate that there is a size or a strain [169] effect. It seems more likely, however, that some sites on the oxygen precipitate itself are more favorable for iron precipitation. Thus at low supersaturation (high temperatures) only a portion of the oxygen precipitate surface serves as an iron precipitation site, reducing the effective number of sites. At high supersaturation (low temperatures), the whole oxygen precipitate behaves as a precipitate site, increasing the effective n_{Fe}.

4.3 Studies of the processes of precipitation of iron, dissolution of iron precipitates, and effect of iron precipitation on minority carrier diffusion length

While the impact of interstitial iron on minority carrier diffusion length is well documented [47] and is used as the primary tool for non-contact determination of the dissolved iron content in silicon wafers, the impact of precipitated iron on minority carrier diffusion length is unclear. We performed a series of studies of the change in the diffusion length in various types of samples as iron precipitates. As shown in Fig. 29, for most samples, the minority carrier diffusion length did not improve and even degraded as the iron precipitated.

The next experiment was to observe dissolution from iron precipitated at oxygen precipitation sites. This process can be simulated using an iterative approach of Ham's law. The silicon sample contained $2x10^8$ oxygen precipitates/cm^3 and was contaminated with iron to approximately $3x10^{13}$ Fe/cm^3. The iron was allowed to precipitate during a slow furnace cool. The sample was then cleaned and annealed at 845°C. The dissolved iron concentration was monitored by DLTS as a function of time. A computer simulation was also performed using the above parameters. The results are shown in Fig. 30. As can be seen, the simulation follows the experimental results satisfactorily. The minority carrier diffusion length was already limited by the oxygen precipitates and did not correlate with the amount of dissolved iron.

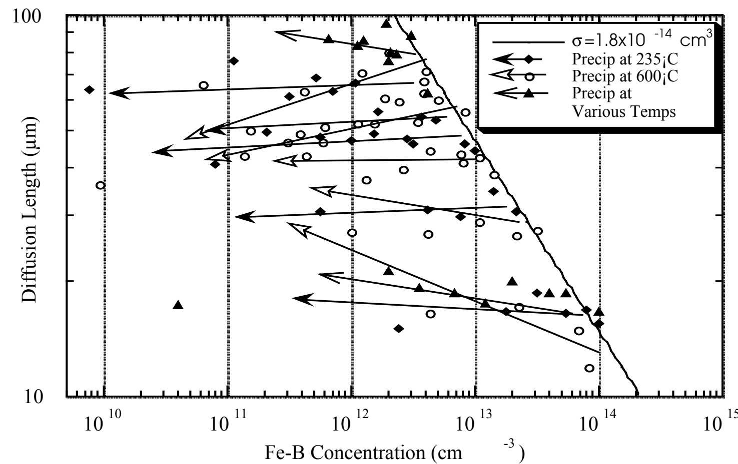

Fig. 29: Minority carrier diffusion lengths as iron precipitates in quenched samples. The straight line is the minority carrier diffusion length for FeB as a function of FeB concentration. FeB concentrations measured by DLTS.

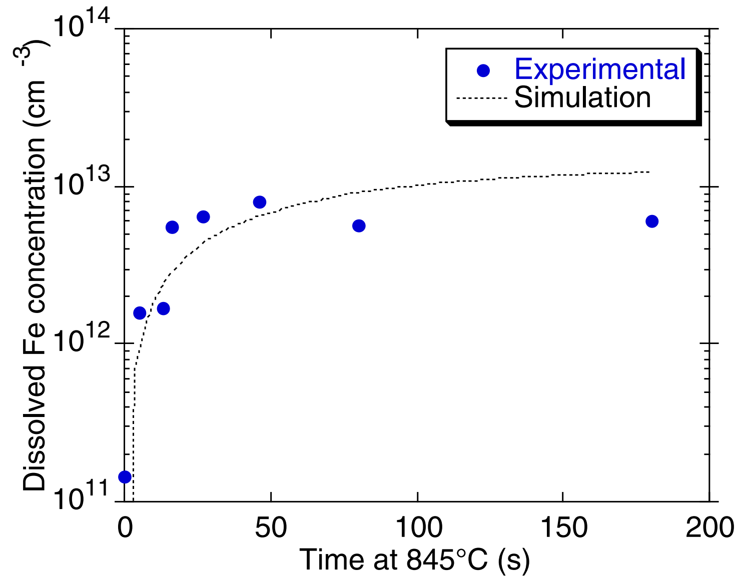

Fig. 30: Dissolution of iron which was previously precipitated at oxygen precipitates.

The results presented above suggest that anneals at 845^{0}C can dissociate iron precipitated at oxygen precipitates, which indicates that iron has precipitated in its metallic or silicide form and did not form silicates or oxides.

Part 2. Transition metals in PV-silicon

5 Application of synchrotron radiation-based X-ray fluorescence microprobe to detect impurities at the location of a shunt.

Shunts are one of major defects limiting solar cell efficiency. They are local spots of low open circuit voltage, which drain current from the areas with a higher open circuit voltage. This decreases the total output voltage of the cell and, consequently, their overall efficiency. Localization and identification of shunts in processed solar cells had remained a problem for a long time, until the technique of thermography was developed and applied to photovoltaics (see, e.g., [201-204]). This technique detects a local increase of temperature on the wafer (typically on the order of millikelvin or less) in the area where a current flows through the shunt. A temperature map of the wafer is obtained either by means of a thermocouple, pressed against the wafer and moved from one position to another by a step motor, or by a highly sensitive infrared videocamera, coupled with a lock-in amplifier and averaging electronics to achieve the best possible sensitivity.

According to the majority of authors, localized dislocations are not involved in the shunt formation. Some of the local shunts were found to be associated with accumulations of grain boundaries, while the others are defects of *pn*-junctions. The dominant shunts have often been found at the edges of the cells. The dependence of the shunt strength on elastic deformation of the cells, which is sometimes observed, indicates that mechanical stress may influence certain shunts. According to Breitenstein *et al*., the quantitative influence of shunts on the efficiency is shown to increase to above 30% for illuminations below 0.2 suns. For stronger illuminations the effect may be weaker, but certainly not less than several percent of the efficiency of the cell.

It was shown that shunts, localized by IR thermography, can also be observed as contrast spots in EBIC and LBIC maps. However, only few of recombination-active spots are shunts, and there is no simple way to tell from EBIC or LBIC measurements alone which of the contrasts is a shunt. Additionally, despite numerous efforts to identify the nature of the shunts, no consistent model is available yet. In this study, we applied the X-ray fluorescence microprobe technique to test whether metal impurities are involved in shunt formation. The study was performed in collaboration with our colleagues from the Instutute of Semiconductor Physics (Frankfurt-Oder, Germany), who provided us with RGS material pre-characterized with infra-red thermography and EBIC. The location of a shunt was described by its position relative to grain boundaries, visible also in an optical microscope (see Figs. 31-34). These data were used to position the sample in the XRF system. At this point we can only say that our experiment indicated that shunts are associated with metal contaminants, and that these contaminants are likely to be heavy metals. A series of experiments is required to obtain a statistically significant representation of the probability of finding one or another metal at the location of a shunt. The hypothesis that shunts may be associated with titanium is physically plausible because Ti has a very low diffusivity in silicon, and cannot be efficiently gettered by non-proximity gettering techniques unless the gettering is performed for a long time and at very high temperatures. Therefore, it should be very difficult to eliminate shunts from the solar cells by gettering.

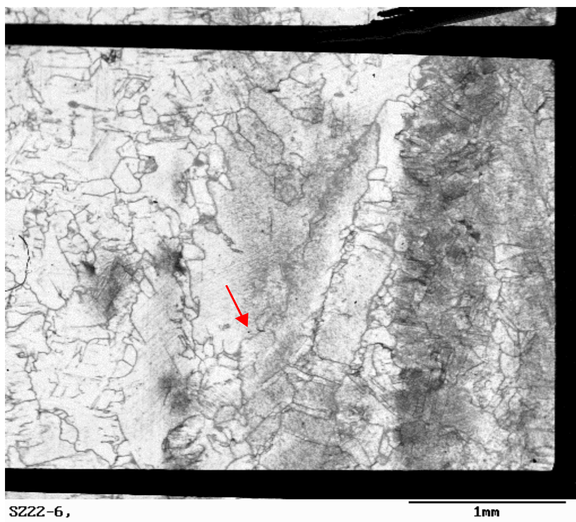

Fig. 31: EBIC images of the solar cell which was found by infra-red thermography to contain a shunt. Arrow indicates shunt position.

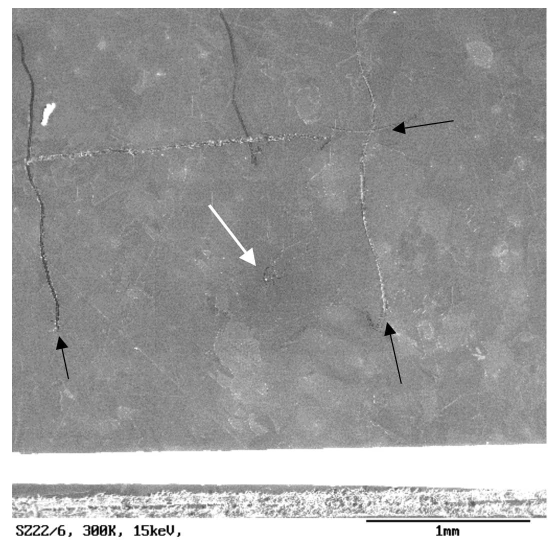

Fig. 32: Secondary electron image showing the position of the shunt relative to grain boundaries and scratches on the sample. Dark arrows mark scratches on the surface which were used to locate the shunt.

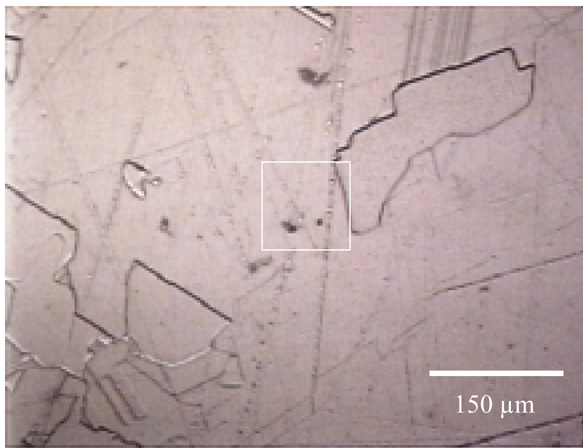

Fig. 33. 20X Optical image of the smaple. White box denotes XRF scan area.

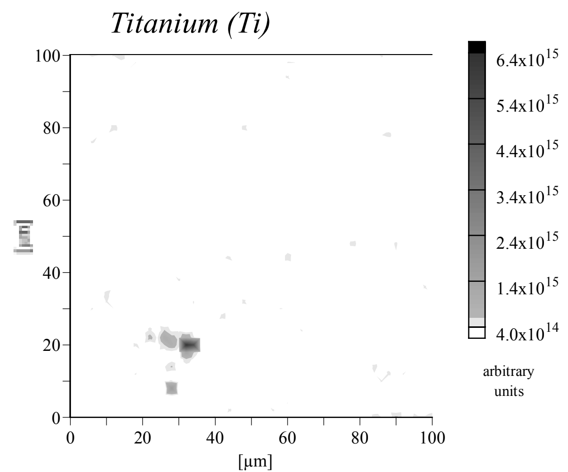

Fig. 34. XRF map of Ti in sample 22-6

6 Study of chemical state and stability of iron precipitates in silicon

The dissolution rate or stability of metal precipitates with the application of a thermal treatment is an important factor for solar cell technology, which may affect the degree to which the minority carrier diffusion length in a wafer can be improved by gettering. Stability of precipitates is determined by the thermodynamic balance between metal precipitates and dissolved metal impurities in the silicon lattice. For nm-scale precipitates in silicon crystals, complete dissolution is possible since the silicon material generally is of sufficient volume to absorb all dissolved impurities afforded by the precipitates. The thermodynamic balance is primarily determined by the chemical state of the metal precipitate. The strain field of a structural defect and native point defect concentration may slightly alter the balance but these effects are thought to be minor compared to a variation in the chemical state of the precipitate.

Past research has been only partially successful in determining the chemical state of metal precipitates at structural defects in silicon mainly because of the small sampling volume and poor sensitivity of standard characterization techniques. The chemical state of copper precipitates has only been identified when precipitated at unspecified structural defects, typically near the surface, where the copper was found to be in a low-temperature polymorph form of Cu_3Si [49, 53, 92, 205]. The chemical state of nickel, cobalt and palladium precipitates has also been studied when precipitated near the surface [50, 52] (see also [10] and references therein). Studies of iron have concentrated on iron reactions with a $Si\text{-}SiO_2$ interface, where both $FeSi_2$ and a modified form of Fe_2SiO_4 phases have been detected [93, 113, 128]. While these studies suggest chemical phases that can form in silicon, they do not directly show which phases actually form at structural defects such as oxygen precipitates, dislocations and stacking faults where the presence of oxygen, carbon and strain fields may modify the phase transformation process. Identification of the chemical state at these defects is of critical importance to fully understand the stability of metal precipitates in solar cells.

The work presented in this section is a study of the chemical state and stability of metal precipitates at dislocations in polycrystalline silicon and at oxygen precipitates and their growth-related defects in single-crystal silicon. We utilize the novel characterization techniques of synchrotron-based X-ray fluorescence and X-ray absorption microscopy to determine elemental distribution and the chemical state of nm-scale precipitates of iron and copper in silicon. Based on our results, we discuss the effect of oxygen-metal reactions in regards to precipitate stability.

X-ray fluorescence (XRF) and X-ray absorption spectroscopy (XAS) were performed at the Advanced Light Source, Lawrence Berkeley National Laboratory (in collaboration with Dr. S.A.McHugo, whose work was funded through DOE) in order to ascertain elemental distribution and chemical state, respectively, of metals in the silicon material. Both XRF and XAS analysis were performed with X-rays focused to a spot size of 1-2 μm^2, with scan areas typically over hundreds of microns. Considering typical sampling depth for 3d transition metals with XRF and XAS are on the order of 10-80 μm, the sampling volumes are significant. Furthermore, the μ-XRF system is capable of detecting metal precipitates with radii > 20 nm, which is superior to other standard characterization techniques such as secondary ion mass spectroscopy. This combination of large sampling volume and high sensitivity allows for analysis that was previously unachievable.

The μ-XRF system detects fluorescent X-rays emanating from the material after excitation with a wide band pass, 12.4 keV energy X-ray beam. The energy of the fluorescent X-rays signifies the elements present. The μ-XAS system detects changes in the excitation of core-level electrons into empty valence band states with the use of a narrow band pass, variable energy X-ray beam. By

monitoring the absorption of the impinging X-ray beam as the energy of the beams varied, we obtain a fingerprint of the chemical state of the element, which is compared to standard samples of known chemical state. Since the valence band electrons are sensitive to variations in chemical binding, this technique provides an excellent means for chemical identification.

Fe Kα and Kβ X-ray emissions were detected in as-grown polysilicon with the μ-XRF system. The energy position and relative ratio of Fe Kα to Kβ clearly identified the fluorescent X-rays as those from Fe in the polysilicon. The Fe signal was compared to a standard sample of known Fe dose to obtain a peak concentration of 5×10^{16} Fe atoms/cm^2. If we assume that the Fe is precipitated as one

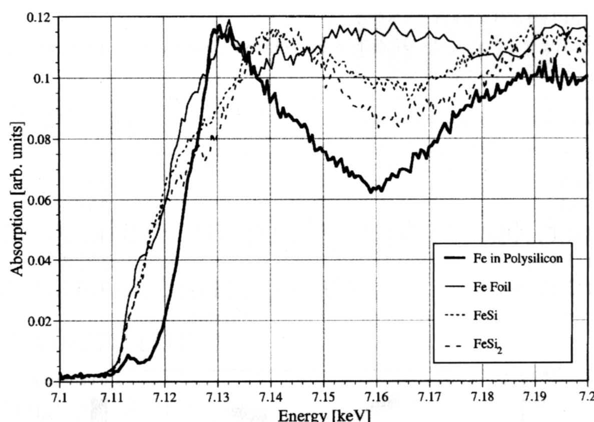

Fig. 35. X-ray absorption spectra from Fe in polysilicon, FeSi, $FeSi_2$ and metallic Fe.

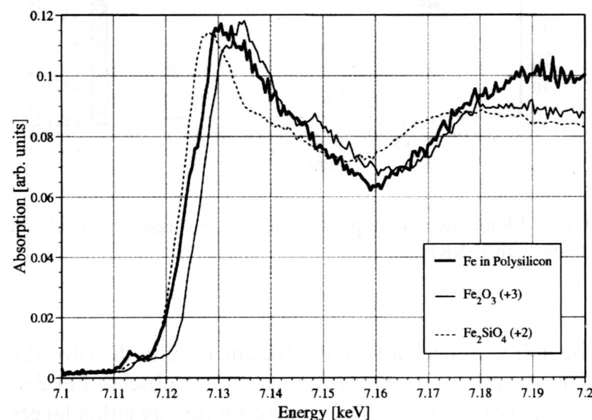

Fig. 36. X-ray absorption spectra from Fe in polysilicon, α-Fe_2O_3 (+3 charge state) and Fe_2SiO_4 (+2 charge state).

precipitate, located within the top 5 μm of the sample, the precipitate size can be calculated to be 288 nm. However, considering earlier work [91], the Fe is more likely a fine dispersion of small precipitates.

The absorption spectra of the Fe precipitate(s) in the polysilicon sample is shown in Fig. 35, 36, which is the summation of 19 spectral scans taken with the μ-XAS system. Multiple XAS scans are also shown in Fig. 35 for Fe, FeSi and $FeSi_2$ standards. Fe silicides would be expected to form in this material since silicide formation temperatures are in the same range as crystal growth temperatures. We observe little similarity between the absorption spectra, indicating that Fe in the polysilicon is not Fe, FeSi nor $FeSi_2$. This is unexpected considering the matrix is silicon.

The shift of the absorption edge for the Fe spectra suggests the Fe atoms have been elevated to a higher valence state. This is common for metal oxides and metal silicates but not for metallic iron or Fe silicides. Furthermore, the presence of the pre-edge structure indicates the local environment of the Fe atoms in this compound is highly asymmetric, which again is common for oxides and silicates but not for metallic Fe or Fe silicides. Further indications of Fe-related complexes comes from other research, which has indicated that Fe may complex with oxygen precipitates in silicon (see, e.g., the literature analysis presented in our report for the 3-rd quarter of 1999, or its summary in Sec. 4.1 above).

With these possibilities in mind, we analyzed standard powders of α-Fe_2O_3 and Fe_2SiO_4 with the μ-XAS beamline for comparison to the Fe in the polysilicon. Results are shown in Fig. 36. We observe some similarity between the absorption spectra of the metal oxides and silicates with the Fe in polysilicon. In particular, the pre-edge structure is remarkably similar. Furthermore, the absorption edge of Fe in polysilicon falls between α-Fe_2O_3 and Fe_2SiO_4. Considering Fe in α-Fe_2O_3 is in a +3 charge state and Fe_2SiO_4 is in a +2 charge state, the Fe in polysilicon seems to be a mix of +2 and +3

charge states. From these comparisons, one may suggest the Fe in polysilicon is in a mixed state of oxide and silicate. These results compare well with Kitano [93] who observed the formation of a mixed +2, +3 state of Fe_2SiO_4 with Fe reaction at a Si-SiO_2 interface.

Table 3. Enthalpies of formation of Fe related compounds.

Compound	ΔH (KJ/mol)
FeSi	-39.3
$FeSi_2$	-30.6
½ Fe_2O_3	-412.1
1/3 Fe_3O_4	-372.8
½ Fe_2SiO_4	-740

With the iron in an oxide or silicate state, the ability to remove or getter the iron from the material is greatly hindered by the high binding energy of iron to oxides and silicates relative to iron silicides. Table 3 lists the standard molar enthalpy of formation for iron silicides, oxides, and silicates at 298 K, data from [206, 207]. The data has not been corrected for compound formation within a silicon matrix, however, these numbers provide a relative indication of binding energy. From the data, the thermodynamic formation energies of iron oxides and silicate are significantly higher than iron silicides, thus, the binding energy of the iron atom to an oxide or silicate precipitate is higher than to a silicide precipitate. With a higher binding energy, the solubility of Fe in the presence of an oxide or silicate precipitate will be low, compared to the presence of a silicide precipitate. Since dissolution is a flux-limited process, this lower solubility decreases the dissolution rate, i.e., the gettering rate. This result has significant impact on solar cell improvements via gettering as well as for the robustness of gettering at oxygen precipitates in IC-grade silicon.

Based on our results we can conclude that Fe in polysilicon solar cells can be in the form of an oxide or a silicate. This is contrary to common thought, where a Fe silicide is expected to form. With the iron being in the form of an oxide of silicate, the rate of impurity removal is significantly reduced due to higher binding energy of Fe atoms to oxides or silicates as compared to silicides.

7 Application of X-ray fluorescence microprobe technique to the analysis of fully processed solar cells

XRF studies of metal impurities in multicrystalline silicon, performed by our group in the past, involved extensive sample preparation, which included chemical cleaning of the samples and removal of the metal contact used for their characterization by LBIC, EBIC, or thermography. An important step of the experiment was to create marks on the sample surface to establish a one-to-one correspondence between the XRF-map and the recombination activity/thermography map. Features revealed by selective etching, such as grain boundaries (see, e.g., the example of Sec. 7) and scratches on the sample surface were used as such marks in the initial experiments. However, this involved tedious and often destructive sample preparation. Therefore, it was important to develop a procedure for analysis of impurities in fully processed solar cells without etching and scratching of the samples.

In this section, we report the results obtained on solar cells fabricated at Fraunhofer Institute for Solar Energy Systems using BaySix material. The processed solar cells were square in shape with sides measuring 47 mm. This relatively small size enabled us to install the whole cell in the sample holder, although only a small area of the cell (on the order of 0.01-0.02 mm^2) could be scanned within a reasonable period of time. The top grid consisted of thin contact strips made of evaporated TiPdAg, additionally electroplated with Ag, with approximately 2.2 mm between them. The cells were pre-characterized by LBIC. To analyze the distribution of metal impurities in the cells, they were installed in an XRF microprobe system, ALS beamline 10.3.1, without any preliminary surface preparation, to check whether the fluorescence map of a metal from the contact grid on the cell surface (evaporated TiPdAg, additionally electroplated with Ag) could supply sufficient features to be used to pinpoint the area of the scan and to link it to optical and EBIC micrographs.

We found that contact strips generated a fluorescence signal, which consisted of a background signal and a number of overlapping peaks with energies of around 1.5keV (close to the K_α Al) and around 3 keV (L_α-L_β Ag). No signal was found for the most intense K_α Ti line indicating a full absorption of the radiation in the upper silver layer. L_α-L_β Ag lines interfere strongly with the Ar lines. We found that the XRF-image giving the most topographical details of the metal strip contacts can be obtained using the spectral area around 1.5 eV, although the element which originates the signal in this area is not known precisely. Fig. 37 presents two complimentary maps with sensitivity tuned for silicon and for aluminum. The contact strip is clearly seen, with a strong contrast between the strip and the silicon. A dotted line in Fig. 37 schematically indicates the position of a grain boundary which we observed also in an optical microscope.

Fig. 38 is a comparison of an XRF scan of the same area of the cell as presented in Fig. 37 (note that the scan presented in Fig. 37 was taken with the sample orientation 180 degrees rotated from its position in Fig. 38). The characteristic features (uneven edge) of the contact strip, indicated by arrows in the XRF image, can also be clearly seen in the optical micrograph. This unambiguous correlation of characteristic features of the contact strip edges on optical and XRF maps has been successfully used in this set of experiments for locating the same area of the sample in subsequent experiments. Interestingly, the grain boundary, which is well seen in the optical microscope, is not detectable in the XRF image.

The area of the cell mapped in Figs. 37,38 was selected using LBIC map of the whole cell, shown in Fig. 39. On the LBIC map we selected a small area which contained a defect cluster with significantly lower diffusion length than in the nearby area. The blown-up image of the cluster is

shown in the upper right corner of Fig. 39. The location of this enlarged area of the solar cell on the overview LBIC map is shown by a rectangle (left-hand side of Fig.3). The image in the right bottom corner of Fig. 39 is the optical image of the area of the cell. The whole area of this optical image corresponds to the area within the rectangle on the enlarged LBIC image in the upper-right corner of Fig. 43. Finally, the area which was actually scanned by XRF, approximately 150×100 microns, is shown by a rectangle in the optical image.

The XRF map of copper distribution in this area of the cell is shown in Fig. 40; the XRF map of iron distribution in the same area of the cell is presented in Fig. 42. Fig. 41 is the energy scan of the XRF signal from copper precipitate located at the bottom of Fig. 40. This scan indicates that the precipitate consists of copper with inclusions of iron. Indeed, the location of this precipitate can also be traced as a weak contrast on the iron map, Fig. 42. Note that the two iron precipitates visible as dark spots in Fig. 42 are located in different spots than the copper precipitate.

In summary, we have demonstrated that our XRF tool is suitable for analysis of metal impurity clusters in processed solar cells without chemical etching. The metallization grid on the cell surface does not significantly interfere with the measurements and can even be used as a marker to accurately pinpoint the location of the area of interest on the cell. Our results confirm that iron and copper clusters are indeed found in low lifetime regions of solar cells. A copper precipitate was found on the grain boundary, and it was found that copper has co-precipitated with iron.

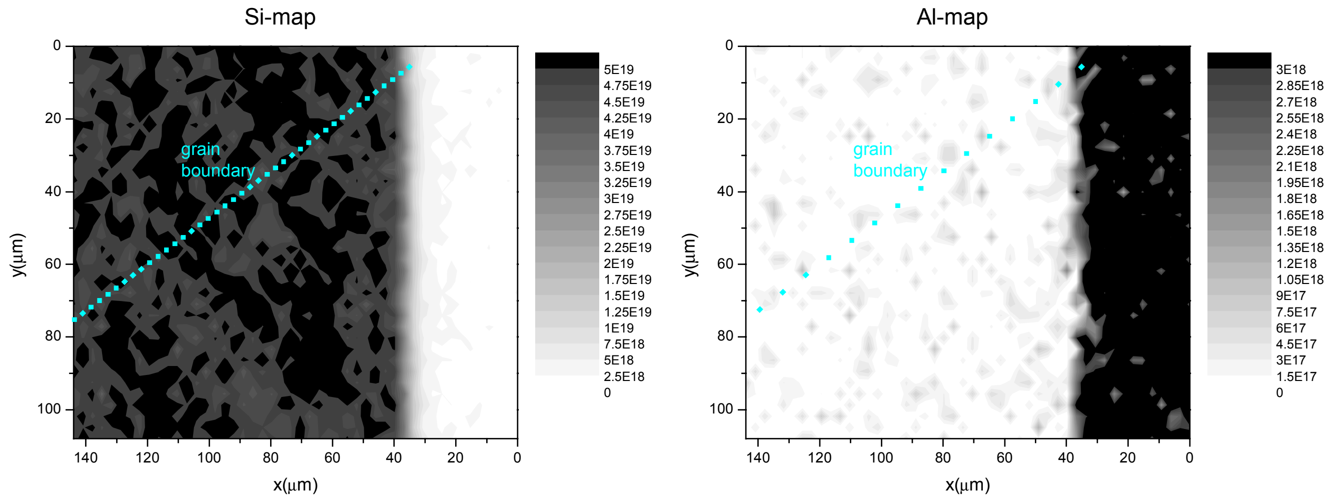

Fig. 37. XRF scans of the same area of the wafer, tuned to sensitivity to the silicon peak (on the left) and the Al peak (which strongly overlaps with the numerous heavy metals constituting the contact strips). The contact strip is clearly seen. The silicon fluorescence signal under the contact strip is attenuated by the metal. A dotted line schematically represents the location of a grain boundary, which is shown in greater detail in the following figures.

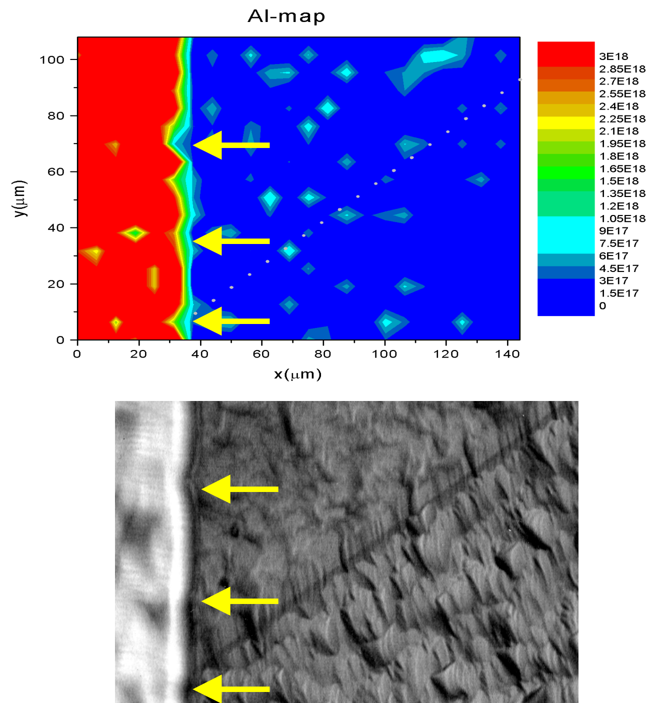

Fig. 38. Comparison of the same area of the cell imaged by XRF and optical microscopy. Features at the edge of contact stripes can easily be identified by both techniques.

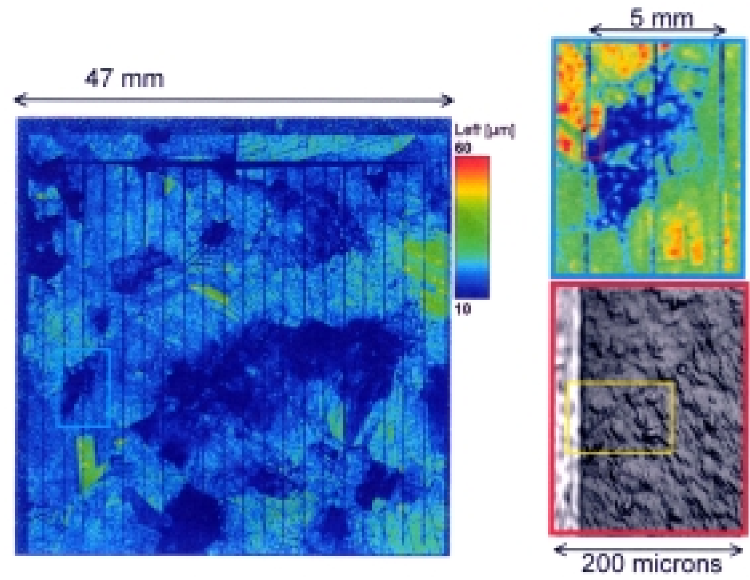

Fig. 39. LBIC image of a solar cell (on the left) with an area of local low minority carrier diffusion length shown on a large scale in the top right corner of the figure. This area is shown on a large-scale LBIC image by a rectangle, which encompasses 2,3, and 4-th contact strips from the left. The red rectangle on the blown-up LBIC image shows the boundaries of the optical image (presented in the right bottom corner of the figure). The boundary of a contact strip and a grain boundary can be well seen in the optical image. The yellow rectangle indicates the area scanned with XRF (it is the same area as mapped in Fig. 2).

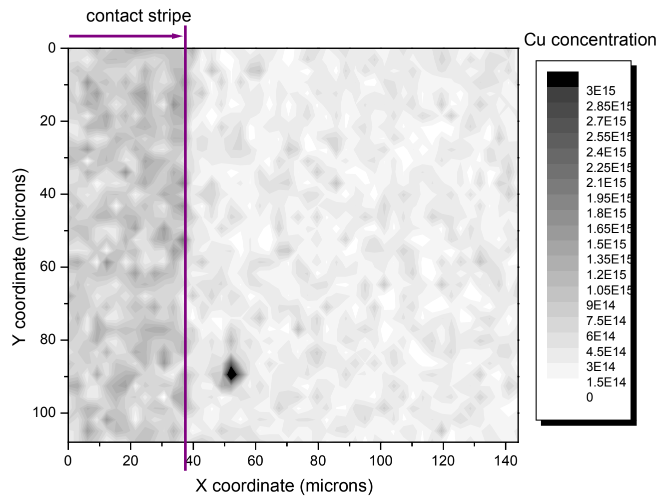

Fig. 40. XRF scan of copper distribution in the local low diffusion length area of the cell. The optical image of this area is shown in Fig. 38. A copper precipitate with a strong XRF peak was found at the location of a grain boundary.

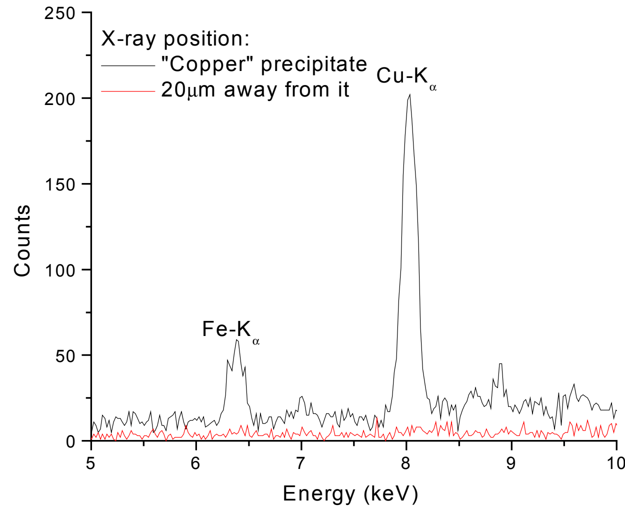

Fig. 41. Energy scan of the XRF signal from the copper precipitate identified in Fig. 4 showed that copper has co-precipitated with a small amount of iron. A red line illustrates the background signal, measured at an arbitrary location about 20 microns away from the Cu precipitate.

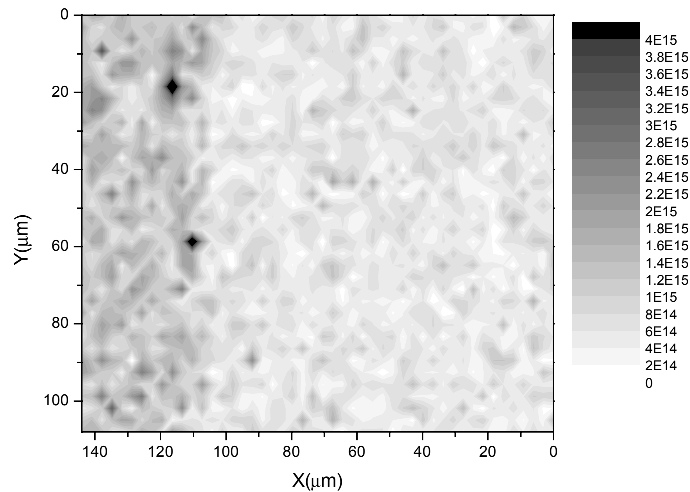

Fig.42. XRF scan of iron distribution in the local low diffusion length area of the cell. The mapped area is identical to that presented in Fig. 5. The optical image of this area is shown in Fig. 3. Two iron precipitates are found in the area away from the grain boundary. The location of copper precipitate visible in Fig. 3, which, as follows from Fig. 4, also contains some iron, can be seen in this figure as a weak green contrast at the same spot as in Fig. 3.

8 Development of an experimental procedure to locate defects in-situ in a beam line

One of the problems of application of X-ray microprobes to mc-Si is that each data point requires an accumulation time of at least several seconds. Consequently, only a small area of the sample can be scanned with a good resolution. As a rule, we are interested in determining the metal content of the areas of low diffusion length on the wafer. Our experience shows that it is quite unlikely to find metals in the areas of locally high diffusion length. Therefore, it would be desirable, to save beamline time wasted on measuring each point within a rectangular area, first find in-situ the areas of locally short diffusion length, and then perform XRF analysis in these areas only. Although EBIC enables one to find areas with low diffusion length with high spatial resolution, there remains a problem of how to move the sample to the beamline and focus the X-ray beam to precisely the same spot.

To simplify this task, we developed and demonstrated the proof of principle of a new technique, X-ray Beam Induced Current (XBIC), which enables one to easily and quickly locate grain boundaries and electrically active defects without removing the sample from the beamline. This powerful in-situ technique can be used to locate recombination active defects, oxide shorts, or p-n junctions, and will be used in the subsequent research for elemental and chemical x-ray characterization of impurities in solar cells.

XBIC is essentially the same technique as EBIC except that the minority carriers are generated by monochromatic x-rays. As it is well known, EBIC technique is a very useful method for locating electrically active defects and junctions. In EBIC, the electron beam of the SEM is used to inject charge carriers, while in XBIC, the minority carriers are generated by X-ray beam in a small region of the sample. The sample itself acts as a detector of electronic charge. What is then measured in EBIC and XBIC is the charge collection efficiency, which depends upon numerous spatially inhomogeneous factors including electrically active defects. Such defects reduce the charge collection efficiency. The detection of charge carriers requires some type of electric field either internally from a p-n junction or externally supplied by an applied voltage or both. The electron beam or x-ray beam is scanned across the surface and the collected current is measured to form an image of electrically active defects.

However, there are some significant differences between EBIC and XBIC. In EBIC, the resolution of the image is primarily determined by the size of the electron cloud generated in the sample by the impinging electron beam, and can range from 1 to 10 μm depending upon the accelerating voltage of the electrons. For a narrow x-ray beam, similar resolutions would be expected. The depth distribution of the electron beam generated electrons is somewhat spherical while the x-ray generated depth distribution determined by the exponential absorption profile of the x-rays. An interesting feature of EBIC or XBIC is that even very small defects, i.e. precipitates less than 80nm or decorated dislocations, can be easily imaged as micron sized features as long as the defects are highly electrically active.

The feasibility of XBIC was demonstrated at beamline 7.3.1.2 at the Advance Light Source, which is the microXPS technique, utilizing relatively small x-ray energies to study near-surface defects. The x-rays at this beamline are generated by a bend magnet. An intense monochromatic x-ray beam with approximately $\approx 10^{10}$ photons/s focused to a 2μm spot in the soft x-ray range is delivered to the sample. In this work, we applied this technique to the edge-defined film-fed grown (EFG) polysilicon sample, slightly etched to remove any surface contamination. After an RCA clean, an aluminum diode of 3mm diameter and ≈300nm thick was evaporated on one side, and a 500nm

Au contact was evaporated on the other side. The sample was inserted into beamline 7.3.1.2 using an automated sample transfer system. The sample holder makes an electrical contact when inserted with which to measure the collected current as a function of beam position and beam energy. No external voltage was applied, only the electric field from the aluminum Schottky diode was utilized to collect minority carriers.

Figure 43 shows an XBIC image taken using a photon energy of 1000eV and represents an area of 180x180μm. A grain boundary can be clearly observed as the dark line. The dark line is

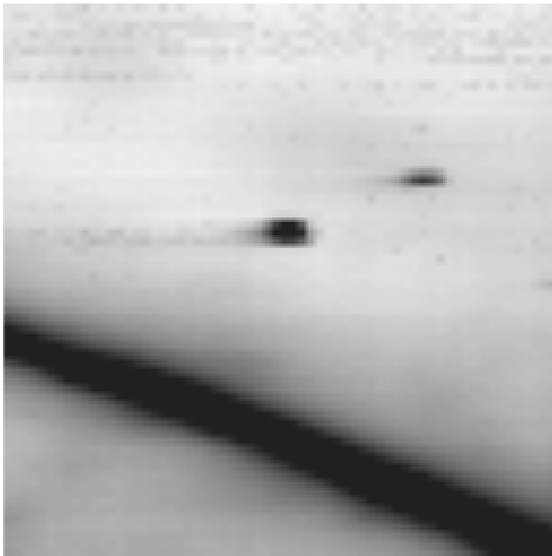

Fig. 43: XBIC image of a grain boundary and point defects. Xray energy of 1000eV has a penetration depth of approximately 2.2μm (180x180μm).

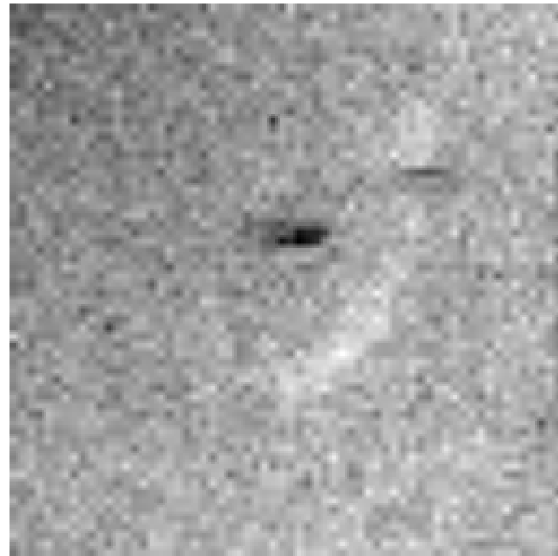

Fig. 44: Secondary electron image (any electrons from 2 to 20eV) of same area as in Fig. 43. The grain boundary is not observed in this image. The spots are observed, and are thus surface features.

approximately 30μm wide. Since the grain boundary is physically much smaller, we can estimate that the electron generation volume is approximately on the order of 15μm. This wide generation volume is partially due to the fact that the photons enter the sample at a 60° angle rather than 90°. There are also two dark spots in the upper right hand corner. A secondary electron image of the same area, also taken using X-ray beam as a probe, is shown in Fig. 44 and the two spots are still observed. The grain boundary, however, is not observed in this image. Thus it can be concluded that the spots are surface artifacts, either particulates or imperfections in the aluminum diode. At 1000eV, the penetration depth of the x-rays at a 60° angle is approximately 2.3 μm. The depth vs. photon energy for this configuration is shown in Fig. 45.

The incoming photon energy can be adjusted, changing the penetration depth of the x-rays. In Fig. 46, three images were made using different X-ray energies, 800, 950, and 1200 eV. As the photon energy increases, the X-ray penetration depth, the electron generation volume, and the total number of electrons generated, all increase. A byproduct is that the image contrast also increases as is observed in EBIC as the electron acceleration voltage is increased. One can see new features arise with increasing photon energy. This is a result of the increased penetration depth. Thus, the depth of an electrically active defect can be estimated by observing the onset of contrasts as the photon energy is increased. In this case, there seems to be a precipitate at the grain boundary 3 to 4 μm below the

surface. Again, the secondary electron image, shown for the 950 eV photon energy in Fig. 51, shows none of the features of the XBIC images proving that the XBIC features are not surface artifacts.

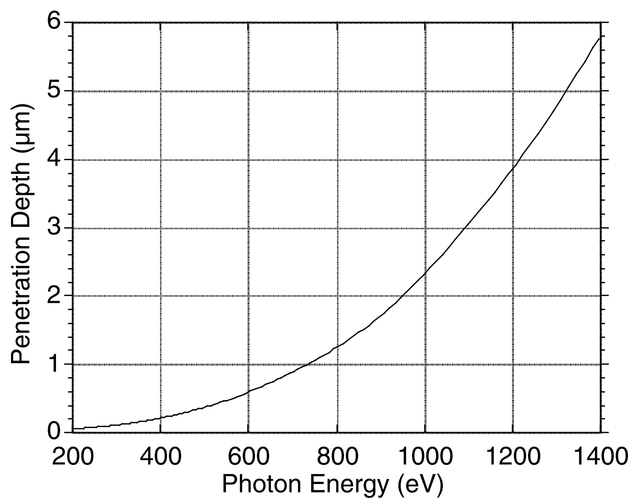

Fig. 45. Penetration depth as a function of photon energy with an incident angle of 60°.

Elemental information may even be obtained from the collected current. If the photon energy matches an absorption peak of an element in the x-ray probe volume, the resulting increase in the number of generated electrons would appear as an increase on collection efficiency, i.e. XBIC current. On the other hand, absorbing elements in the aluminum diode or at the aluminum-silicon interface would screen incoming x-rays, resulting in a drop of the observed XBIC current. In Fig. 48, the XBIC current is shown as a function of photon energy for two spots in Fig. 46 labeled D (dark) and L (light). Since the incoming photon flux varies with photon energy, the XBIC current was normalized by the incident flux. The normalized XBIC current increases with photon energy due to increased generation of minority carriers at higher energies. The drop off in XBIC current at approximately 1200 eV occurs because the minority carriers are generated further from the Schottky diode depletion region and thus few minority carriers are collected despite the increase in the minority carrier generation at higher energies. There are two features on the normalized XBIC current curves. There is a dip (loss of flux) at approximately 534 eV on both the light and dark curves. This is likely absorption by oxygen in a thin Al_2O_3 film on the diode. This absorption is similar in both spots and does not show up in the difference curve, D*L/(L-D). On the other hand, a feature on the dark curve at approximately 1070 eV does show up as a on the difference curve. The feature is likely to be a phosphourous 1s absorption which has an energy double that observed. This absorption due to the second harmonic from the monochromator. Other phosphorous absorption peaks are less than 400 eV and are not observed.

The next step in development of XBIC, which unfortunately was not achieved in this contract due to temporary technical difficulties at the beamline, is to set up XBIC technique on XRF beamline to be able to identify the metal clusters in low lifetime areas in situ.

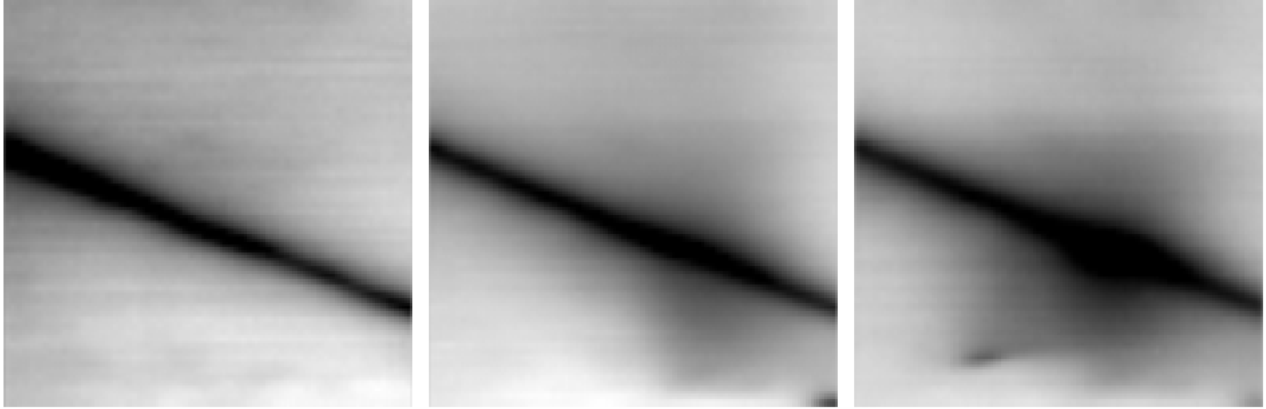

Fig. 46: Series of images taken with various energies, 800, 950, and 1200eV. These energies correspond to a penetration depth of 1.2, 2.0, and 3.8 µm.

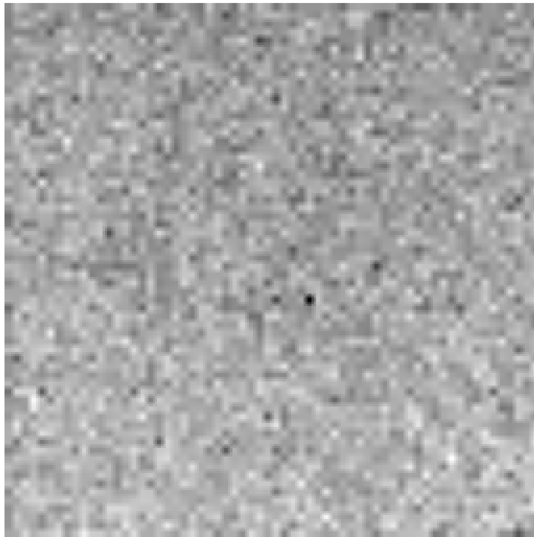

Fig. 47: Secondary electron image of same area at 950eV. The grain boundary is not observed in this image.

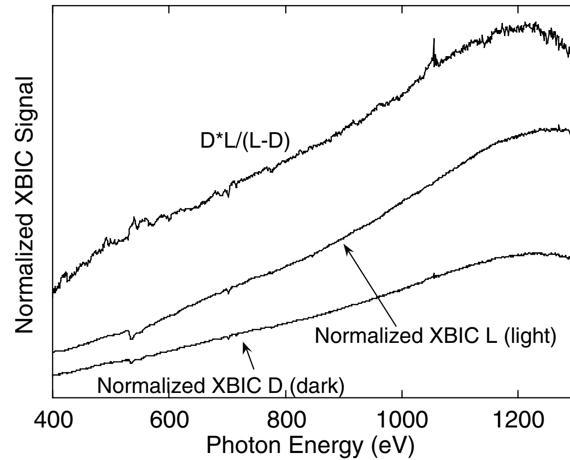

Fig. 48. The XBIC current normalized to the photon flux as a function of photon energy. The light and dark curves correspond to the light and dark regions labeled in Fig. 4. The light and dark curves were multiplied and then divided by the difference in order to obtain greater contrast.

In conclusion, we suggested a new method to facilitate the location of objects of interest in multicrystalline silicon for solar cell applications, and demonstrated it on the example of EFG material.

9 An attempt to apply the experimental techniques developed for interstitial copper to nickel in silicon.

As pointed out by Weber [31], low formation enthalpy of nickel in silicon can be considered an indication that it dissolves in the silicon lattice as a positively charged ion. This conclusion was based on results of the theoretical treatment of Van Vechten [208], who showed from general thermodynamic considerations that the formation enthalpy would be lower for dissolution of impurities which are ionized in silicon at the diffusion temperature than that for the neutral impurities. He calculated that dissolution of a neutral interstitial impurity would cost about 2.1 eV, whereas it should take only 1.4 eV to dissolve a positively charged interstitial impurity. Indeed, as was pointed out by Weber [31], transition metals in silicon can be distinguished into two subgroups according to their enthalpy of formation, $\Delta H=2.1\pm0.1$ eV for Cr, Mn, Fe, and Co, and $\Delta H=1.5\pm0.1$ eV for Ni and Cu. Since these experimentally determined values are very close to the predictions of Van Vechten [208], Weber [31] argued that Cu and Ni dissolve in silicon in the positive charge state. The positive charge state of Cu was indeed confirmed experimentally at high [209] and low [36] temperatures as well as by theoretical calculations [210, 211]. In contrast, the data on the charge state of Ni in Si are controversial. In this study we attempted to apply the experimental techniques developed to study interstitial copper in silicon to nickel-contaminated samples. If nickel is positively charged in silicon, then it should (a) compensate shallow acceptors, (b) quickly drift out of the depletion region when reverse bias voltage is applied, and (c) within a short time after the quench (no longer than a few days) either precipitate in the bulk or diffuse to the surface. Therefore, in our experiments we looked primarily at changes in electrical properties of the samples with the time of storage at room temperature or annealing on a hot plate.

FZ crystalline silicon samples with p-type conductivity were contaminated with Ni using a solution of NiCl in DI water. Diffusion was performed in a vertical furnace at 650^0C, 750^0C, and 850^0C and was terminated by quench in ethylene glycol. These temperatures correspond to the solubility of nickel of 8×10^{14} cm^{-3}, 6.5×10^{15} cm^{-3}, and 3.5×10^{16} cm^{-3}, respectively [30, 31]. The duration of anneal was sufficient to achieve a homogeneous distribution of Ni through the sample. Following the quench, the samples were stored in liquid nitrogen. The first capacitance measurements were performed after approximately 50 minutes of storage at room temperature after the quench. This time was required to perform chemical cleaning of the sample and to evaporate Schottky diodes. A Ni-correlated peak at approx. E_V+0.33 eV and a peak associated with inadvertent iron contamination were observed in the DLTS spectrum. However, no changes in the deep level spectrum, measured by DLTS, or in the doping level of the sample, as determined from capacitance-voltage measurements, was observed even after a week of storage at room temperature or after annealing the sample on a hot plate. This indicates that similarity between nickel and copper is not as close as we initially expected: there is no compensation of boron by mobile interstitial nickel, as it usually happens in the case of copper, and no metastable effects in the deep level spectra.

This finding can have two explanations: either interstitial nickel is neutral in silicon, as it was recently suggested by Hoelzl et al. [212], and therefore cannot be observed by Transient Ion Drift or as a change in netto doping level by capacitance-voltage measurements, or it precipitates completely during or immediately after the quench. The observation that nickel silicide fits silicon lattice almost perfectly [213] indicates that there is no lattice strains which can contribute to the precipitation barrier for nickel (as compared to the 150% lattice expansion known for copper). Additionally, nickel-silicide precipitates were shown to be negatively charged in silicon [214, 215]. Hence, there

will be no electrostatic barrier to repel nickel from the growing precipitates, as it is the case with copper. Hence, it appears that there may be a significant difference between the behavior of copper and nickel in silicon. Namely, the mechanisms which suppress bulk precipitation of copper seem not to work for nickel, which makes precipitation of nickel its preferred defect reaction that occurs immediately when sufficient supersaturation to overcome the initial nucleation barrier is reached. If this model is correct, one can expect formation of nickel precipitates everywhere in the wafer, whereas copper precipitates are more likely to be formed at existing defects, where the precipitation barrier is reduced due to tensile lattice strains or electrostatic effects. Further studies are necessary to ascertain the possible mechanisms of the impact of nickel on minority carrier diffusion length in silicon and its impact on solar cell efficiency. It should be emphasized that the available literature data [214, 215] indicate strong recombination activity of nickel precipitates in silicon.

10 Summary and outlook

A detailed list of major achievements of this subcontract is presented in the executive summary. This list, and the detailed report presented above, shows that major progress in understanding the physics of transition metals in silicon and their possible impact on the efficiency of solar cells was achieved during the three-year span of this subcontract. We found that metal-silicide precipitates and dissolved 3d transition metals can be relatively easily gettered. Gettering and passivating treatments have to take into account the individuality of each transition metal. Our studies demonstrated how significant is the difference between defect reactions of copper and iron. Copper does not significantly affect the minority carrier diffusion length in p-type silicon, at least as long as its concentration is low, but readily precipitates in n-type silicon. Therefore, copper precipitates may form in the area of p-n junctions and cause shunts in solar cells. Fortunately, copper precipitates are present mostly in the chemical state of copper-silicide and can relatively easily be dissolved. In contrast, iron was found to form clusters of iron-oxides and iron-silicates in the wafers. These clusters are thermodynamically stable even at high temperatures and are extremely difficult to remove. The formation of iron-silicates was observed at temperatures over 900^0C. We speculate that these compounds are formed in PV-grade mc-Si since it contains relatively high concentrations of both iron and oxygen.

A significant effort was focused on development of novel material characterization techniques, suitable for photovoltaics. These techniques are X-ray fluorescence microprobe analyses, particularly X-ray fluorescence and X-ray near-edge absorption spectroscopy. They allow one to detect metal precipitates as small as 80 nm in diameter, and map their distribution in a solar cell on a micron scale. We have shown that XRF microprobe can be used for characterization of fully processed solar cells, and applied the technique to characterization of metal content at the location of a shunt.

Our studies of recombination and electrical activity of metal-silicide precipitates explained why application of DLTS and other electrical characterization techniques to mc-Si or process cells did not detect any elelctrically active defects above the detection limit, although recombination centers were clearly present in the wafers. We showed that band-like states of extended defects and precipitates form extremely wide DLTS peaks, whose apparent amplitude is much lower than the actual impurity concentration.

On the other hand, our findings raised a number of new questions which have to be resolved. We hope to address these questions in the next round of the NREL-sponsored research program. These questions include (but not limited to) the following issues:

1. Using a combination of XBIC and XRF, determine what fraction of recombination-active defects in a solar cell contains clusters of transition metals.
2. Determine the recombination activity of gettering-resistant metal clusters, such as metal-oxides and metal-silicates.
3. Determine what other metals, besides Fe, Cu, and Ni, are commonly found in fully processed solar cells.
4. Address in greater detail the nature of shunts in solar cells.
5. Study the kinetics of defect reactions between extended defects (dislocations and grain boundaries), dissolved interstitial oxygen, and metals during solar cell production. Determine the likelihood of the formation of gettering-resistant compounds for different growth techniques and establish a correlation of the density of these defects with crystallization rate, density of lattice defects (such as dislocations and grain boundaries), and concentration of oxygen and carbon.

6. Compare the efficiency of the available passivation techniques, including SiN passivation, for different types of metal clusters in silicon.
7. Address the problem of recombination activity of “clean” lattice defects, such as agglomerates of self-interstitials, vacancies, oxygen, and carbon.

11 Publications supported by the subcontract XAF-8-17607-04

1. A.A.Istratov and E.R.Weber, "The role of transition metals in solar cell efficiency", in 11-th workshop on crystalline silicon solar cell materials and processes, B. L. Sopori, Editor, NREL, Golden, CO (2001) (in print).
2. O.F.Vyvenko, A.A.Istratov, A.Buonassisi, E.R.Weber, and R.Schindler, "Application of X-ray fluorescence microprobe technique for the analysis of fully processed solar cells", in 11-th workshop on crystalline silicon solar cell materials and processes, B. L. Sopori, Editor, NREL, Golden, CO (2001) (in print).
3. R.Sachdeva, A.A.Istratov, and E.R.Weber, "Impact of copper on minority carrier diffusion length in p-type and n-type silicon", in 11-th workshop on crystalline silicon solar cell materials and processes, B. L. Sopori, Editor, NREL, Golden, CO (2001) (in print).
4. A.A.Istratov, H.Hieslmair, O.F.Vyvenko, E.R.Weber, and R.Schindler, “Defect recognition and impurity detection techniques in crystalline silicon for solar cells”, Solar Energy Materials and Solar Cells (2001), in print.
5. A.A.Istratov, R.Sachdeva, C.Flink, S.Balasubramanian, and E.R.Weber, “Precipitation kinetics and recombination activity of Cu in Si in the presence of gettering sites”, proceedings of the international conference Gettering and Defect Engineering in Semiconductor Technology GADEST-2001, Solid State Phenomena (2001), in print.
6. S. A. McHugo, A. C. Thompson, C. Flink, E. R. Weber, G. Lamble, B. Gunion, A. MacDowell, R. Celestre, H. A. Padmore, and Z. Hussain, "Synchrotron-based impurity mapping", J. Cryst. Growth 210, 395 (2000).
7. S. A. McHugo and C. Flink, "Thermal stability of copper precipitates in silicon", Appl. Phys. Lett. 77, 3598 (2000).
8. A. A. Istratov, H. Hiesimair, and E. R. Weber, "Advanced gettering techniques in ULSI technology", MRS Bulletin 25, 33 (2000).
9. A. A. Istratov, H. Hieslmair, and E. R. Weber, "Iron contamination in silicon technology", Appl. Phys. A 70, 489 (2000).
10. C. Flink, H. Feick, S. A. McHugo, W. Seifert, H. Hieslmair, T. Heiser, A. A. Istratov, and E. R. Weber, "Out-diffusion and precipitation of copper in silicon: An electrostatic model", Phys. Rev. Lett. 85, 4900 (2000).
11. H. Kohno, H. Hiesimair, A. A. Istratov, and E. R. Weber, "Temperature dependence of the iron donor level in silicon at device processing temperatures", Appl. Phys. Lett. 76, 2734 (2000).
12. A. A. Istratov, C. F. Flink, H. Hieslmair, S. A. McHugo, and E. R. Weber, "Diffusion, solubility, and gettering of copper in silicon", Mater. Sci. Engineering B 72, 99 (2000).
13. A. A. Istratov, H. Hieslmair, and E. R. Weber, "Iron and its complexes in silicon", Appl. Phys. A 69, 13 (1999).
14. S. A. McHugo, A. C. Thompson, G. Lamble, C. Flink, and E. R. Weber, "Metal impurity precipitates in silicon: chemical state and stability", Physica B 273-274, 371 (1999).
15. C. Flink, H. Feick, S. A. McHugo, A. Mohammed, W. Seifert, H. Hieslmair, T. Heiser, A. Istratov, and E. R. Weber, "Formation of copper precipitates in silicon", Physica B 273-274, 437 (1999).

16. A. A. Istratov, H. Hedemann, M. Seibt, O. F. Vyvenko, W. Schröter, T. Heiser, C. Flink, H. Hieslmair, and E. R. Weber, "Electrical and recombination properties of copper-silicide precipitates in silicon", J. Electrochem. Soc. 145, 3889 (1998).
17. A. A. Istratov, C. Flink, H. Hieslmair, E. R. Weber, and T. Heiser, "Intrinsic diffusion coefficient of interstitial copper in silicon", Phys. Rev. Lett. 81, 1243 (1998).
18. H. Hieslmair, A. A. Istratov, T. Heiser, and E. R. Weber, "Evaluation of precipitate densities and capture radii from the analysis of precipitation kinetics", J. Appl. Phys. 84, 713 (1998).
19. C. Flink, S. A. McHugo, W. Seifert, M. Langenkamp, A. A. Istratov, R. Sachdeva, and E. R. Weber, "Application of synchrotron radiation-based X-ray fluorescence microprobe to detect impurities at the location of a shunt", in 10-th workshop on crystalline silicon solar cell materials and processes, B. L. Sopori, Editor, p. 212, NREL, Golden, CO (2000).
20. H. Hieslmair, "New synchrotron-radiation based technique to study localized defects in silicon: "EBIC" with X-ray excitation", in 10-th workshop on crystalline silicon solar cell materials and processes, B. L. Sopori, Editor, p. 162, NREL, Golden, CO (2000).
21. S. A. McHugo, A. C. Thompson, C. Flink, and E. R. Weber, "Copper precipitate dissolution in silicon", in 10-th workshop on crystalline silicon solar cell materials and processes, B. L. Sopori, Editor, p. 200, NREL, Golden, CO (2000).
22. E. R. Weber and A. A. Istratov, "Transition metals in silicon: the continuing story", in 10-th workshop on crystalline silicon solar cell materials and processes, B. L. Sopori, Editor, p. 8, NREL, Golden, CO (2000).
23. C. Flink, S. Balasubramanian, A. A. Istratov, R. Sachdeva, and E. Weber, "Study of precipitation/outdiffusion of copper in CZ and EFG silicon wafers", in 10-th workshop on crystalline silicon solar cell materials and processes, B. L. Sopori, Editor, p. 216, NREL, Golden, CO (2000).
24. E. R. Weber, S. A. McHugo, A. A. Istratov, C. Flink, and H. Hieslmair, "Identification of metal-oxygen complexes as lifetime limiting defects in solar cell materials", in Proceedings of the NCPV program review meeting 2000, p. 131, NREL, Denver, CO (2000).
25. H. Hieslmair, A. A. Istratov, C. Flink, and E. R. Weber, "Fe/Cu precipitation and precipitate dissolution in silicon", in Proceedings of the 15th NCPV photovoltaics program review, M. Al-Jassim, J. P. Thornton, and J. M. Jee, Editors, p. 418, American Institute of Physics, Woodbury, NY (1999).
26. A. A. Istratov, H. Hiesimair, and E. R. Weber, "Physics of iron in silicon: how much do we know after 35 years of research?" in Proceedings of the ninth workshop on crystalline silicon solar cell materials and processes, B. L. Sopori, Editor, p. 16, NREL, Breckenridge, CO (1999).
27. H. Hieslmair, A. A. Istratov, C. Flink, W. Seifert, S. A. McHugo, and E. R. Weber, "Experiments and computer simulations of p/p+ gettering of iron in silicon", in Proceedings of the ninth workshop on crystalline silicon solar cell materials and processes, B. L. Sopori, Editor, p. 143, NREL, Breckenridge, CO (1999).
28. C. Flink, H. Feick, S. A. McHugo, W. Seifert, H. Hieslmair, A. A. Istratov, and E. R. Weber, "About the reaction path of copper in silicon", in Proceedings of the ninth workshop on crystalline silicon solar cell materials and processes, B. L. Sopori, Editor, p. 144, NREL, Breckenridge, CO (1999).
29. A. A. Istratov, S. A. McHugo, H. Hieslmair, and E. R. Weber, "Improvement of material parameters of silicon by gettering", in Proceedings of the ninth workshop on crystalline

silicon solar cell materials and processes, B. L. Sopori, Editor, p. 153, NREL, Breckenridge, CO (1999).

30. A. A. Istratov, C. Flink, T. Heiser, H. Hieslmair, and E. R. Weber, "Interstitial copper in silicon", in Proceedings of the ninth workshop on crystalline silicon solar cell materials and processes, B. L. Sopori, Editor, p. 141, NREL, Copper Mountain, CO (1998).

Results of our work was presented at the following conferences and workshops:

1. 8th NREL workshop on crystalline silicon solar cell materials and processes (Copper Mountain, CO, U.S.A., August 17-19, 1998).
2. Gordon Research Conference "Point and Line Defects in Semiconductors" (New London, NH, U.S.A., July 12-17, 1998).
3. European Materials Research Society 1998 spring meeting (Strasbourg, France, June 16-19, 1998).
4. Eighth international symposium on silicon materials science and technology "Semiconductor Silicon-1998" (San Diego, CA, U.S.A., May 4-8, 1998).
5. 1998 Materials Research Society 1998 spring meeting (San Francisco, CA, U.S.A., April 13-17, 1998).
6. 15-th NCPV photovoltaics program review meeting (Denver, Colorado, September 1998).
7. 5th international workshop "Beam Injection Assessment of Defects in Semiconductors BIADS-98" (Wulkow, Germany, August 30 – September 3, 1998).
8. International conference on Extended Defects in Semiconductors EDS'98 (Jaszowiec, Poland, September 6-11, 1998).
9. 20th International Conference on Defects in Semiconductors ICDS-20 (Berkeley, California, July 26-30, 1999).
10. Fifth IUMRS International Conference on Advanced Materials (Beijing, China, June 13-18, 1999).
11. Ninth workshop on crystalline silicon solar cell materials and processes (Beaver Run Resort, Breckenridge, Colorado, USA, August 9-11, 1999).
12. National Center for Photovoltaics Program Review meeting (Denver, Colorado, U.S.A., April 16-19, 2000).
13. 10-th workshop on crystalline silicon solar cell materials and processes (Copper Mountain, CO, USA, Aug. 14-16, 2000).
14. 3rd international symposium on advanced science and technology of silicon materials (Aston Keauhou Beach Resort, Kona, Hawaii, USA, Nov. 20-24, 2000).
15. 2001 E-MRS meeting, Symposium E "Crystalline silicon for solar cells" (Strasbourg, June 5-8, France).
16. 11-th workshop on crystalline silicon solar cell materials and processes (Estes Park, CO, August 2001).

12 Acknowledgements

We would like to acknowledge fruitful collaboration with S.A.McHugo, whose work at the Advanced Light Source was funded by the US Department of Energy through LBNL, W.Schröter, M.Seibt, and H.Hedemann from the University of Göttingen, R.Schindler from Franunhofer Institute for Solar Systems, B.Sopori, R.McConnell, and T.Ciszek from NREL, and J.Kalejs from ASE Americas for their interest to our work and many helpful discussions.

13 References

1. T. Heiser and E. R. Weber, "Transient ion-drift-induced capacitance signals in semiconductors", *Phys. Rev. B* **58**, 3893 (1998).
2. A. A. Istratov, C. Flink, H. Hieslmair, E. R. Weber, and T. Heiser, "Intrinsic diffusion coefficient of interstitial copper in silicon", *Phys. Rev. Lett.* **81**, 1243 (1998).
3. R. N. Hall and J. H. Racette, "Diffusion and solubility of copper in extrinsic and intrinsic germanium, silicon, and gallium arsenide", *J. Appl. Phys.* **35**, 379 (1964).
4. A. A. Istratov, C. Flink, S. Balasubramanian, E. R. Weber, H. Hieslmair, S. A. McHugo, H. Hedemann, M. Seibt, and W. Schroter, "Progress in understanding the physics of copper in silicon", in *High Purity Silicon VI,* C. L. Claeys, P. Rai-Choudhury, M. Watanabe, P. Stallhofer, and H. J. Dawson, Editors, p. 258, The Electrochemical Soc., Pennington (2000).
5. A. A. Istratov and E. R. Weber, "Physics of copper in silicon", *J. Electrochem. Soc.*, to be published (2001).
6. A. A. Istratov, H. Hieslmair, and E. R. Weber, "Iron and its complexes in silicon", *Appl. Phys. A* **69**, 13 (1999).
7. A. A. Istratov, H. Hedemann, M. Seibt, O. F. Vyvenko, W. Schröter, T. Heiser, C. Flink, H. Hieslmair, and E. R. Weber, "Electrical and recombination properties of copper-silicide precipitates in silicon", *J. Electrochem. Soc.* **145**, 3889 (1998).
8. O. F. Vyvenko, "Minority carrier transient spectroscopy of copper-silicide and nickel-disilicide precipitates in silicon", *Solid State Phenom.* **63-64**, 301 (1998).
9. A. A. Istratov, H. Hieslmair, T. Heiser, C. Flink, E. R. Weber, W. Seifert, and M. Kittler, "Potential influence of the recombination of minority carriers at interstitial and precipitated copper in silicon on solar cell efficiency", in *Proceedings of the seventh workshop on the role of impurities and defects in silicon device processing,* B. L. Sopori, Editor, p. 158, NREL, Copper Mountain, CO (1997).
10. A. A. Istratov and E. R. Weber, "Electrical properties and recombination activity of copper, nickel and cobalt in silicon", *Appl. Phys. A* **66**, 123 (1998).
11. A. A. Istratov, O. F. Vyvenko, C. Flink, T. Heiser, H. Hieslmair, and E. R. Weber, "Charge state of copper silicide precipitates in silicon and its application to the understanding of copper precipitation kinetics", in *Defect & Impurity Engineered Semiconductors & Devices II,* S. Ashok, J. Chevallier, W. Goetz, B. Sopori, and K. Sumino, Editors, p. 313, Mat. Res. Soc., Pittsburgh (1998).
12. C. Flink, H. Feick, S. A. McHugo, W. Seifert, H. Hieslmair, T. Heiser, A. A. Istratov, and E. R. Weber, "Out-diffusion and precipitation of copper in silicon: An electrostatic model", *Phys. Rev. Lett.* **85**, 4900 (2000).
13. M. Ronay and R. G. Schad, "New insight into silicide formation: the creation of silicon self-interstitials", *Phys. Rev. Lett.* **64**, 2042 (1990).
14. A. A. Istratov and E. R. Weber, "The importance of understanding of the physics of copper in silicon for development and characterization of copper diffusion barriers", in *Copper interconnects, new contact metallurgies/structures, and low-K interlevel dielectrics,* G. S. Mathad, H. S. Rathore, B. C. Baker, C. Reidsma Simpson, and T. L. Ritzdorf, Editors, p. 90, The Electrochem. Soc., Pennington (2001).
15. S. A. McHugo, A. C. Thompson, G. Lamble, C. Flink, and E. R. Weber, "Metal impurity precipitates in silicon: chemical state and stability", *Physica B* **273-274**, 371 (1999).

16. S. A. McHugo, A. C. Thompson, C. Flink, and E. R. Weber, "Copper precipitate dissolution in silicon", in *10-th workshop on crystalline silicon solar cell materials and processes,* B. L. Sopori, Editor, p. 200, NREL, Golden, CO (2000).
17. A. A. Istratov, H. Hieslmair, and E. R. Weber, "Iron contamination in silicon technology", *Appl. Phys. A* **70**, 489 (2000).
18. C. Flink, S. A. McHugo, W. Seifert, M. Langenkamp, A. A. Istratov, R. Sachdeva, and E. R. Weber, "Application of synchrotron radiation-based X-ray fluorescence microprobe to detect impurities at the location of a shunt", in *10-th workshop on crystalline silicon solar cell materials and processes,* B. L. Sopori, Editor, p. 212, NREL, Golden, CO (2000).
19. H. Hieslmair, "New synchrotron-radiation based technique to study localized defects in silicon: "EBIC" with X-ray excitation", in *10-th workshop on crystalline silicon solar cell materials and processes,* B. L. Sopori, Editor, p. 162, NREL, Golden, CO (2000).
20. C. P. Khattak and K. V. Ravi, "Silicon processing for photovoltaics", North-Holland, Amsterdam (1985).
21. A. Huber, G. Böhm, and S. Pahlke, "Industrial applications of instrumental neutron activation analysis", *J. Radioanal. Nucl. Chem.* **169**, 93 (1993).
22. J. Bailey and E. R. Weber, "Precipitation of iron in polycrystalline silicon", *phys. stat. sol. (a)* **137**, 515 (1993).
23. J. Bailey, S. A. McHugo, H. Hieslmair, and E. R. Weber, "Efficiency-limiting defects in silicon solar cell material", *J. Electron. Mat.* **25**, 1417 (1996).
24. S. A. McHugo, J. Bailey, H. Hieslmair, and E. R. Weber, "Efficiency-limiting defects in polycrystalline silicon", in *Conference Record of the Twenty Fourth IEEE Photovoltaic Specialists Conference*, p. 1607, IEEE, New York (1994).
25. S. A. McHugo, J. Bailey, H. Hieslmair, and E. R. Weber, "Efficiency-limiting defects in silicon solar cell material", *J. Electron. Materials* **25**, 1417 (1994).
26. S. A. McHugo, H. Hieslmair, and E. R. Weber, "Gettering of metallic impurities in photovoltaic silicon", *Appl. Phys. A* **64**, 127 (1997).
27. M. Werner, E. R. Weber, S. McHugo, H. Hieslmair, and K. L. Chapman, "Investigation of microdefects in multicrystalline silicon for photovoltaic applications", *Solid State Phenom.* **47-8**, 449 (1996).
28. M. Werner, H. J. Möller, and E. Wolf, "Identification of microdefects in multicrystalline silicon", in *Defects and Diffusion in Silicon Processing,* T. Diaz de la Rubia, S. Coffa, P. A. Stolk, and C. S. Rafferty, Editors, p. 89, Mat. Res. Soc., Pittsburgh (1997).
29. E. R. Weber, A. A. Istratov, S. A. McHugo, H. Hieslmair, and C. Flink, "Minority carrier diffusion length degradation in silicon: who is the culprit?" in *Recombination lifetime measurements in silicon,* D. C. Gupta, F. R. Bacher, and W. M. Hughes, Editors, p. 18, ASTM, West Conshohocken (1998).
30. K. Graff, *Metal impurities in silicon-device fabrication*, Springer, Berlin (1995).
31. E. R. Weber, "Transition metals in silicon", *Appl. Phys. A* **30**, 1 (1983).
32. H. Reiss, C. S. Fuller, and F. J. Morin, "Chemical Interactions Among Defects in Germanium and Silicon", *Bell Syst. Techn. J.* **35**, 535 (1956).
33. J. D. Struthers, "Solubility and Diffusivity of Gold, Iron, and Copper in Silicon", *J. Appl. Phys.* **27**, 1560 (1956).
34. R. Keller, M. Deicher, W. Pfeiffer, H. Skudlik, D. Steiner, and T. Wichert, "Copper in silicon", *Phys. Rev. Lett.* **65**, 2023 (1990).

35. A. Mesli and T. Heiser, "Defect reactions in copper-diffused and quenched p-type silicon", *Phys. Rev. B* **45**, 11632 (1992).
36. T. Heiser and A. Mesli, "Determination of the copper diffusion coefficient in silicon from transient ion drift", *Appl. Phys. A* **57**, 325 (1993).
37. A. Mesli, T. Heiser, and E. Mulheim, "Copper diffusivity in silicon: a re-examination", *Mater. Sci. Eng. B* **25**, 141 (1994).
38. P. Wagner, H. Hage, H. Prigge, T. Prescha, and J. Weber, "Properties of copper-induced complexes in silicon", in *Semiconductor Silicon - 1990,* H. R. Huff, K. G. Barraclough, and J. I. Chikawa, Editors, p. 675, The Electrochem. Soc., Pennington (1990).
39. S. K. Estreicher, "Copper, lithium, and hydrogen passivation of boron in c-Si", *Phys. Rev. B* **41**, 5447 (1990).
40. D. V. Lang, "Deep-level transient spectroscopy: a new method to characterize traps in semiconductors", *J. Appl. Phys.* **45**, 3023 (1974).
41. G. Baccarani, M. Rudan, G. Spadini, H. Maes, W. Vandervorst, and R. van Overstraeten, "Interpretation of C-V measurements for determining the doping profile in semiconductors", *Sol. St. Electron.* **23**, 65 (1980).
42. W. Jungling, P. Pichler, S. Selberherr, E. Guerrero, and H. W. Potzl, "Simulation of critical IC fabrication processes using advanced physical and numerical methods", *IEEE Trans. Electron Dev.* **ED-32**, 156 (1985).
43. D. E. Woon, D. S. Marynick, and S. K. Estreicher, "Titanium and copper in Si: barriers for diffusion and interactions with hydrogen", *Phys. Rev. B* **45**, 13383 (1992).
44. H. Feichtinger, "Electrical and kinetic properties of thermally activated iron in silicon", *Acta Phys. Austr.* **51**, 161 (1979).
45. H. Hieslmair, A. A. Istratov, C. Flink, S. A. McHugo, and E. R. Weber, "Experiments and computer simulations of iron profiles in p/p+ silicon: segregation and the position of the iron donor level", *Physica B* **273-274**, 441 (1999).
46. T. Prescha, T. Zundel, J. Weber, H. Prigge, and P. Gerlach, "Fast-diffusing defects induced by copper in silicon", *Mater. Sci. Engin. B* **4**, 79 (1989).
47. G. Zoth and W. Bergholz, "A fast, preparation-free method to detect iron in silicon", *J. Appl. Phys.* **67**, 6764 (1990).
48. W. Schröter, M. Seibt, and D. Gilles, "Electronic Structure and Properties of Semiconductors", in *Materials Science and Technology: A Comprehensive Treatment,* R. W. Cahn, P. Haasen, and E. J. Kramer, Editors, p. 576, VCH, New York (1991).
49. M. Seibt, M. Griess, A. A. Istratov, H. Hedemann, A. Sattler, and W. Schröter, "Formation and properties of copper silicide precipitates in silicon", *phys. stat. sol. (a)* **166**, 171 (1998).
50. M. Seibt and K. Graff, "TEM study of metal impurity precipitates in the surface regions of silicon wafers", in *Defects in Electronic Materials,* M. Stavola, S. J. Pearton, and G. Davies, Editors, p. 215, Mat. Res. Soc, Pittsburgh (1988).
51. E. Nes and J. Washburn, "Transmission electron microscope investigation of the growth of copper precipitate colonies in silicon", *J. Appl. Phys.* **44**, 3682 (1973).
52. M. Seibt and K. Graff, "Characterization of haze-forming precipitates in silicon", *J. Appl. Phys.* **63**, 4444 (1988).
53. M. Seibt, "Homogeneous and heterogeneous precipitation of copper in silicon", in *Semiconductor Silicon 1990,* H. R. Huff, K. G. Barraclough, and J. I. Chikawa, Editors, p. 663, The Electrochem. Soc., Pennington (1990).

54. A. Broniatowski and C. Haut, "The electronic properties of copper-decorated twinned boundaries in silicon", *Philos. Mag. Lett.* **62**, 407 (1990).
55. E. Nes and J. Washburn, "Precipitation in high-purity silicon single crystals", *J. Appl. Phys.* **42**, 3562 (1971).
56. E. Nes and G. Lunde, "Copper precipitate colonies in silicon", *J. Appl. Phys.* **43**, 1835 (1972).
57. A. Correia, D. Ballutaud, A. Boutry-Forveille, and J. L. Maurice, "Effects of copper and oxygen precipitation during thermal oxidation of silicon: an electron-beam-induced current study", *J. Appl. Phys.* **78**, 6543 (1995).
58. E. Nes, "The mechanism of repeated precipitation on dislocations", *Acta Metallurgica* **22**, 81 (1974).
59. J. M. Silcock and W. J. Tunstall, *Phil. Mag.*, 361 (1964).
60. M. Seibt, "Metal impurity precipitation in silicon", in *Crystalline defects and contamination: their impact and control in device manufacturing II,* B. O. Kolbesen, C. Claeys, P. Stallhofer, and F. Tardif, Editors, p. 243, The Electrochem. Soc., Pennington (1997).
61. M. El Kajbaji and J. Thibault, "Platelet copper precipitates in silicon: a high-resolution electron microscopy study", *Philos. Mag. Lett.* **71**, 335 (1995).
62. W. Schröter, J. Kronewitz, U. Gnauert, F. Riedel, and M. Seibt, "Bandlike and localized states at extended defects in silicon", *Phys. Rev. B* **52**, 13726 (1995).
63. H. Hedemann and W. Schroeter, "Deep-level transient-spectroscopy for localized states at extended defects in semiconductors", *J. de Physique III* **7**, 1389 (1997).
64. A. A. Istratov, C. Flink, H. Hieslmair, T. Heiser, and E. R. Weber, "Influence of interstitial copper on diffusion length and lifetime of minority carriers in p-type silicon", *Appl. Phys. Lett.* **71**, 2121 (1997).
65. T. Heiser, S. McHugo, H. Hieslmair, and E. R. Weber, "Transient ion drift detection of low level copper contamination in silicon", *Appl. Phys. Lett.* **70**, 3576 (1997).
66. M. B. Shabani, T. Yoshimi, and H. Abe, "Low-temperature out-diffusion of Cu from silicon wafers", *J. Electrochem. Soc.* **143**, 2025 (1996).
67. C. McCarthy, M. Miyazaki, H. Horie, S. Okamoto, and H. Tsuya, "Room temperature copper out-diffusion from the bulk of silicon wafers and its behavior following various postanneal treatments", in *Semiconductor Silicon 1998,* H. Huff, U. Gösele, and H. Tsuya, Editors, p. 629, The Electrochem. Soc., Pennington (1998).
68. T. Sinno, R. A. Brown, W. Van Ammon, and E. Dornberger, "Point defect dynamics and the oxidation-induced stacking-fault ring in Czochralski-grown silicon crystals", *J. Electrochem. Soc.* **145**, 302 (1998).
69. G. Kissinger, G. Morgenstern, and H. Richter, "Copper silicide precipitation influenced by the strain of a Ge/sub 0.02/Si/sub 0.98/ heteroepitaxial layer", *J. Appl. Phys.* **75**, 4994 (1994).
70. S. A. McHugo, A. C. Thompson, C. Flink, E. R. Weber, G. Lamble, B. Gunion, A. MacDowell, R. Celestre, H. A. Padmore, and Z. Hussain, "Synchrotron-based impurity mapping", *J. Cryst. Growth* **210**, 395 (2000).
71. A. Goetzberger and W. Shockley, "Metal precipitates in silicon p-n junctions", *J. Appl. Phys.* **31**, 1821 (1960).
72. J. R. Davis, A. Rohatgi, R. H. Hopkins, P. D. Blais, P. Rai-Choudhury, J. R. McCormic, and H. C. Mollenkopf, "Impurities in silicon solar cells", *IEEE Trans. Electron. Dev.* **ED-27**, 677 (1980).
73. R. H. Hopkins and A. Rohatgi, "Impurity Effects in Silicon for High Efficiency Solar Cells", *J. Cryst. Growth* **75**, 67 (1985).

74. S. Naito and T. Nakashizu, "Electric degradation and defect formation of silicon due to Cu, Fe, and Ni contamination", in *Defect Engineering in Semiconductor Growth, Processing and Device Technology,* S. Ashok, J. Chevallier, K. Sumino, and E. Weber, Editors, p. 641, Mat. Res. Soc., Pittsburgh (1992).
75. M. Itsumi, Y. Sato, K. Imai, and N. Yabumoto, "Characterization of metallic impurities in Si using a recombination-lifetime correlation method", *J. Appl. Phys.* **82**, 3250 (1997).
76. D. Walz, J. P. Joly, M. Suarez, J. Palleau, and G. Kamarinos, "Characterization of copper and nickel contamination using recombination lifetime techniques", in *Analytical Techniques for Semiconductor Materials and Process Characterization II,* B. O. Kolbesen, C. Claeys, and P. Stallhofer, Editors, p. 64, The Electrochem. Soc., Pennington (1995).
77. H. Prigge, P. Gerlach, P. O. Hahn, A. Schnegg, and H. Jacob, "Acceptor compensation in silicon induced by chemomechanical polishing", *J. Electrochem. Soc.* **138**, 1385 (1991).
78. A. L. P. Rotondaro, T. Q. Hurd, A. Kaniava, J. Vanhellemont, E. Simoen, M. M. Heyns, C. Claeys, and G. Brown, "Impact of Fe and Cu contamination on the minority carrier lifetime of silicon substrates", *J. Electrochem. Soc.* **143**, 3014 (1996).
79. M. Miyazaki, "Influence of metal impurities on lifetime", in *Recombination lifetime measurements in silicon,* D. C. Gupta, F. R. Bacher, and W. M. Hughes, Editors, p. 294, ASTM, West Conshohocken (1998).
80. W. B. Henley and D. A. Ramappa, "Detection of copper contamination in silicon by surface photovoltage diffusion length measurements", *Appl. Phys. Lett.* **74**, 278 (1999).
81. J.-G. Lee and S. R. Morrison, "Copper passivation of dislocations in silicon", *J. Appl. Phys.* **64**, 6679 (1988).
82. B. Shen, T. Sekiguchi, J. Jablonski, and K. Sumino, "Gettering of copper by bulk stacking faults and punched-out dislocations in Czochralski-grown silicon", *J. Appl. Phys.* **76**, 4540 (1994).
83. B. Shen, T. Sekiguchi, and K. Sumino, "Precipitation of Cu, Ni and Fe on Frank-type partial dislocations in Czochralski-grown silicon", *Mater. Sci. Forum* **196-201**, 1207 (1995).
84. B. Shen, T. Sekiguchi, Z. Rong, Y. Shi, H. Shi, Y. Kai, Z. Youdou, and K. Sumino, "Precipitation of Cu and Fe in dislocated floating-zone-grown silicon", *Jpn. J. Appl. Phys.* **35**, 3301 (1996).
85. F. S. Ham, "Theory of Diffusion-Limited Precipitation", *J. Phys. Chem. Solids* **6**, 335 (1958).
86. H. Hieslmair, A. A. Istratov, S. A. McHugo, C. Flink, T. Heiser, and E. R. Weber, "Gettering of iron by oxygen precipitates", *Appl. Phys. Lett.* **72**, 1460 (1998).
87. C. Flink, H. Feick, S. A. McHugo, A. Mohammed, W. Seifert, H. Hieslmair, T. Heiser, A. Istratov, and E. R. Weber, "Formation of copper precipitates in silicon", *Physica B* **273-274**, 437 (1999).
88. C. Flink, Ph.D. thesis, Köln, Germany (2000).
89. P. Omling, E. R. Weber, L. Montelius, H. Alexander, and J. Michel, "Electrical properties of dislocations and point defects in plastically deformed silicon", *Phys. Rev. B* **32**, 6571 (1985).
90. H. B. Aaron and G. R. Kotler, "Secon phase dissolution", *Metal. Trans.* **2**, 393 (1971).
91. S. A. McHugo, "Release of metal impurities from structural defects in polycrystalline silicon", *Appl. Phys. Lett.* **71**, 1984 (1997).
92. K. J. Solberg, "The crystal structure of eta -Cu/sub 3/Si precipitates in silicon", *Acta Crystallographica A* **A34**, 684 (1978).
93. T. Kitano, "Local structure around iron at the SiO/sub 2//Si interface", *J. Electron. Mat.* **21**, 1027 (1992).

94. R. R. Kola, G. A. Rozgonyi, J. Li, W. B. Rogers, T. Y. Tan, K. E. Bean, and K. Lindberg, "Transition metal silicide precipitation in silicon induced by rapid thermal processing and free-surface gettering", *Appl. Phys. Lett.* **55**, 2108 (1989).
95. W. K. Tice and T. Y. Tan, "Nucleation of CuSi precipitate colonies in oxygen-rich silicon", *Appl. Phys. Lett.* **28**, 564 (1976).
96. S. J. Pearton, J. W. Corbett, and T. S. Shi, "Hydrogen in crystalline semiconductors", *Appl. Phys. A* **43**, 153 (1987).
97. J. Meier, S. Dubail, R. Platz, P. Torres, U. Kroll, J. A. A. Selvan, N. P. Vaucher, C. Hof, D. Fischer, H. Keppner, R. Flueckiger, A. Shah, V. Shklover, and K. D. Ufert, "Towards high-efficiency thin-film silicon solar cells with the "micromorph" concept", *Solar Energy Mat. Solar Cells* **49**, 35 (1997).
98. R. Plieninger, H. N. Wanka, J. Kuhnle, and J. H. Werner, "Efficient defect passivation by hot-wire hydrogenation", *Appl. Phys. Lett.* **71**, 2169 (1997).
99. O. V. Feklisova and N. A. Yarykin, "Transformation of deep-level spectrum of irradiated silicon due to hydrogenation under wet chemical etching", *Semicond. Sci. Technol.* **12**, 742 (1997).
100. Y. Tokuda, "Deep-level transient spectroscopy study of hydrogen-related traps formed by wet chemical etching in electron-irradiated n-type silicon", *Jpn. J. Appl. Phys.* **37**, 1815 (1998).
101. J. U. Sachse, E. O. Sveinbjornsson, W. Jest, J. Weber, and H. Lemke, "Electrical properties of platinum-hydrogen complexes in silicon", *Phys. Rev. B* **55**, 16176 (1997).
102. W. Jost and J. Weber, "Titanium-hydrogen defects in silicon", *Phys. Rev. B* **54**, R11038 (1996).
103. N. Yarykin, J. U. Sachse, J. Weber, and H. Lemke, "Electrically active silver-hydrogen complexes in silicon", *Mater. Sci. Forum* **258-263**, 301 (1997).
104. W. Jost, J. Weber, and H. Lemke, "Hydrogen-cobalt complexes in p-type silicon", *Semicond. Sci. Technol.* **11**, 525 (1996).
105. A. J. Tavendale and S. J. Pearton, "Deep level, quenched-in defects in silicon doped with gold, silver, iron, copper or nickel", *J. Phys. C* **16**, 1665 (1983).
106. S. J. Pearton and A. J. Tavendale, "Electrical properties of deep silver- and iron-related centres in silicon", *J. Phys. C* **17**, 6701 (1984).
107. J. Weber, "private communications", (1998).
108. M. Kouketsu and S. Isomae, "Hydrogen passivation of iron-related hole traps in silicon", *J. Appl. Phys.* **80**, 1485 (1996).
109. M. Kouketsu, K. Watanabe, and S. Isomae, "Hydrogen passivation of iron-related hole traps in silicon", *Mater. Sci. Forum* **196-201**, 861 (1995).
110. E. B. Yakimov and A. L. Parakhonsky, "Hydrogen stimulated destruction of Fe-B pairs in p-Si", *Solid State Phenom.* **57-58**, 383 (1997).
111. M. Kaniewska, J. Kaniewski, L. Ornoch, T. Sekiguchi, and K. Sumino, "Hydrogenation of deep defect states in n-type Si containing extended defects and transition metal (Ni or Fe)", *Mater. Sci. Forum* **258-63**, 325 (1997).
112. T. Sadoh, A. K. Tsukamoto, A. Baba, D. Bai, A. Kenjo, T. Tsurushima, H. Mori, and H. Nakashima, "Deep level of iron-hydrogen complex in silicon", *J. Appl. Phys.* **82**, 3828 (1997).
113. S. Sadamitsu, A. Sasaki, M. Hourai, S. Sumita, and N. Fujino, "Transmission electron microscopy observation of defects induced by Fe contamination on Si(100) surface", *Jpn. J. Appl. Phys.* **30**, 1591 (1991).
114. N. R. Baldwin and D. G. Ivey, "Iron silicide formation in bulk iron-silicon diffusion couples", *J. Phase Equilibria* **16**, 300 (1995).

115. T. B. Massalski, H. Okamoto, P. R. Subramanian, and L. Kacprzak, *Binary Alloy Phase Diagrams*, ASM International, Materials Park (1990).
116. P. Augustus, "Detection of Fe and Ni surface precipitates by TEM", *in* "Semicond. Int." Vol. 8, p. 88 (1985).
117. M. D. De Coteau, P. R. Wilshaw, and R. Falster, "Precipitation of iron in silicon: gettering to extended surface defect sites", *Solid State Phenom.* **19-20**, 27 (1991).
118. P. J. Ward, "A survey of iron contamination in silicon substrates and its impact on circuit yield", *J. Electrochem. Soc.* **129**, 2573 (1982).
119. K. Radermacher, R. Carius, and S. Mantl, "Optical and electrical properties of buried semiconducting beta -FeSi/sub 2", *Nuclear Instrum. Methods Phys. Res. B* **84**, 163 (1994).
120. H. Katsumata, Y. Makita, N. Kobayashi, H. Shibata, M. Hasegawa, I. Aksenov, S. Kimura, A. Obara, and S. Uekusa, "Optical absorption and photoluminescence studies of beta -FeSi/sub 2/ prepared by heavy implantation of Fe/sup +/ ions into Si", *J. Appl. Phys.* **80**, 5955 (1996).
121. X. W. Lin, J. Desimoni, H. Bernas, Z. Liliental-Weber, and J. Washburn, "Evolution of cubic FeSi/sub 2/ in Si upon thermal annealing", in *Phase Transformations in Thin Films - Thermodynamics and Kinetics,* M. Atzmon, A. L. Greer, J. M. E. Harper, and M. R. Libera, Editors, p. 293, Mat. Res. Soc., Pittsburgh (1993).
122. X. W. Lin, M. Behar, J. Desimoni, H. Bernas, W. Swider, Z. Liliental-Weber, and J. Washburn, "Epitaxial phase formation of FeSi/sub 2/ in an Fe-implanted Si by ion irradiation and rapid thermal annealing", in *Beam Solid Interactions: Fundamentals and Applications,* M. Nastasi, L. R. Harriott, N. Herbots, and R. S. Averback, Editors, p. 535, Mat. Res. Soc., Pittsburgh (1993).
123. R. L. Maltez, M. Behar, L. Amaral, P. F. P. Fichtner, and X. W. Lin, "Depth, phase and coarsening evolution of FeSi/sub 2/ precipitates upon thermal annealing", *Nucl. Instrum. Methods Phys. Res. B* **96**, 366 (1995).
124. C. W. T. Bulle-Lieuwma, D. J. Oostra, and D. E. W. Vandenhoudt, "TEM investigation of Si/ beta FeSi/sub 2//Si (100) and (111) heterostructures formed by Fe implantation", in *Microcrystalline Semiconductors: Materials Science and Devices,* P. M. Fauchet, C. C. Tsai, L. T. Canham, I. Shimizu, and Y. Aoyagi, Editors, p. 885, Mat. Res. Soc., Pittsburgh (1993).
125. J. Desimoni, H. Bernas, M. Behar, X. W. Lin, J. Washburn, and Z. Liliental-Weber, "Ion beam synthesis of cubic FeSi/sub 2", *Appl. Phys. Lett.* **62**, 306 (1993).
126. R. L. Maltez, L. Amaral, M. Behar, A. Vantomme, G. Langouche, and X. W. Lin, "Mossbauer study of the magnetic character and ordering process of the cubic gamma -FeSi/sub 2/ phase obtained by Fe implantation into a Si(100) matrix", *Phys. Rev. B* **54**, 11659 (1996).
127. A. Ohsawa, K. Honda, and N. Toyokura, "Metal impurities near the SiO_2-Si interface", *J. Electrochem. Soc.* **131**, 2964 (1984).
128. J. Wong-Leung, D. J. Eaglesham, J. Sapjeta, D. C. Jacobson, J. M. Poate, and J. S. Williams, "The precipitation of Fe at the Si-SiO/sub 2/ interface", *J. Appl. Phys.* **83**, 580 (1998).
129. J. Desimoni, F. H. Sánchez, M. B. Fernandez van Raap, H. Bernas, C. Clerc, and X. W. Lin, "Mossbauer characterization of gamma -FeSi/sub 2/ precipitates in Si(100)", *Phys. Rev. B* **51**, 86 (1995).
130. D. N. Leong, M. A. Harry, K. J. Reeson, and K. P. Homewood, "On the origin of the 1.5 mu m luminescence in ion beam synthesized beta -FeSi/sub 2", *Appl. Phys. Lett.* **68**, 1649 (1996).
131. K. Lefki and P. Muret, "Photoelectric study of beta -FeSi/sub 2/ on silicon: optical threshold as a function of temperature", *J. Appl. Phys.* **74**, 1138 (1993).

132. D. Leong, M. Harry, K. J. Reeson, and K. P. Homewood, "A silicon/iron-disilicide light-emitting diode operating at a wavelength of 1.5 mu m", *Nature* **387**, 686 (1997).
133. M. Kittler, W. Seifert, M. Stemmer, and J. Palm, "Interaction of iron with a grain boundary in boron-doped multicrystalline silicon", *J. Appl. Phys.* **77**, 3725 (1995).
134. A. Ihlal and R. Rizk, "Effects of iron contamination on the electrical activity of a silicon bicrystal", *J. Phys. D* **29**, 3096 (1996).
135. W. Seifert, M. Kittler, J. Vanhellemont, E. Simoen, C. Claeys, and F. G. Kirscht, "Recombination activity of oxygen precipitation related defects in Si", in *Defect Recognition and Image Processing in Semiconductors 1995,* A. R. Mickelson, Editor, p. 319, Institute of Physics, Bristol (1996).
136. M. Kittler and W. Seifert, "A reflection upon the applicability of electron beam induced current (EBIC) as a sensitive microanalytical technique (ppb range) for silicon materials research", *Scanning Microsc.* **9**, 677 (1995).
137. W. Seifert, M. Kittler, and J. Vanhellemont, "EBIC study of recombination activity of oxygen precipitation related defects in Si", *Mater. Sci. Eng. B* **42**, 260 (1996).
138. D. M. Lee and G. A. Rozgonyi, "Low-temperature gettering of trace iron and copper by misfit dislocations in Si/Si(Ge) epitaxy", *Appl. Phys. Lett.* **65**, 350 (1994).
139. C. Hässler, G. Pensl, M. Schulz, A. Voigt, and H. P. Strunk, "Grain boundaries in multicrystalline silicon. Characterization by admittance and EBIC measurements", *phys. stat. sol. (a)* **137**, 463 (1993).
140. X. Portier, A. Ihlal, and R. Rizk, "Iron silicide formation by precipitation in a silicon bicrystal", *phys. stat. sol. (a)* **161**, 75 (1997).
141. W. Rieger, "The Impact of Impurities in Chemicals on the Performance of DRAMs", in *Crystalline Defects and Contamination: Their Impact and Control in Device Manufacturing,* B. O. Kolbesen, C. Claeys, P. Stallhofer, and F. Tardif, Editors, p. 103, The Electrochem. Soc., Grenoble (1993).
142. P. S. D. Lin, R. B. Marcus, and T. T. Sheng, "Leakage and breakdown in thin oxide capacitors correlation with decorated stacking faults", *J. Electrochem. Soc.* **130**, 1878 (1983).
143. P. M. Petroff, G. A. Rozgonyi, and T. T. Sheng, "Elimination of process-induced stacking faults by preoxidation gettering of Si wafers. II. Si/sub 3/N/sub 4/ process", *J. Electrochem. Soc.* **123**, 565 (1976).
144. K. V. Ravi, C. J. Varker, and C. E. Volk, "Electrically active stacking faults in silicon", *J. Electrochem. Soc.* **120**, 533 (1973).
145. M. Miyazaki, S. Miyazaki, T. Kitamura, T. Aoki, Y. Nakashima, M. Hourai, and T. Shigematsu, "Influence of Fe contamination in Czochralski-grown silicon single crystals on LSI-yield related crystal quality characteristics", *Jpn. J. Appl. Phys.* **34**, 409 (1995).
146. M. Kageyama, N. Tsuchiya, and Y. Matsushita, "Mixed contamination effect of trace elements on the OSF/BMD generation", in *Contamination control and defect reduction in semiconductor manufacturing II,* R. Novak, D. N. Schmidt, T. Ito, and D. Reedy, Editors, p. 202, The Electrochem. Soc., Pennington (1994).
147. N. Fujino, K. Hiramoto, M. Sano, K. Murakami, H. Horiye, Y. Oka, and S. Sumita, "Quantitative diagnostic technique deduced from behavior of heavy metal contamination on silicon wafers", in *Semiconductor Silicon 1990,* H. R. Huff, K. G. Barraclough, and J. I. Chikawa, Editors, p. 709, The Electrochem. Soc., Pennington (1990).

148. K. Schmalz, F. G. Kirscht, S. Niese, H. Richter, M. Kittler, W. Seifert, I. Babanskaya, H. Klose, K. Tittelbach-Helmrich, and J. Schoneich, "On the intrinsic gettering in Fe-contaminated Cz-Si", *phys. stat. sol. (a)* **100**, 69 (1987).
149. M. Hourai, K. Murakami, T. Shigematsu, N. Fujino, and T. Shiraiwa, "Behavior of defects induced by metallic impurities on Si(100) surfaces", *Jpn. J. Appl. Phys.* **28**, 2413 (1989).
150. D. Gilles, E. R. Weber, S. Hahn, O. R. Monteiro, and K. Cho, "Model of internal gettering from low-temperature Fe precipitation kinetics in Czochralski silicon", in *Semiconductor Silicon 1990,* H. R. Huff, K. G. Barraclough, and J. I. Chikawa, Editors, p. 697, The Electrochem. Soc., Pennington (1990).
151. D. Gilles, E. R. Weber, and S. K. Hahn, "Mechanism of internal gettering of interstitial impurities in Czochralski-grown silicon", *Phys. Rev. Lett.* **64**, 196 (1990).
152. M. Aoki, A. Hara, and A. Ohsawa, "Intrinsic gettering of iron impurities in silicon wafers", *Jpn. J. Appl. Phys.* **30**, 3580 (1991).
153. M. Aoki, A. Hara, and A. Ohsawa, "Fundamental properties of intrinsic gettering of iron in a silicon wafer", *J. Appl. Phys.* **72**, 895 (1992).
154. M. Aoki and A. Hara, "Distribution of Fe in an intrinsic gettered silicon wafer after annealing at supersaturation temperature", *Jpn. J. Appl. Phys. (Letters)* **35**, L1231 (1996).
155. H. Hieslmair, A. A. Istratov, T. Heiser, and E. R. Weber, "Evaluation of precipitate densities and capture radii from the analysis of precipitation kinetics", *J. Appl. Phys.* **84**, 713 (1998).
156. S. Sadamitsu, S. Ogushi, Y. Koike, N. Reilly, T. Nagashima, M. Sano, and H. Tsuya, "Gettering in advanced low temperature processes", *Solid State Phenom.* **57-58**, 53 (1997).
157. S. Ogushi, S. Sadamitsu, K. Marsden, Y. Koike, and M. Sano, "Gettering characteristics of heavy metal impurities in silicon wafers with polysilicon back seal and internal gettering", *Jpn. J. Appl. Phys.* **36**, 6601 (1997).
158. O. Kononchuk, K. G. Korablev, N. Yarykin, and G. A. Rozgonyi, "Diffusion of iron in the silicon dioxide layer of silicon-on-insulator structures", *Appl. Phys. Lett.* **73**, 1206 (1998).
159. M. B. Shabani, T. Yoshimi, S. Okuuchi, and H. Abe, "A quantitative method of metal impurities depth profiling for gettering evaluation in silicon wafers", *Solid State Phenom.* **57-58**, 81 (1997).
160. K. Honda, T. Nakanishi, A. W. Ohsawa, and N. Toyokura, "Catastrophic breakdown in silicon oxides: the effect of Fe impurities at the SiO/sub 2/-Si interface", *J. Appl. Phys.* **62**, 1960 (1987).
161. Y. Kamiura, F. Hashimoto, and M. Iwami, "Observation of iron pileup and reduction of SiO/sub 2/ at the Si-SiO/sub 2/ interface", *Appl. Phys. Lett.* **53**, 1711 (1988).
162. Y. Kamiura, F. Hashimoto, and M. Iwami, "Iron accumulation at the Si-SiO/sub 2/ interface and possible reduction of SiO/sub 2", *Appl. Surf. Sci.* **41-42**, 447 (1989).
163. T. Yoshimi, M. B. Shabani, S. Okuuchi, and H. Abe, "Diffusion and out-diffusion behavior of Fe in Si wafer for different annealing", in *Diagnostic Techniques for Semiconductor Materials and Devices,* P. Rai-Choudhury, J. L. Benton, D. K. Schroder, and T. J. Shaffner, Editors, p. 452, Mat. Res. Soc., Pennington (1997).
164. X. Ding, M. F. Chiah, W. Y. Cheung, S. P. Wong, J. B. Xu, I. H. Wilson, W. Hui-min, C. Li-zhi, and L. Xiang-huai, "Aggregation and out diffusion of iron atoms for Fe ion implanted silica films", *J. Appl. Phys.* **86**, 2550 (1999).
165. D. A. Ramappa and W. B. Henley, "Stability of iron-silicide precipitates in silicon", *J. Electrochem. Soc.* **144**, 4353 (1997).

166. E. G. Colas and E. R. Weber, "Reduction of iron solubility in silicon with oxygen precipitates", *Appl. Phys. Lett.* **48**, 1371 (1986).
167. M. Aoki, A. Hara, and A. Ohsawa, "Intrinsic gettering of iron in Czochralski silicon crystals", in *Defect Engineering in Semiconductor Growth, Processing and Device Technology,* S. Ashok, J. Chevallier, K. Sumino, and E. Weber, Editors, p. 963, Mat. Res. Soc., Pittsburgh (1992).
168. M. Aoki and A. Hara, "Re-emission of iron originally gettered by oxygen precipitates in a silicon wafer", *J. Appl. Phys.* **74**, 1440 (1993).
169. S. A. McHugo, E. R. Weber, M. Mizuno, and F. G. Kirscht, "A study of gettering efficiency and stability in Czochralski silicon", *Appl. Phys. Lett.* **66**, 2840 (1995).
170. J. A. James and D. H. Richards, "Radiochemical analysis of silicon", *J. Electron. Control* **3**, 500 (1957).
171. F. A. Trumbore, "Solid Solubilities of Impurity Elements in Germanium and Silicon", *Bell Syst. Techn. J.* **39**, 205 (1960).
172. A. A. Bugay, V. E. Kosenko, and E. G. Miseliuk, *Zh. Techn. Phys.* **27**, 210 (1957).
173. K. Mishra, M. Banan, J. Moody, and S. Chandrasekhar, "Effect of iron and iron complexes on the minority carrier lifetime in B, Al and P doped silicon", in *Diagnostic Techniques for Semiconductor Materials and Devices,* D. K. Schroder, J. L. Benton, and P. Rai-Choudhury, Editors, p. 131, The Electrochem. Soc., Pennington (1994).
174. C. B. Collins and R. O. Carlson, "Properties of silicon doped with iron or copper", *Phys. Rev.* **108**, 1409 (1957).
175. E. R. Weber, "Solubility of Fe in Si", in *Properties of Silicon (EMIS Datareviews Series No.4)*, p. 442, INSPEC, London (1988).
176. W. Wijaranakula, "Iron precipitation at oxygen related bulk defects in Czochralski silicon", *J. Appl. Phys.* **79**, 4450 (1996).
177. B. Shen, J. Jablonski, T. Sekiguchi, and K. Sumino, "Influences of Cu and Fe impurities on oxygen precipitation in Czochralski-grown silicon", *Jpn. J. Appl. Phys.* **35**, 4187 (1996).
178. B. Hackl, K. J. Range, P. Stallhofer, and L. Fabry, "Correlation between DLTS and TRXFA measurements of copper and iron contaminations in FZ and CZ silicon wafers; application to gettering efficiencies", *J. Electrochem. Soc.* **139**, 1495 (1992).
179. K. Graff and H. Pieper, "The properties of iron in silicon", *J. Electrochem. Soc.* **128**, 669 (1981).
180. E. Weber and H. G. Riotte, "The solution of iron in silicon", *J. Appl. Phys.* **51**, 1484 (1980).
181. E. Weber, "Iron as a thermal defect in silicon", *Appl. Phys. Lett.* **33**, 433 (1978).
182. S. E. Beck, M. A. George, D. A. Bohling, B. J. Shemanski, R. G. Ridgeway, G. A. Hames, J. J. Wortman, and W. A. Lanford, "Gas phase contaminants and their effects on MOS structures", *in* "Solid State Technol." Vol. 38, p. 69 (1995).
183. A. L. P. Rotondaro, T. Q. Hurd, A. Kaniava, J. Vanhellemont, E. Simoen, M. M. Heyns, C. Claeys, and G. Brown, "The impact of Fe and Cu on the minority carrier lifetime of p and n-type silicon wafers", in *Analytical Techniques for Semiconductor Materials and Process Characterization II,* B. O. Kolbesen, C. Claeys, and P. Stallhofer, Editors, p. 54, The Electrochem. Soc., Pennington (1995).
184. H. C. Swart and G. L. P. Berning, "The effect of oxygen on the formation of iron silicide", *Appl. Surf. Sci.* **78**, 77 (1994).
185. R. Takizawa, T. Nakanishi, and A. Ohsawa, "Degradation of metal-oxide-semiconductor devices caused by iron impurities on the silicon wafer surface", *J. Appl. Phys.* **62**, 4933 (1987).

186. H. Shimizu, "Behavior of metal-induced oxide charge during thermal oxidation in silicon wafers", *J. Electrochem. Soc.* **144**, 4335 (1997).
187. H. Shimizu, H. Uchida, and S. Ishiwari, "Confirmation of aluminum distribution in thermally grown oxide of silicon wafers", *Jpn. J. Appl. Phys.* **33**, 5690 (1994).
188. H. Shimizu and S. Saitou, "Iron-induced negative charge in thermally grown oxide of silicon wafers", *Jpn. J. Appl. Phys.* **34**, 3071 (1995).
189. H. Shimizu and S. Ishiwari, "Iron distribution and iron-induced negative charge in thin SiO2 films on silicon wafers", *Mater. Trans. JIM (Japan)* **36**, 1271 (1995).
190. T. Abe, T. Itoh, Y. Hayamizu, K. Sunagawa, S. Yokota, and H. Yamagishi, "The Contrastive Behavior of Fe and Cu Impurities in Si Crystals", in *Defect Control in Semiconductors,* K. Sumino, Editor, p. 297, Elsevier Science Publishers B. V. (1990).
191. S. Saito, K. Hamada, D. J. Eaglesham, Y. Shiramizu, J. L. Benton, H. Kitajima, S. D. C. Jacobson, and J. M. Poate, "Impact of metal contamination of 7.0 nm gate oxides on various substrate materials", in *Materials Reliability in Microelectronics VII,* J. J. Clement, R. R. Keller, K. S. Krisch, J. E. Sanchez, Jr., and Z. Suo, Editors, p. 141, Mat. Res. Soc., Pittsburgh (1997).
192. P. W. Mertens, A. L. P. Rotondaro, M. Meuris, H. F. Schmidt, M. M. Heyns, and D. Gräf, "Effect of oxidation ramp up on the redistribution of metallic contamination in gate oxides", in *1994 proceedings of the institute of enviromental sciences, vol.1 (ISBN 1-877862-45-2)*, p. 325, IES, Mount Prospect, IL, USA (1994).
193. F. Tardif, J. P. Joly, T. Lardin, A. Tonti, P. Patruno, D. Levy, and W. Sievert, "Impact Study of the use of ULSI, VLSI, and MOS grade chemicals in the RCA cleaning process on MOS and bipolar devices", in *Crystalline Defects and Contamination: Their Impact and Control in Device Manufacturing,* B. O. Kolbesen, C. Claeys, P. Stallhofer, and F. Tardif, Editors, p. 114, The Electrochem. Soc., Grenoble, France (1993).
194. F. Tardif, J. P. Joly, and T. Lardin, "Impact study of the use of ULSI, VLSI and MOS grade chemicals in the RCA cleaning process on MOS and bipolar devices", in *Cleaning technology in semiconductor device manufacturing,* J. Ruzyllo and R. E. Novak, Editors, p. 85, The Electrochem. Soc., Pennington (1994).
195. R. S. Hockett and D. Hymes, "TXRF characterization of trace metal contamination in thin gate oxides", in *Chemical Surface Preparation, Passivation and Cleaning for Semiconductor Growth and Processing,* R. J. Nemanich, C. R. Helms, M. Hirose, and G. W. Rubloff, Editors, p. 173, Mat. Res. Soc., Pittsburgh (1992).
196. L. Zhong and F. Shimura, "Dependence of lifetime on surface concentration of copper and iron in silicon wafers", *Appl. Phys. Lett.* **61**, 1078 (1992).
197. M. Takiyama, S. Ohtsuka, S. Hayashi, and M. Tachimori, "Dielectric degradation of silicon dioxide films caused by metal contaminations", in *Semiconductor Silicon - 1994,* H. R. Huff, W. Bergholz, and K. Sumino, Editors, p. 346, The Electrochem. Soc., Pennington (1994).
198. F. M. Livingston, S. Messoloras, R. C. Newman, B. C. Pike, R. J. Stewart, M. J. Binns, W. P. Brown, and J. G. Wilkes, "An infrared and neutron scattering analysis of the precipitation of oxygen in dislocation-free silicon", *J. Phys. C* **17**, 6253 (1984).
199. R. C. Newman, M. J. Binns, W. P. Brown, F. M. Livingston, S. Messoloras, R. J. Stewart, and J. G. Wilkes, "Precipitation of oxygen in silicon: kinetics, solubility, diffusivity and particle size", *Physica B&C* **116**, 264 (1983).
200. H. Fujimori, "Dependence on morphology of oxygen precipitates upon oxygen supersaturation in Czochralski silicon crystals", *J. Electrochem. Soc.* **144**, 3180 (1997).

201. A. Kaminski, J. Jouglar, M. Mergui, Y. Jourlin, A. Bouille, P. L. Vuillermoz, and A. Laugier, "Infrared characterization of hot spots in solar cells with high precision due to signal treatment processing", *Solar Energy Mat. Solar Cells* **51**, 233 (1998).
202. A. Voight, C. Hassler, D. Karg, H. P. Strunk, G. Pensl, and M. Schulz, "Shunts in n/sup +/p-junction solar cells fabricated on multicrystalline cast silicon", *Solid State Phenom.* **51-52**, 497 (1996).
203. D. Karg, C. Hassler, G. Pensl, and M. Schulz, "Characterization of local shunts in multicrystalline silicon solar cells by p-n mesa structures", *Solid State Phenom.* **51-52**, 503 (1996).
204. O. Breitenstein, K. Iwig, and I. Konovalov, "Evaluation of local electrical parameters of solar cells by dynamic (lock-in) thermography", *phys. stat. sol. (a)* **160**, 271 (1997).
205. M. Seibt, H. Hedemann, A. A. Istratov, F. Riedel, A. Sattler, and W. Schroter, "Structural and electrical properties of metal silicide precipitates in silicon", *phys. stat. sol. (a)* **171**, 301 (1999).
206. D. R. Lide, "CRC handbook of chemistry and physics", CRC press, Boca Raton (1998).
207. M. E. Schlesinger, *Chem. Rev.*, 607 (1990).
208. J. A. Van Vechten, "A simple man's view of the thermochemistry of semiconductors", in *Handbook on Semiconductors,* T. S. Moss and S. P. Keller, Editors, p. 2, North-Holland, Amsterdam (1980).
209. C. J. Gallagher, "Electrolysis of copper in solid silicon", *J. Phys. Chem. Solids* **3**, 82 (1957).
210. A. Zunger, "Electronic Structure of 3d Transition-Atom Impurities in Semiconductors", in *Solid St. Phys.,* H. Ehrenreich and D. Turnbull, Editors, p. 275, Academic Press, Orlando (1986).
211. S. K. Estreicher, "Rich chemistry of copper in crystalline silicon", *Phys. Rev. B* **60**, 5375 (1999).
212. R. Hoelzl, D. Huber, K. J. Range, L. Fabry, J. Hage, and R. Wahlich, "Gettering of copper and nickel in p/p+ epitaxial wafers", *J. Electrochem. Soc.* **147**, 2704 (2000).
213. M. Seibt and W. Schröter, "Precipitation behaviour of nickel in silicon", *Phil. Mag. A* **59**, 337 (1989).
214. F. Riedel and W. Schroter, "Electrical and structural properties of nanoscale $NiSi_2$ precipitates in silicon", *Phys. Rev. B* **62**, 7150 (2000).
215. F. Riedel, J. Kronewitz, U. Gnauert, M. Seibt, and W. Schroter, "Structural and electrical properties of $NiSi_2$ particles in silicon", *Solid State Phenom.* **47-48**, 359 (1996).

REPORT DOCUMENTATION PAGE			Form Approved OMB NO. 0704-0188
Public reporting burden for this collection of information is estimated to average 1 hour per response, including the time for reviewing instructions, searching existing data sources, gathering and maintaining the data needed, and completing and reviewing the collection of information. Send comments regarding this burden estimate or any other aspect of this collection of information, including suggestions for reducing this burden, to Washington Headquarters Services, Directorate for Information Operations and Reports, 1215 Jefferson Davis Highway, Suite 1204, Arlington, VA 22202-4302, and to the Office of Management and Budget, Paperwork Reduction Project (0704-0188), Washington, DC 20503.			
1. AGENCY USE ONLY (Leave blank)	2. REPORT DATE February 2002	3. REPORT TYPE AND DATES COVERED Final Technical Report 30 January 1998 – 29 August 2001	
4. TITLE AND SUBTITLE Impurity Precipitation, Dissolution, Gettering, and Passivation in PV Silicon Final Technical Report, 30 January 1998 – 29 August 2001 6. AUTHOR(S) Eicke R. Weber			5. FUNDING NUMBERS CF: XAF-8-17607-04 PVP22501
7. PERFORMING ORGANIZATION NAME(S) AND ADDRESS(ES) University of California at Berkeley Berkeley, California			8. PERFORMING ORGANIZATION REPORT NUMBER
9. SPONSORING/MONITORING AGENCY NAME(S) AND ADDRESS(ES) National Renewable Energy Laboratory 1617 Cole Blvd. Golden, CO 80401-3393			10.SPONSORING/MONITORING AGENCY REPORT NUMBER NREL/SR-520-31528
11.SUPPLEMENTARY NOTES NREL Technical Monitor: Robert McConnell			
12a. DISTRIBUTION/AVAILABILITY STATEMENT National Technical Information Service U.S. Department of Commerce 5285 Port Royal Road Springfield, VA 22161			12b. DISTRIBUTION CODE
13.ABSTRACT *(Maximum 200 words)* This report describes the major progress in understanding the physics of transition metals in silicon and their possible impact on the efficiency of solar cells that was achieved during the three-year span of this subcontract. We found that metal-silicide precipitates and dissolved 3d transition metals can be relatively easily gettered. Gettering and passivating treatments must take into account the individuality of each transition metal. Our studies demonstrated how significant is the difference between defect reactions of copper and iron. Copper does not significantly affect the minority-carrier diffusion length in p-type silicon, at least as long as its concentration is low, but readily precipitates in n-type silicon. Therefore, copper precipitates may form in the area of p-n junctions and cause shunts in solar cells. Fortunately, copper precipitates are present mostly in the chemical state of copper-silicide and can relatively easily be dissolved. In contrast, iron was found to form clusters of iron-oxides and iron-silicates in the wafers. These clusters are thermodynamically stable even in high temperatures and are extremely difficult to remove. The formation of iron-silicates was observed at temperatures over 900°C.			
14.SUBJECT TERMS: PV ; metal silicide precipitates ; gettering ; passivation ; minority carrier diffusion ; p-type ; p-n junctions ; X-ray fluorescence microprobe analyses ; 3d transition ; transient ion drift ; recombination activity ; beam induced current ; multicrystalline silicon			15.NUMBER OF PAGES 16.PRICE CODE
17.SECURITY CLASSIFICATION OF REPORT Unclassified	18.SECURITY CLASSIFICATION OF THIS PAGE Unclassified	19.SECURITY CLASSIFICATION OF ABSTRACT Unclassified	20.LIMITATION OF ABSTRACT UL